THE UNIVERSITY *of* LIVERPOOL

Development of Mathematical Morphology Systems for Signal Feature Extraction and Detection

Thesis submitted in accordance with the
requirements of the University of Liverpool
for the degree of Doctor of Philosophy

in

Electrical Engineering and Electronics

by

Pu Sun, BSc

July 2002

Development of Mathematical Morphology Systems for Signal Feature Extraction and Detection

by

Pu Sun

Dedicated to Fang Wang.

Acknowledgements

I would like to thank my supervisor, Professor Q. H. Wu. His dedicated and thorough supervision and unwavering attention to precision, style and clarity have greatly improved my research and the quality of this thesis. I shall always cherish his patient guidance in matters - academic, professional and personal - in which I happened to seek his advice. I would also like to thank Professor A. M. Weindling. At different stages of my work at the Liverpool Women's Hospital, my knowledge and thoughts have been enriched from the numerous (often long) discussions with him.

I am indebted to Dr. Jihong Wang, for her helpful suggestions on my research, Dr. Simon Clarke, Dr. Suresh Victor, Dr. Khalid Ibrahim and Miss Anna Feinkelstein, for discussions and assistance in the tedious task of collecting and interpreting ECG data. David Courdon and the EBME team at the Liverpool Women's Hospital provided assistance in calibrating and testing equipment, which was essential for this research. Staff at the Neonatal Intensive Care Unit of Liverpool Women's Hospital were also helpful and friendly. Also I am indebted to all those cute babies in the ward who were the basic mainstay of this work. Specially I would like to thank David Buse for improving the language of much that I have written.

I have made good friends at the University of Liverpool with whom I share precious memories of my graduate student life. My gratitude and appreciation can never measure up to all the help and support that I received from Lin Jiang, Nicholas Huxley, David Buse, Wenhu Tang, Dongjiang Zhang, and other colleagues in the Department of Electrical Engineering and Electronics.

This research was made possible by a studentship from the Newborn Appeal at the Liverpool Women's Hospital and additional support from an Overseas Research Students award (ORS) offered by Universities UK (formerly known as CVCP).

Last, but not least, I thank my wife, parents and sister, for all their help and encouragement in every step of my work and in preparing this thesis, for putting up with my ever changing moods throughout these years and most of all for believing in me all the time.

Abstract

This thesis describes a set of algorithms and systems that were developed, using signal processing techniques based on *mathematical morphology* (MM), for neonatal electrocardiogram (ECG) signal analysis and power transformer inrush current identification.

MM methodologies are founded on set-theoretic concepts and nonlinear superpositions of signals and images. Morphological operations have been applied successfully to a wide range of problems including image processing and analysis tasks, noise suppression, feature extraction and pattern recognition etc. This approach seems very appropriate for dealing with objects which share common features, and has thus attracted attention for solving problems similar to those described in this thesis, which are closely related to feature extraction and identification.

This thesis begins with a systematic introduction to MM. It explains the historical background and the concept of MM, highlights the advantages of MM as an advanced nonlinear signal/image processing technique. A brief comparison between MM and traditional filtering techniques is then given, followed by the descriptions of various morphological operations, from basic operators defined for binary images, to the elaborate generalised framework for sets in a generic mathematical space, the complete lattice.

The development of a morphological method to discriminate magnetising inrush current waveform from internal fault conditions of large power trans-

formers is then described. A morphological signal decomposition scheme is proposed to allow the unique feature associated with the inrush current waveform to be separated and identified in the time domain, to avoid the problems of sensitivity and robustness that may occur in the traditional Fourier analysis based approaches. The performance of the proposed method is assessed and discussed, based on signals derived from various operating conditions of the transformer.

The second application presented is a morphological scheme for neonatal ECG signal processing and analysis, aiming to facilitate the investigation of the relationship between the clinical pattern of asphyxiated newborn infants and alterations of the ECG pattern. Neonatal ECGs are not routinely used to achieve a detailed analysis as these measurements would usually involve the time consuming act of manual interpretation and measurement. Existing technologies have also not yet been able to accurately monitor these parameters due to the rapid heart rate and the variation of waveform morphology of babies. In the proposed scheme, a morphological filtering method that incorporates subject specific information is developed, to remove the interferences introduced by recording environments and subjects without much distortion to the ECG pattern of interest. The performance of the proposed algorithms is examined using simulated neonatal ECGs and experimental signals acquired from infants. The possibility of extending this study to the fetuses is also considered, in which the fetal ECG would be obtained from the composite maternal signal, to allow intervention at an early stage for fetuses at a high risk of asphyxia.

The implementation and integration of the morphological system for neonatal ECG analysis is then described. A prototype of the morphological ECG analyser is developed, which allows the system to be used in clinics by persons without a detailed knowledge of the technology. The optimisation of basic morphological operators, code design, hardware integration and optimisation

are discussed, with emphasis on a generic architecture that can accommodate future improvement and extension without major revision of the code. The results obtained from the pilot trial on the ward of Liverpool Women's Hospital are then given and investigated, focusing on the accuracy of the ECG measurements and the relationship between the waveform morphology and the gestational ages of the babies.

The major contributions of this work are the utilisation of the advanced performance of MM for feature enhancement, extraction, noise suppression and background normalisation. The studies include the development of morphological algorithms for the decomposition and representation of the power transformer inrush current waveform, and further to enhance its features of interest and to allow them to be identified; introduction of a novel approach for neonatal ECG signal processing and analysis; development of an integrated morphological system for medical research on the neonatal ECG, and investigation of the results obtained from this system with experiments carried out in a clinical environment.

Contents

List of Figures

List of Tables

List of symbols and abbreviations

Mathematical Morphology

MM	mathematical morphology
GS	grey-scale
GSMF	grey-scale morphological filter
n–D	n dimensional, $n = 1, 2, \ldots$
$\mathbb{E}^d$	d dimensional Euclidean space
SE	structuring element
GSE	grey-scale structuring element
$\varnothing$	empty set
$A \oplus B$	dilation of A by B
$A \ominus B$	erosion of A by B
$A \circ B$	opening of A by B
$A \bullet B$	closing of A by B
$\delta_A(X)$	dilation of A by SE A
$\varepsilon_A(X)$	erosion of A by SE A
$\forall$	for all
$\breve{f}$	transpose of f
f^c	complement of f
■	foreground in binary image
□	background in binary image
$\cup$	union
$\cap$	intersection

Transformer inrush current detection

CT	current transformer
EMTDC/PSCAD	power system simulation softwares
LabVIEW	a programming language for control and automation
Matlab	a programming language for scientific research

Electrocardiogram processing

ECG	electrocardiogram
FECG	fetal ECG
MECG	maternal ECG
I, II, III	bipolar limb ECG leads
LA, RA, LL, RL	left arm, right arm, left leg, right leg
aVR, aVL, aVF	unipolar limb ECG leads
P, Q, R, S, T, U	ECG waves
QRS	QRS complex
ST	ST segment
PR, QT, QRS, RR (intervals)	ECG intervals between various waves
QTc	corrected QT interval
SA	sinoatrial node
AV	atrioventricular node
VLBW	very low birth weight
SIDS	sudden infant death syndrome
CRIB	clinical risk index for babies
FIR	finite impulse response
IIR	infinite impulse response
SNR	signal to noise ratio
CV	coefficient of variation
SD	standard deviation
SVD	singular value decomposition

Chapter 1

Introduction

This chapter introduces the motivations behind this study on the applications of mathematical morphology (MM), explains the historical background and concept of MM, highlights the advantages of MM as an advanced nonlinear signal/image processing technique, and summarise the contributions from this research. The layout of the thesis is also given at the end of the chapter.

1.1 Motivations and historical background of MM

1.1.1 Motivations

Different techniques are applied in signal and image processing depending on the type of information carried by the signal. A widespread attitude, adopted by researchers, is empiricism: try something (or even anything), and see what happens [2]. However, the important point is that the analysis technique must be matched by the way in which information is being carried in the signal [3].

MM emerges as a general theory that provides a unified approach to deal

with problems in medicine, geology, geography, remote sensing, and many other fields [4] [5] [6]. In spite of the diversity of purpose, all of these problems have a common feature: the need to extract shape information from signals. From a review of the literature, the shape information extracted with the use of MM tools proves to be suitable for the characterisation of those features [7], while promising to be effective for various automatic classification schemes. Inspired by the appropriateness of MM in dealing with objects that share common features, this study attempts to apply MM to problems that closely relate to feature extraction, detection and discrimination.

The first such attempt described in this thesis is in the area of power system relaying, where differential protection has been applied so far as the primary protection for large power transformers [8]. This method detects every type of internal fault while blocking trip signals caused by inrush. By incorporating a harmonic constraint of the input signal over time [9], the second harmonic is used as the characteristic component of the asymmetrical magnetisation peculiar to the inrush. However, security problems may arise with advances in the capacity and manufacturing technology of power transformers, which minimise the level of the second harmonic of the inrush current [10]. Contrary to this, in high voltage power systems with series capacitor compensation, the second harmonic content of fault current may be well above the threshold for inrush detection [11]. Therefore, the lack of sensitivity and robustness becomes major challenges to this traditional technique and further improvement on inrush signal identification is still in high demand.

Research on improving the performance of the harmonics constraint based inrush current identification algorithms continues [12] [13] [14]. However, most of these studies are either based on the transformer equivalent circuit model or require some transformer data, and this may become susceptible to parameter variations. Compared to traditional Fourier transform based harmonic analysis in the frequency domain, the morphological decomposition technique

can localise features in the time domain. By morphologically decomposing the signal, the asymmetric features of the inrush signal can the enhanced, whereas other irrelevant components may be attenuated, to allow the pattern of the gaps between successive waveforms to be extracted and identified.

The other study described in this thesis originates from the area of neonatal intensive care, where it was observed that during repeated asphyxia, the electrocardiogram (ECG) waveform of fetal sheep exhibits increases in certain parameters, accompanied by deviation of the ST segment. Researchers in paediatrics hypothesised that similar waveform variations may occur when the human fetus is compromised by similar situations [15].

Although the ECG signal is determined by its shape, i.e., it is a time-domain encoded signal, most of the linear approaches traditionally used are based on frequency domain filtering. Moreover, while ECG monitoring and interpretation have been well studied and established in human adults, it is difficult to achieve baseline correction solely by means of linear filtering, without introducing considerable distortions to the ECG waveform [16]. In neonatal ECG, in addition to the higher level of disturbances from muscular activities and respiration [17], there is also a surprising variation in the heart rate and diversity of waveform morphology, which will further extend the ECG spectrum. Therefore it is very difficult to determine a predominant spectrum and the corresponding cut-off frequency for linear filtering.

Morphological approaches have been proposed in literature, to remove impulsive noise and baseline wander [1], as well as to detect the QRS complex from ECG signals [18]. A variant of this method has been applied to QRS complex detection. Although this approach is very effective in terms of robustness and computational efficiency, it introduces distortions to the PR and ST segments. It is likely that this distortion comes from the singularity of the QRS complexes. Therefore it may be possible to achieve a better processing result, if the QRS complexes are detected and removed before morphological

processing, with incorporation of subject information, e.g., the heart rate, into the filtering algorithm.

1.1.2 Origin and historical notes of MM

The word *morphology* stems from the Greek meaning "study of form" [19]. It has been used to designate a new branch of mathematics - *mathematical morphology* (MM) - whose goal is to investigate the geometrical structure of sets. "It is *mathematical* in the sense that the analysis is based on the set theory, topology, lattice algebra, random functions, etc., and it is called *morphology* since it aims at analysing the shape and form of the objects" [20].

The name and concept of MM were introduced in 1966 by Matheron [4] and Serra [5] [6] at the Paris School of Mines in Fontainebleau, from their research on petrography and mineralogy, including investigation of the relationship between the geometry of porous media and their permeabilities, and quantification of the petrography of iron ores in order to predict their milling properties. The original theoretical work of Matheron and Serra as a quantitative description of shape and size was initially used for binary images, comprised of a set algebra which includes four basic transformations: erosion, dilation, opening and closing. The dilation was originally proposed by Minkovski in order to characterise integral measures of certain ill-behaved sets, and is sometimes referred to as the "Minkovski set addition" [21]. The erosion, however, was not proposed until much later by Hadwiger [22], and is sometimes referred to as the "Minkovski set subtraction". The opening and closing, formed by compositions of erosion and dilation, were proposed by Matheron [4]. The class of *morphological transformations* was then defined to be the collection of all set transformations generated by unions, compositions, and complementations of erosions and dilations [23]. Finally, the ubiquity of the morphological transformations was demonstrated by Matheron [4] [24], who proved that any

translation-invariant and increasing transformation can be represented as a union of erosions, defined in the complete lattice [25].

MM has been proved to be a well defined methodology which is applicable to a wide variety of problems, and attracts attention from researchers with completely different backgrounds. However, in practice, like other image processing tools, MM requires huge computational power, especially in real-time applications. Various implementations of a general MM system were proposed [26] [27] [28]. Haralick [29] addresses some applications of morphological filtering, e.g., the Golay logic processor [30], Diff3 [31], PICAP [32], the Leitz Texture Analysis System (TAS) [33], the CLIP processor arrays [34], and the Delft image processor (DIP) [35]. A cellular neural network (CNN) based morphological system was also proposed recently [36].

With over three decades of development, MM has become an important formalism in signal/image processing and computer vision and a powerful tool for geometrical shape analysis [7]. MM provides an approach which is by means of geometrical transformations based on the shape of objects. When acting upon complex shapes, morphological operations are able to decompose them into meaningful parts and separate them from the background, while preserving the main shape characteristics. Therefore, such an algebraic system with its operators and their combinations allows the underlying shapes to be identified, reconstructed and enhanced from their noisy, distorted forms.

1.2 The concepts of MM

Appropriate MM operations, as nonlinear transformations, tend to simplify signal/image data by modifying geometrical features of signal/image locally, to eliminate irrelevancies while preserving the essential shape characteristics.

The foundation of MM is laid on set theory in which a set of pixels define a signal/image object; the geometric structure of objects is extracted via the

use of other objects called *structuring elements* (SE). Information pertaining to the size, spatial distribution, shape, connectivity, convexity, smoothness, and orientation can be obtained, by means of applying various SEs to the original object with operations derived from set theory [7].

Like any signal/image processing theory, MM has a perspective which allows it to focus on certain phenomena within signal/images. It considers objects using set theory and geometry, thus distinguishing itself from other signal/image processing theories, e.g., syntactic theories based upon generative grammars and signal processing theories based upon Fourier analysis. The SE, as a probe, slides through the image as a moving window, inspects its interaction with the image, and detects specific features in the neighbourhood of every point of the image. Therefore a priori knowledge of the information content of the image can help to choose a proper SE [7].

Usually, MM transformations constitute an intermediate part of the processing sequence. In the first phase the inputs are digitised and pre-processed using local convolution operators and segmented to separate objects from the background. Being used as the second phase, MM operations act on the shape of these objects. Finally the last step evaluates the results using different numerical descriptors or a syntactic approach. MM operations are predominantly used for following purposes

- Signal/image pre-processing (noise filtering, shape simplification)
- Enhancing object structure (skeletonising, thinning, thickening, convex hull, object marking)
- Quantitative description of objects (area, perimeter, projection).

1.3 MM versus linear filtering

It is mentioned by Serra that "When one scrutinises the behaviour of the scientists who access morphological filtering for the first time, a number of

their reactions, more or less implicitly, refer to linear processing. They tend to extrapolate, if not the results, at least the style and the a priori of the linear approach. Progressively then, they usually set themselves free from these crutches." [37]

Within the framework of traditionally non-morphological methods, which is similar to calculus and based on point spread function concepts and linear transformations, e.g., convolution and its frequency domain representation, we may describe any function as a sum of harmonic components, therefore enabling the "undoing" of noise corruption by filtering, i.e. convolving with some kernel functions. Similarly, what the algebra of convolution does for linear systems, so the algebra of MM does for shape. Moreover, compared with non-morphological systems, MM only involves comparisons for finding maxima/minima, or addition/subtraction in some specific case for grey-scale signals/images, and Boolean operations for binary ones, thus making it significantly faster in calculation than the multiplication and addition being used in convolution for linear transformation. Some major differences between the two approaches are given briefly in Table 1.1.

Features	MM	Convolution
Reversibility	No	Yes
Unique algebraic structure	No	Yes
Idempotence and loss of information	Yes	No
Defined in complete lattice	Yes	No
Iteration	Yes	No
Flatness $\psi(\log(f)) = \log(\psi(f))$	Yes	No

Table 1.1: Morphological filtering versus convolution

The difference between the two techniques can be summarised as described by Boomgaard [7] "In linear image processing the basic underlying assumption

is the superposition of visual stimuli. The visual signal is thought of as the weighted addition of basic signals. This assumption of linearity is questionable in case the image is formed by projection, where one object completely hides another object behind it. Due to using non-linear transformations, it is impossible to reconstruct the original image."

1.4 Overview of this thesis

This thesis is structured as follows:

Chapter 2 introduces the theoretical background of MM. It starts with a review of a number of basic morphological operators such as dilation, erosion, opening and closing, and a brief discussion about the relation between such nonlinear operators. The theory of grey-scale morphological operators is also covered.

Chapter 3 presents an MM based inrush current restraint algorithm for designing power transformer protection relay. A brief introduction to the inrush current is given, followed by the descriptions of existing detection methods and the difficulties associated with them. The proposed technique is then described, which is to discriminate the inrush current from internal fault conditions by using MM transforms to extract the singularity associated with the asymmetric inrush waveform, while attenuating other irrelevant features. By quantifying the extracted features, the inrush current is then identified with simple criteria. The results of applying the MM approach to simulated signals and waveforms recorded from physical transformers are given, which indicate that the proposed algorithm is fast and reliable, and may be considered as an alternative method in designing and implementing a digital relay.

Chapter 4 presents a set of morphological algorithms for normalising, processing and analysis of the neonatal ECG signal. Following an introduction and definition of the terms in ECG, a morphological filtering scheme that adapts to subject specific parameters is described, to estimate and remove baseline wander from the signal with less distortion to the waveform. The normalised signals are then processed to obtain a set of ECG measurements. The studies are conducted on ECGs with simulated interference and also on actual noisy ECG records. The results obtained are investigated.

Chapter 5 presents the design and implementation of an integrated system for on-line automatic analysis of the neonatal ECG signal, based on the algorithms described in Chapter 4. The proposed system allows the system to be used in clinics by persons without a detailed knowledge of the technology. It covers the optimisation and implementation of basic morphological operators, code design and hardware integration, with emphasis on a generic architecture which is able to accommodate future improvement and extension without major revision of the code.

Chapter 6 describes the pilot trial conducted on the ward for the system described in Chapter 5. The design of the trial and the results obtained are given and investigated, focusing on the accuracy of the ECG measurements and the relationship between the waveform morphology and the gestational ages of the babies.

Chapter 7 concludes this thesis and discusses the limitation of the proposed morphological techniques. Suggestions for possible future work that can be investigated are also given.

Appendix A describes the CRIB score used in clinics for simplifying and refining the assessment of neonatal mortality and morbidity.

Appendix B encloses the clinical data of the babies monitored in the pilot trial.

Appendix C includes the original and statistical results of the pilot trial described in Chapter 6.

1.5 Contributions of research

The major contributions arising from this research are the utilisation of the advanced performance of MM for feature enhancement, extraction, noise suppression and background normalisation, by introducing morphological approaches to problems on power transformer protection and neonatal ECG signal processing.

This thesis describes, for the first time, original work on the application of MM to power system protection relays [38]. It is focused on the identification of transformer inrush current. The proposed technique is fundamentally different from conventional methods, as it decomposes the signal based on time domain features instead of in the frequency domain. Since it works directly upon the geometric characteristics of the input, there is no need for abstract transform techniques such as Fourier, Laplace, and Hilbert transforms, nor is there a requirement for transform-world concepts such as frequency, convolution, effective bandwidth and ripple.

The results obtained confirm that the proposed method provides reliable identification of inrush, in both cases when the current transformer is saturated or there are only low levels of the second harmonic content [39]. It also reduces the computational complexity by using nonlinear morphological operations. The classification scheme is a simple yet effective means to assign an observed signal to a particular group [40]. Moreover, it provides flexibility in the choice of SE, which can be adjusted by modifying its shape.

As the second application of MM, a morphological method for processing and measuring neonatal ECG signals is introduced, with improvements to an existing morphological approach for baseline correction. The proposed algorithm is used to obtain the QRS complex before baseline correction, and further to incorporate the heart rate information into the morphological baseline correction algorithm [41].

The performance of the algorithm is investigated using simulated neonatal ECGs with artificial noise and baseline wander, and compared with experimental signals acquired from infants nursed in a special care baby unit. The result of this comparison suggests that a substantial improvement in the SNR (Signal to Noise Ratio) over existing approaches is achieved, and the distortion of the ECG waveform can be greatly reduced [42].

Compared to linear filtering, which will suppress any signal with frequency lower than the designated cut-off frequency, the proposed morphological technique has very high performance in preserving shapes that contain various frequency components. Moreover, it is also efficient in terms of computational load. By using a specially designed structuring element for the morphological operators, the amount of computation can be reduced as the only calculation involved is to find local maxima/minima.

An integrated neonatal ECG analysis system, which implements the above morphological filtering techniques, is also described in this thesis. The system is designed to aid neonatologists in diagnosing complicated cases, conducting research, archiving important results, creating an electronic ECG data bank etc. It is preferred when high-precision electrocardiography is needed, especially in the case of neonatal ECGs that have a higher heart rate than adults. It also aims to be a valuable tool for computerised analysis, particularly as it allows the user to examine the reliability of the results. Important features like ST segment measurement, trend analysis and cardiac vector calculation provide the opportunity of adding diagnostic power to the routine examination

and the standard interpretive features. Theoretical support, algorithm development, interaction with physicians, hardware and software design, debugging, system validation are integrated in this system, which provides flexibility and modularity, and is continuously upgradable. This is the first step in developing a commercial system for monitoring the blood supply to the babies by means of analysis of the ECG signals.

To validate the morphological techniques proposed in Chapter 4, as well as to assess the robustness of the integrated neonatal ECG analysis system, a set of experiments were also devised and carried out in clinical environment. The general variability of ECG measurements was obtained, and the system was delivered for use as a clinical research tool, which will facilitate further study of the neonatal ECG.

Chapter 2

Introduction to mathematical morphology

The previous chapter briefly discussed the concepts of MM. This chapter introduces the theoretical background of MM, focuses on the definitions of the operators that will be used in later chapters, including dilation, erosion, opening, closing and their extension on grey-scale signals.

2.1 Background notions

As one can imagine, there are many ways to approach the description of phenomena that are distributed over space, and which exhibit a certain spatial structure. One such approach is to consider them as objects, i.e., as subsets of their space of definition. Based on this point of view, the concepts and principles of MM have been developed, which exploit point set properties, and can be generalised as integral geometry and topology.

Sets in MM represent the shapes that appear in signals/images. In Euclidean 2-space, sets denote the foreground regions in binary images; sets in 3-space may denote time-varying images, static grey-scale images or binary

solids. Further, in higher dimensional spaces, sets may include additional information such as colour or multiple perspective imagery .

A fundamental feature of MM is the use of a *structuring element* (SE), which is a points set that is usually smaller and simpler than the original input signal/image, and can be regarded as a probe that MM uses to extract information about the geometrical structure of an object [43] [44]. Depending on the different shapes of SE and their specific operation sequences, useful geometrical information of the signal/image, such as size, spatial distribution, connectivity, convexity, smoothness and orientation can be extracted.

2.2 Basic morphological operators

2.2.1 Dilation and erosion

The basic operators in MM are dilation and erosion; other operators, such as opening and closing, are built using the combination of dilation and erosion. In a crude sense, dilation expands an image, while erosion results in a contraction.

Given two sets $X, Y \subseteq \mathbb{E}^d$, where $\mathbb{E}^d$ is $d-$ dimensional Euclidean space, the *Minkowski addition and subtraction* [21] are defined respectively as

$$X \oplus Y = \{x + y \mid x \in X, y \in Y\}$$

$$X \ominus Y = \{h \mid h + y \in X \forall y \in Y\}.$$

These operations form the basic ingredients of MM. Choose a fixed set $A \in \mathbb{E}^d$ as the SE, then the dilation and erosion over the input image X, denoted by δ_A, ε_A respectively, are given by

$$\delta_A(X) = X \oplus A$$

$$\varepsilon_A(X) = X \ominus A.$$

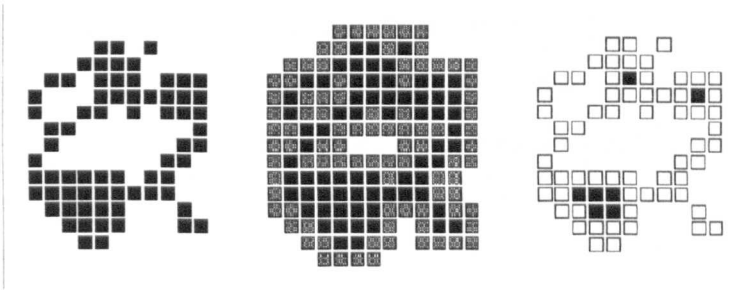

Figure 2.1: Original image (left), dilated (middle), eroded (right) by a 3×3 square SE.

Figure 2.1 illustrates the effects of both operators. By using the notation $X_y = \{x + y \mid x \in X\}$, which is the translation of X along the vector y; and $\check{A} = \{-a \mid a \in A\}$, the transpose of A with respect to the origin, alternative representations of dilation and erosion can be defined as:

$$X \oplus A = \bigcup_{a \in A} X_a = \{h \in \mathbb{E}^d \mid \check{A}_h \cap X \neq \varnothing\}$$

$$X \ominus A = \bigcap_{a \in A} X_{-a} = \{h \in \mathbb{E}^d \mid A_h \subseteq X\}.$$

The basic property of dilation is

$$(\bigcup_{i \in I} X_i) \oplus A = \bigcup_{i \in I} (X_i \oplus A),$$

for every collection $X_i, i \in I$, of subsets of $\mathbb{E}^d$. In other words, dilation is distributive over union. Dually, erosion is distributive over intersection:

$$(\bigcap_{i \in I} X_i) \ominus A = \bigcap_{i \in I} (X_i \ominus A).$$

Let $X, Y, A, B \subseteq \mathbb{E}^d, h \in \mathbb{E}^d$, and $r \in \mathbb{E}$; other basic properties of dilation are listed as follows:

$$\begin{aligned} (X \oplus A)_h &= X_h \oplus A \\ (X \oplus A) \oplus B &= X \oplus (A \oplus B) \\ X \subseteq Y &\Rightarrow X \oplus A \subseteq Y \oplus A \\ rX \oplus rA &= r(X \oplus A). \end{aligned}$$

The first property expresses that dilation is translation invariant: an operator ψ is called *translation invariant* if $\psi(X_h) = [\psi(X)]_h$, for $X \subseteq \mathbb{E}^d, h \in \mathbb{E}^d$. The second property provides a means to decompose structuring elements into smaller parts. The third property means that dilation is an increasing operator: an operator ψ is called *increasing* if $X \subseteq Y$ implies $\psi(X) \subseteq \psi(Y)$. Most of the operators we discussed here and later are increasing. In the last property, rX denotes the multiplication $\{rx \mid x \in X\}$, it means that dilation is invariant under scaling.

For erosion, similar properties hold as follows:

$$\begin{aligned} (X \ominus A)_h &= X_h \ominus A \\ (X \ominus A) \ominus B &= X \ominus (A \oplus B) \\ X \subseteq Y &\Rightarrow X \ominus A \subseteq Y \ominus A \\ rX \ominus rA &= r(X \ominus A). \end{aligned}$$

Dilation and erosion are *dual* operators in two different perspectives. First, the following relation holds for dilation and erosion:

$$(X \oplus A)^c = X^c \ominus \check{A} \text{ and } (X \ominus A)^c = X^c \oplus \check{A},$$

where X^c is the complement of X. Therefore, dilating a set has the same effect as eroding its complement(with transposed SE). Finally, dilation and erosion are dual in the sense that they satisfy the *adjunction* relationship:

$$Y \oplus A \subseteq X \iff Y \subseteq X \ominus A, \tag{2.2.1}$$

for all $X, Y \subseteq \mathbb{E}^d$.

2.2.2 Opening and closing

Morphological operators discard information. In general, it is not possible to recover the original image after dilation or erosion. If one erodes an image X with a SE A and subsequently dilates it with the same SE, the final result

will be smaller than the original one. This can easily be proven using the adjunction relation (2.2.1): substituting $Y = X \ominus A$ we get $(X \ominus A) \oplus A \subseteq X$. The operator

$$\alpha_A(X) = X \circ A = (X \ominus A) \oplus A$$

is called the *(structural) opening* of X by A. Dually, first dilating, then eroding, yields a set $(X \oplus A) \ominus A$ which is larger than X. The operator

$$\beta_A(X) = X \bullet A = (X \oplus A) \ominus A$$

is called the *(structural) closing* of X by A. Furthermore, we have

$$((X \ominus A) \oplus A) \ominus A = (X \circ A) \ominus A \subseteq X \ominus A$$

$$((X \ominus A) \oplus A) \ominus A = (X \ominus A) \bullet A \supseteq X \ominus A.$$

Combining both inclusions, we arrive at the identity

$$((X \ominus A) \oplus A) \ominus A = X \ominus A.$$

And dually, we have

$$((X \oplus A) \ominus A) \oplus A = X \oplus A.$$

In particular, these relations yield

$$(X \circ A) \circ A = X \circ A \text{ and } (X \bullet A) \bullet A = X \bullet A.$$

Thus we have shown that opening and closing by A are idempotent operators. An operator ψ is *idempotent* if $\psi^2 = \psi$. Also, following alternative definitions of opening and closing express their geometric properties:

$$X \circ A = \bigcup \{A_h \mid h \in \mathbb{E}^d \text{ and } A_h \subseteq X\},$$

$$X \bullet A = \{h \in \mathbb{E}^d \mid h \in \check{A}_y \Rightarrow \check{A}_y \cap X \neq \varnothing\}.$$

Furthermore, opening and closing are each other's negative, i.e.,

$$(X \circ A)^c = X^c \bullet \check{A} \text{ and } (X \bullet A)^c = X^c \circ \check{A}.$$

Openings and closings are used for many different purposes, e.g., the enhancement of images that are distorted by noise; a number of applications can be found in [5]. In Figure 2.2, we illustrate the effects of opening and closing on an original image using a symmetric 3×3 SE with its origin at the centre.

Figure 2.2: Original image, opening, closing by 3×3 square.

2.3 Grey-scale morphological filters

Grey-scale (GS) digital signal can be represented as sets whose components are in Z^2, the discrete Euclidean space. In this case, one element refers to the co-ordinates of a sample, and the other refers to its discrete intensity value. In this section the operators are assumed to be grey-scale unless specified, and to generalise the idea, we will assume grey-scale is not restricted to the range 0-255, but any integer number unless specified.

Let $f(n)$ and $g(n)$ denote respectively an 1-D GS structuring element (GSE) of length L, D_f and D_g denote their domains. 1-D GS erosion, dilation, opening and closing, denoted respectively by $(f \ominus g)(n), (f \oplus g)(n), ((f \ominus g) \oplus g)(n)$ and $((f(\oplus g) \ominus g)(n)$, are defined as follows.

$$\begin{aligned}
(f \ominus g)(n) &= \min_v\{f(n+v) - g(v)\} \\
(f \oplus g)(n) &= \max_v\{f(n-v) + g(v)\} \\
((f \ominus g) \oplus g)(n) &= \max_v\{\min_u\{f(n+u-v) - g(u) + g(v)\}\} \\
((f(\oplus g) \ominus g)(n) &= \min_v\{\max_u\{f(n-u+v) + g(u) - g(v)\}\},
\end{aligned}$$

where $u, v \in D_g$ and $f(\alpha), \alpha \in D_f$. If the structuring element is flat (i.e., $g(k) = 0, \forall k \in D_g$), then the above equations can be simplified to:

$$\begin{aligned}
(f \ominus g)(n) &= \min_v\{f(n+v)\} \\
(f \oplus g)(n) &= \max_v\{f(n-v)\} \\
((f \ominus g) \oplus g)(n) &= \max_v\{\min_u\{f(n+u-v)\}\} \\
((f(\oplus g) \ominus g)(n) &= \min_v\{\max_u\{f(n-u+v)\}\},
\end{aligned}$$

The above equations can easily be extended to 2-D, and moreover, to $n-D$.

The properties of GS MM operators are similar to binary operation for translation, transpose and complement, as follows:

1. *GS translation:* The translation of a function f by k is defined as

$$f(n)_k = f(n+k).$$

2. *GS transpose:* The transpose $\check{f}$ of a function f is defined as

$$\check{f}(n) = f(-n).$$

3. *GS complement:* The complement f^c of a function f is

$$f^c(n) = -f(n).$$

4. *GS (anti-)extensivity:* GS dilation (erosion) is extensive (anti-extensive) if the value of the origin of SE is non-negative:

$$g(0) \geq 0 \Rightarrow f \ominus g \leq f \leq f \oplus g.$$

GS opening is always anti-extensive $f \circ g \leq f$ and GS closing is always extensive $f \leq f \bullet g$, and

$$g(0) \geq 0 \Rightarrow f \ominus g \leq f \circ g \leq f \leq f \bullet g \leq f \oplus g.$$

2.4 Summary

In this chapter the basic operators involved in MM were defined, mainly as binary or grey-scale. It is realised that there are only two basic operators: dilation and erosion, and the rest of the operators can be obtained by proper combinations of them. More relations of morphological operators have also been given. The operators opening and closing have been shown to be anti-extensive and extensive, respectively. It has also been shown that morphological filters can be easily developed in higher dimensions too.

Chapter 3

Morphological method for power transformer inrush current detection

In this chapter, an MM based inrush current restraint algorithm is presented. A brief introduction to transformer magnetising inrush is given, followed by a brief description of existing detection methods and the associated difficulties. The proposed technique is then described, which is to identify the inrush current by using MM transforms to extract the singularity peculiar to the asymmetric inrush waveform, while attenuating other irrelevant features. By quantifying the extracted features, the inrush current is then identified using a set of simple criteria. Results of applying the MM approach to simulated signals and waveforms recorded from physical transformers are given and investigated.

3.1 Introduction

The continuity of power transformer operation has been recognised as being of vital importance in maintaining the reliability of electric power systems, where the protection of large power transformers still remains one of the most challenging problems in the area of power system relaying.

Digital protection relays for power transformers offer many advantages such as reliability, flexibility, high performance, post fault recording and low cost. Several factors have to be considered when designing such a relay, including the magnetising inrush during the energising process, the over-excitation condition resulting from dynamic over-voltage, tap changing, current transformer (CT) saturation, internal, ground and external faults, etc.

The differential protection principle, employed by most digital relays, is so far the primary protection for large power transformers [8]. It detects all types of internal fault while blocking trip signals caused by the magnetising inrush, over excitation and external faults, etc. Previous studies have shown the harmonic components that exist in the inrush currents [9]. Because of its dominance, the second harmonic has been utilised by most conventional relays to block the trip signal triggered by inrush. Gap detection is another widely used method [45]. Alternatively there are also applications using wavelet transforms [46], frequency transient detection [12] and artificial neural networks [13] [14].

Security problems may arise with the advances in power transformer capacity and manufacturing technology. In certain cases of magnetising inrush, the second harmonic may reduce to a considerably lower level [10], whereas in other cases the harmonic content of the fault current may increase to such a magnitude that discrimination between inrush and fault condition solely by means of the harmonic constraint is not possible [11]. Moreover, the gap detection technique is subject to the assumption that there exists an explicit gap

in every cycle of the waveform [47]. In conditions where the CT is saturated by the inrush current, the distortion introduced to the gap may result in a false tripping; whereas during severe internal faults, the secondary current waveform of the saturated CT may exhibit periods of low and flat values similar to the gap, resulting in the relay missing operations.

3.2 The magnetising inrush

3.2.1 Introduction to magnetising inrush

Magnetising inrush currents in power transformers result from any abrupt change of the magnetising voltage. Although usually considered as the result of energising a transformer, the magnetising inrush may also be due to [48] [49]:

1. occurrence of an external fault;
2. voltage recovery after clearing an external fault;
3. changes of the character of an external fault;
4. out-of-phase synchronising of a nearby generator;

The magnetising current disturbs the balance between the currents at the transformer terminals, and is therefore identified by the differential relay as a "false" differential current. The relay, however, must remain stable during inrush conditions. In addition, considering the transformer lifetime, tripping out during an inrush condition is a very undesirable situation (breaking the current of a pure inductive loading generates high over-voltage that may jeopardise the insulation of the transformer and be the indirect cause of an internal fault).

Initial magnetising due to switching a transformer on is considered as the most severe case of an inrush. When a transformer is de-energised, the magnetising voltage is disconnected and the magnetising current reduces to zero

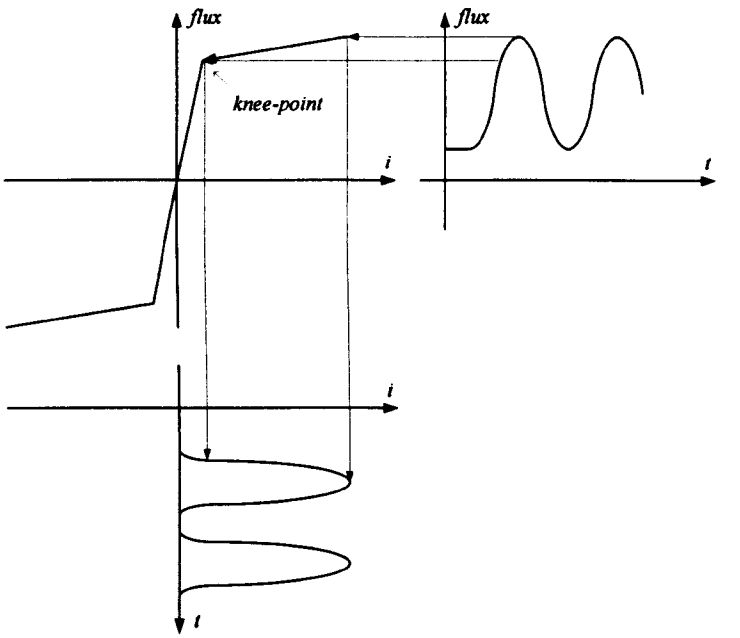

Figure 3.1: Illustration of the magnetising inrush

while the flux follows the hysteresis loop of the core. This results in certain remanent flux in the core. When, afterwards, the transformer is re-energised by an alternating sinusoidal voltage, the flux will be biased by the remanence. The residual flux can be as high as 80–90% of the rated value [10], and therefore, it may shift the flux-current trajectories far above the knee-point, resulting in both large peak values and strong distortion to the magnetising current, as illustrated in Figure 3.1.

A typical inrush current waveform is given in Figure 3.2, where a large and long lasting DC component can be observed, which has large peak values at the beginning and decays substantially after a few tenths of a second, but only decays fully after several seconds. The shape, magnitude and duration of the inrush current depend on several factors, including:

1. the size of the transformer,
2. the impedance of the energising system,

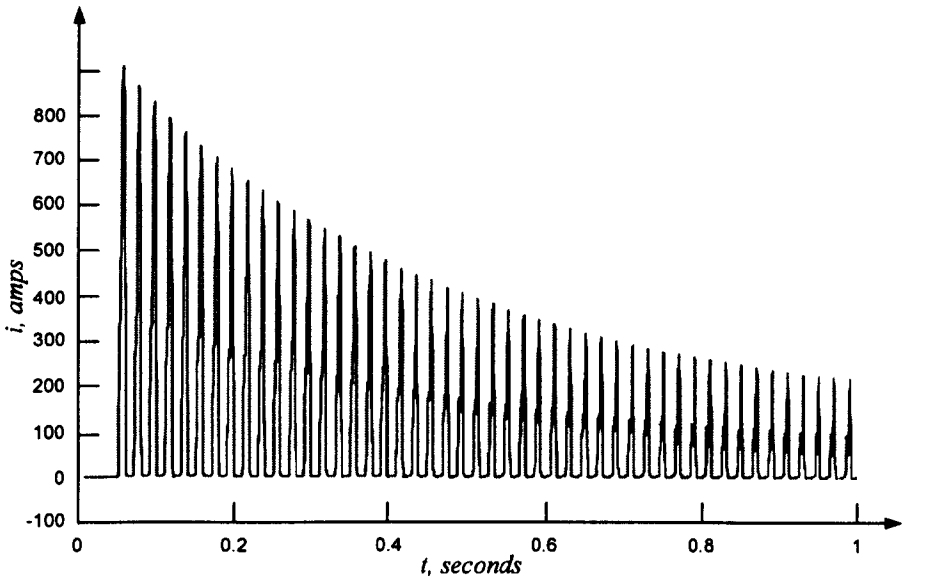

Figure 3.2: A typical inrush current waveform

3. the magnetic properties and remanence of the core,
4. the phase angle when the transformer is switched on.

A detailed discussion about how these factors affect the inrush waveform can be found in [49].

3.2.2 Waveform and harmonics of the inrush current

For a single-phase transformer, to obtain the frequency spectrum of the inrush waveform, an analytical approximation of the inrush waveform is given in Figure 3.3. The waveform between $-\alpha$ and α is the inrush current due to saturation of the transformer air core; between α and $2\pi - \alpha$ the intermittent angle of the waveform, known as the *gap*. The angle α is used to facilitate the modelling of an actual inrush current.

The amplitude of the n-th harmonic, A_n, of the waveform shown in Figure 3.3 can be calculated as

$$A_n = \frac{I_m}{\pi}\left[\frac{1}{n+1}\sin((n+1)\alpha) + \frac{1}{n-1}\sin((n-1)\alpha) - 2\cos(\frac{\alpha}{n})\sin(n\alpha)\right] \quad (3.2.1)$$

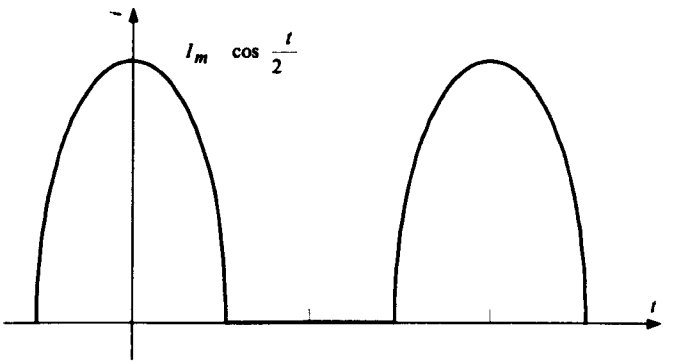

Figure 3.3: An idealised inrush current waveform for the spectral analysis

where I_m is the peak value of the inrush current i [49].

Figure 3.4 presents the spectrum of the signal shown in Figure 3.3, calculated by using (3.2.1) with $\alpha = 60, 90$ and 120 degrees, respectively. It is clear that the second harmonic always dominates because of the large DC component. However, the amount of the second harmonic may drop below 20%. The minimal content of the second harmonic depends mainly on the knee-point of the magnetising characteristic of the core, the lower the saturation flux density, the higher the amount of the second harmonic. Modern transformers built with improved magnetic materials have high knee-points, and therefore, their inrush currents display a relatively low amount of the second harmonic. Since the second harmonic is the basic restraining criterion for stabilising differential relays during inrush conditions, certain difficulties may arise when protecting these transformers [50], as discussed in following sections.

Inrush currents measured from a three-phase transformer may differ considerably from the above mentioned single phase transformer, as:

1. the angles of the energising voltages are different in different phases;
2. when a delta-connected winding is switched in, the line voltages are applied as the magnetising voltages;
3. in the above case the line current in a given phase is the vector sum of the other two windings' currents;

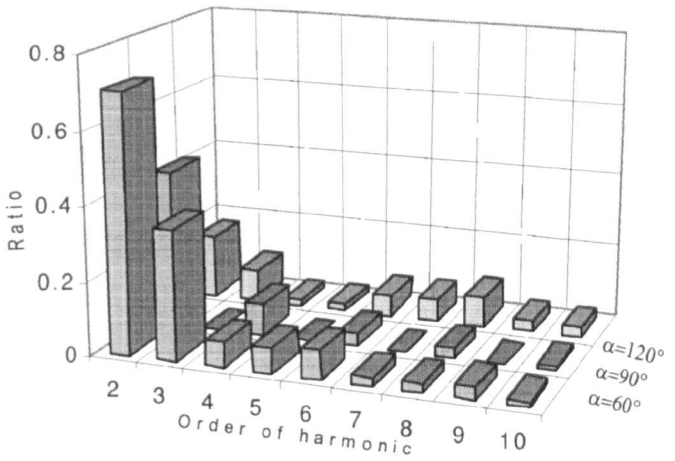

Figure 3.4: Harmonic content of the idealised inrush current with $\alpha = 60, 90$ and 120 degrees

4. depending on the core type and other conditions, it is possible that only some of the core legs are saturated.

Therefore, for the current in a given phase or a grounded neutral, it is either similar to the single-phase inrush pattern (as shown in Figure 3.2), or becomes a distorted but oscillatory waveform. In the latter case, the amount of the second harmonic may drop dramatically, which causes problems for differential relaying. In Figure 3.5, which illustrates the waveforms of energising a three-phase transformer, the currents in phases A and B exhibit typical rectified inrush pattern, whereas phase C is an oscillatory waveform.

3.2.3 Magnetising inrush current with saturated current transformer

Due to the large and slow decaying DC component, the inrush current waveform is likely to be distorted by the saturation of the built-in instrumental current transformer (CT) of the relay. In such a condition, the CT's secondary current may exhibit a certain level of distortion (see Figure 3.6), with considerably reduced amount of the second harmonic [51], and in the most adverse

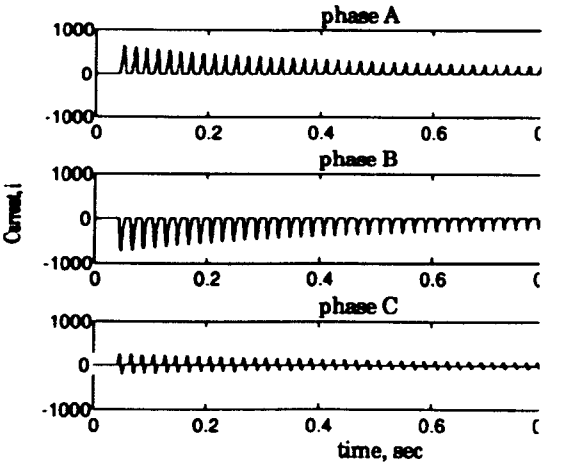

Figure 3.5: Sample inrush currents in a three-phase transformer

conditions the gap disappears.

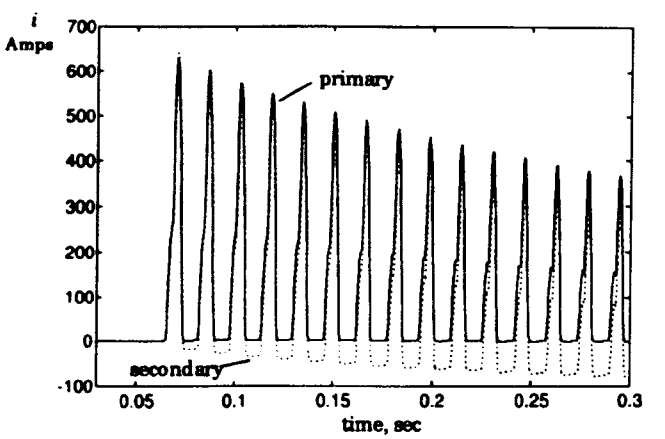

Figure 3.6: The primary and secondary currents of a saturated CT

3.3 Existing methods for detecting inrush current waveform

Modern means of restraining differential relays during magnetising inrush conditions recognise the inrush pattern either indirectly (harmonic analysis) or

directly (waveform analysis) [52].

The harmonic restraint method is the classical way to restrain the relay from tripping during magnetising inrush conditions. As aforementioned, the inrush current is rich in harmonics, and generally, low levels of harmonics enable tripping, while high levels indicate inrush and restrain the relay. For digital relays this may be written as

$$T = \text{true when } I_{CH} < \delta I_{CD} \tag{3.3.1}$$

where

T: Tripping permission from the inrush detector;

I_{CH}: Combined harmonic component in the differential current;

I_{CD}: Combined differential current;

δ: threshold.

The condition given in (3.3.1) originates a whole family of algorithms using a variety of approaches for combing currents I_{CH} and I_{CD}.

In the simplest approach, the amplitude of the second harmonic is considered as the combined harmonic signal, while the amplitude of the fundamental frequency component in the same phase is used as the combined differential current.

Harmonic restraint in general, regardless of the method of composing the combined harmonic and differential signals, displays certain limitations. First, the estimator of the harmonic component (usually the second harmonic only) needs a certain amount of time for accurate estimation of the amplitude. Even if the harmonic is not present in the differential signal at all, the ratio of I_{CH} to I_{CD} in (3.3.1) is initially significantly overestimated (until the fault data fills out the estimator data window). This means that the harmonic restraint usually will not permit tripping for a time approximately equal to the data window length of the estimators (typically one cycle). Second, as aforementioned, in

modern transformers the proportion of higher harmonics in the magnetising current may drop well below 10% (the second harmonic can be as low as 7%, while the total harmonic content is at a level around 7.5% [10] [53]. Under such circumstances, the setting δ in (3.3.1) should be adjusted to be under 7%. This may lead to, however, delayed or even missing operations of the relay, due to the harmonics in the differential currents during internal faults accompanied by saturation of the CTs. Third, the second harmonic ratio may temporarily (for several cycles) drop below the threshold of 20% used in most relays[54].

For waveform based restraining methods, the most commonly used technique is to detect the periods of low and flat values, i.e., the gap, in the waveform. In this method, the hypothesis of magnetising inrush may be ruled out if the differential current does not include in its every cycle a period, which lasts no less then 1/4 of a cycle while its shape is both flat and close to zero. This relaying principle was known in the era of static relays and there are certain analogue schemes developed for implementing it [54] [55].

This form of direct waveform restraining regardless of its implementation shows weakness [49]. First, the recognition of an internal fault versus magnetising inrush takes one full cycle. Second, The CTs, when saturated during inrush conditions, change the shape of the waveform within the gap period (see Figure 3.6) and may cause a false tripping. Third, during severe internal faults, when the CTs are saturated, their secondary currents may also show periods of low and flat values, causing the relay to miss operations.

3.4 Morphological approach for inrush signal detection

3.4.1 Extraction of the asymmetric features

To extract the asymmetric features associated with the inrush current, morphological signal decomposition [56] [57] is employed to separate the waveform into various levels of detail. Let f be a signal; to decompose f as $f = \sum_i f_i$ with a set of components $\{f_i, i = 1, 2, \ldots, \}$, a constructive transform can be applied for obtaining a family of residues of f. If the residue of two transforms, ϕ and ψ, is defined as $R_{\{\phi,\psi\}}(f) = \phi(f) - \psi(f)$, with an anti-extensive and positively defined transform γ, the general representation scheme can be defined as:

1. The family of residues of f with respect to γ is $\{r_i, i = 1, 2, \ldots, \}$, where $r_1 = f$ and $r_{i+1} = R_{\{r_i, \gamma(r_i)\}}$ until $\gamma(r_i)$ is a null signal.

2. The set $\{f_i\}, f_i = \gamma(r_i)$ is the residual representation of f with respect to the constructive transform γ. The reconstruction f^* of f can be obtained as $f^* = \sum_i f_i$. The partial j-components reconstruction is given by $f_j^* = \sum_{i=1}^{j} f_i$.

The family of residues can be considered as the result of the identity transform $I(r) = r$ and the constructive transform γ. When the constructive transform is recursively applied to the signal, a residue family can be uniquely determined. With j partial reconstruction, f can be represented in arbitrary levels of detail. The reconstruction is nondecreasing by definition, when the final residue r_{j+1} is null, a complete reconstruction f_j^* can be obtained since $f = f_j^* + r_{j+1}$. A non-converging reconstruction can appear if r_{j+1} is not null and the transform $\gamma(r_j)$ is a null function. Its error has to be determined.

There are a large number of transforms fulfilling the above constraints. For our studies of inrush current identification, one of them should be chosen such that the corresponding residual representation is optimal, when the signal is partially reconstructed, in obtaining the singularities peculiar to the inrush signal.

Morphological erosions and openings are anti-extensive transforms if their structuring functions satisfy $g(0) > 0$. Furthermore, they are constructive transforms if the region of support of the erosion $[f \ominus kg](x)$ is limited to those points x of the domain for which $[f \ominus kg](x) \geq 0$ [56]. Let r_{kg} be the family of openings of r with kg, the homothetics of a structuring function g. As k increases, the openings are more simplified version of the original function and the details that are less than kg are discarded. This reason suggests to us the selection of the maximal scale opening as the constructive transform. If κ is the corresponding maximal value of k, the constructive transform is $\gamma(r) = \max_k(r_{kg}) = r_{\kappa g}$. Following the approach mentioned above, the definition of morphological signal decomposition is recovered. [56] The family of residues is $r_{i+1} = R_{\{r_i, r_{\kappa_i g}\}}$ and the components of the representation are

$$f_i = \gamma(r_i) = (r \ominus \kappa_i g) \oplus \kappa_i g. \tag{3.4.1}$$

Information on the shape of the signal is captured by g while κ_i provides information on size. The components are maximal functions in the sense that they describe the largest scaled version of the structuring function g that can still be fitted inside the current residue. The maximal structuring function is an invariant for the residue. The support of the components f_i are the functions $l_i, l_i = r_i \ominus \kappa_i g$. By using l_i functions, one can get $f_i = l_i \oplus \kappa_i g$. The function l_i represents the loci of the centres of the maximal structuring function in the current residue; l_i is positive on its domain. The reconstructed f is given by

$$f^* = \Sigma_i f_i = \Sigma_i (r_i \ominus \kappa_i g) \oplus \kappa_i g = \Sigma_i l_i \oplus \kappa_i g. \tag{3.4.2}$$

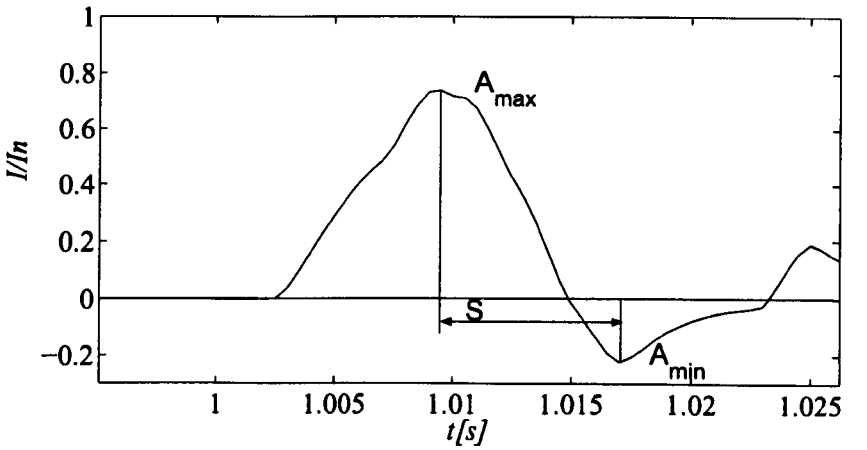

Figure 3.7: A typical inrush current waveform

The morphological representation is translation invariant and, in the continuous setting, scale invariant and rotation invariant (if the structuring function is rotation invariant). The quality of the reconstruction depends on the shape of the structuring function and its size. The details that are smaller than the structuring function are lost and the reconstructed function is a smoothed version of the original.

Consider a typical cycle of the inrush current, as illustrated in Figure 3.7, where this 50 Hz current signal I is normalised as I/In. It is clear that the asymmetries of the waveform exhibit in both amplitude and duration of the positive and negative segments. If the signal is decomposed to have the peak around $A_{\max}$ and the valley around $A_{\min}$ separated from other components, both with a flat base of given length, then the difference in the amplitude of $A_{\max}$ and $A_{\min}$, as well as the interval between them, can be quantified and compared with those in the internal fault current and normal power system operation conditions.

Compared with the inrush current, the waveform of internal fault current, as shown in Figure 3.8, is a regular periodic signal with an exponentially decaying

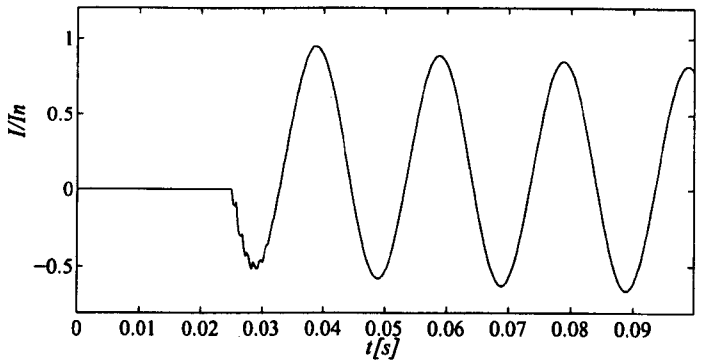

(a) Internal fault current waveform

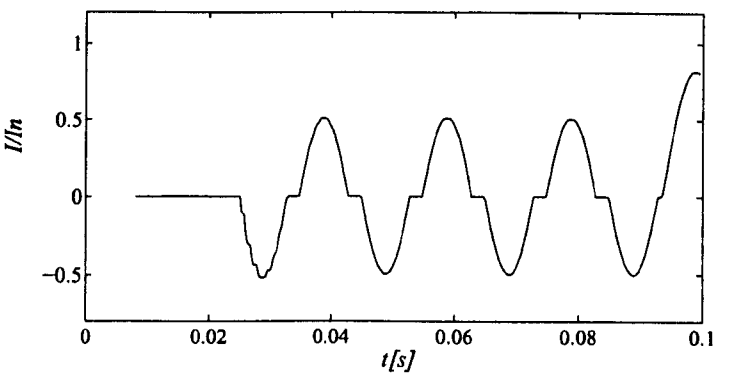

(b) Partial reconstruction with $\kappa = 0.08$

Figure 3.8: Internal fault current and its reconstruction

DC offset. If the effect of DC offset is removed, the waveform becomes a normal sinusoid. When the same decomposition as mentioned above is applied, the extracted peaks and valleys should have similar amplitudes, with intervals approximately equal to half of the power system cycle.

To perform such a decomposition for extracting the peaks and valleys of the transformer current signals, the morphological signal decomposition scheme is applied as illustrated in Figure 3.9.

The input current waveform is first transformed to obtain two signals f and f', defined as

$$\begin{aligned} f &= I + i_0 \\ f' &= -I + i_0, \end{aligned} \tag{3.4.3}$$

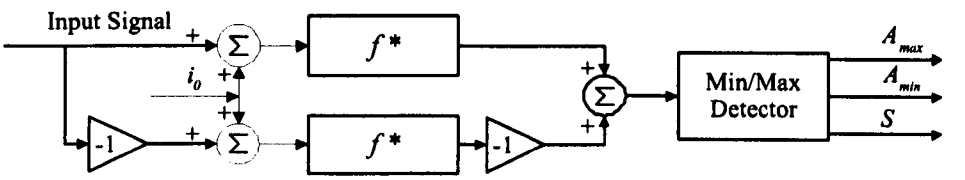

Figure 3.9: Block diagram of the proposed method

where i_0 is a pre-determined constant. i_0 is necessary since the morphological decomposition requires that the input signal f satisfies $[f \ominus kg](t) \geq 0$ [56]. The value of i_0 is not important as long as it results in both f and f' being positive. Since the current signal contains both peaks and valleys, due to the erosion operation in the decomposition procedure can only extract the peaks of a signal, the inverted input signal, f' is decomposed separately and then inverted again to obtain the valleys of the signal.

The structuring function g used for decomposition is a simple zero-valued flat line with 0.02 second length, with its origin at the center. However, the maximal number of iterations of decomposition, κ, does not need to be large enough to obtain a full reconstruction of the original signal, as long as it can extract the peaks of the waveform for measurement. In our study, we choose 0.08 seconds as the final structuring function; the reason will be discussed in following section. Therefore, there are three iterations of the morphological transform, with structuring function length at 0.02, 0.06 and 0.08 respectively.

3.4.2 Classification and decision

When a signal is decomposed to the given level, simple criteria can be employed to quantify the asymmetry in the signal, as follows:

$$\begin{aligned} \delta_I &= \frac{|A_{\max} - |A_{\min}||}{A_{\max} + |A_{\min}|} \times 100\% \\ \delta_t &= \frac{|S - 0.01|}{0.01} \times 100\%. \end{aligned} \tag{3.4.4}$$

where δ_I represents the amplitude asymmetry between the extracted peaks and valleys, whereas δ_t is the peak-to-valley interval asymmetry normalised by half of the power system cycle, which is 0.01 second in the case of 50 Hz. The higher the δ_I and δ_t are, the stronger the asymmetry existing in the signal. Therefore, if both δ_I and δ_t exceed a predefined threshold, an inrush current can be identified. Based on our practical experiment, we use 10% and 20% as the threshold for δ_I and δ_t, respectively.

3.5 Results

The proposed algorithm was tested with EMTDC/PSCAD [58] (an electromagnetic transients simulation software for electrical power systems, information on http://www.ee.umanitoba.ca/~hvdc) simulated internal fault current shown in Figure 3.8, as well as inrush signals, as shown in Figure 3.10 and Figure 3.11. The inrush signals, both with their second harmonic contents less than 10% and the effect of CT saturation, were measured on-site from a single type of transformer and provided by ALSTOM. As illustrated in the partially reconstructed waveforms, only the peaks and valleys of the original signal with 0.008 second intervals exist in the output signal, in which the singularities of the inrush current are clearly enhanced; where as shown in Figure 3.8(b), the partially reconstructed fault current of Figure 3.8(a) remains fairly symmetrical.

Figures 3.12 and 3.13 present a cycle by cycle evaluation of the waveform asymmetries, δ_I and δ_t respectively, for the partially reconstructed signals. It is clear that in the first cycle, both δ_I and δ_t of the fault current are far below the 10% threshold, whereas for the inrush currents, they are mostly well above 20% and may be as high as 73%.

One may notice that in certain cycles, e.g., the δ_I of inrush 2, at the third cycle (Table 3.1), is only 4.19%. However, since the identification of inrush

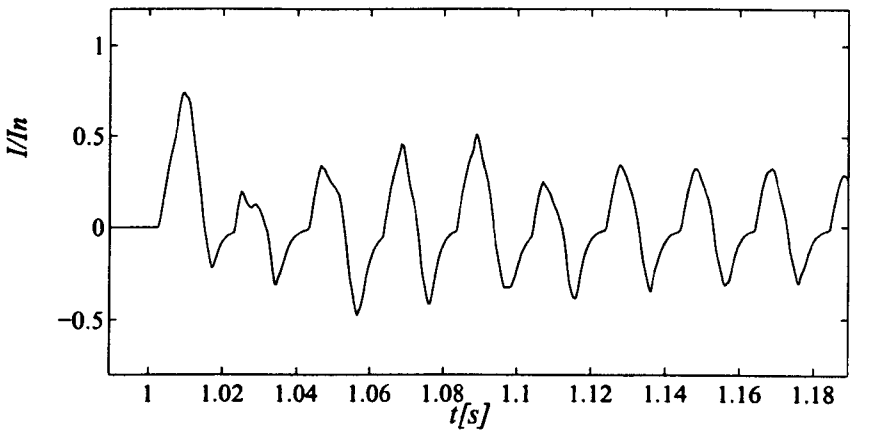

(a) Inrush signal 1

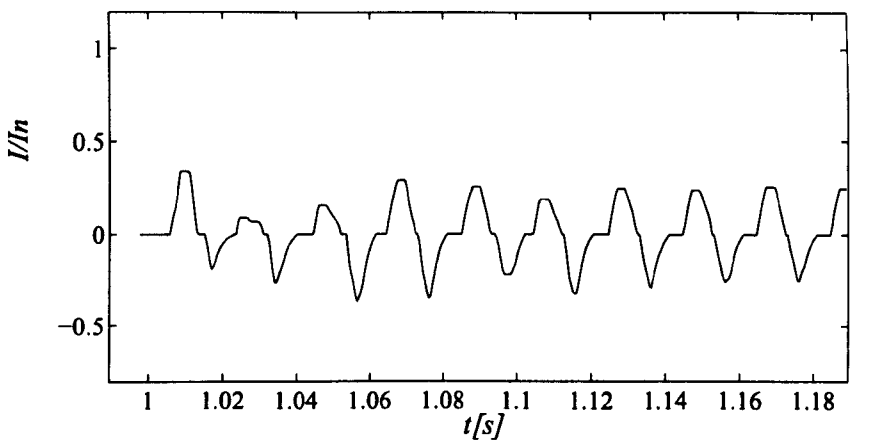

(b) Partial reconstruction with $\kappa = 0.08$

Figure 3.10: Inrush signal 1 and its reconstruction

current is solely by means of the asymmetry exhibited in the first cycle, such values should not cause any problem.

The maximal length of the structuring function is important in applying morphological signal decomposition, as it determines the length of the base for the extracted peaks and valleys, as well as their amplitudes. An optimal length of the maximal structuring function should allow the asymmetry in the amplitude to be accurately extracted. A reasonable length should also be chosen to avoid excessive calculation, since the longer the structuring function,

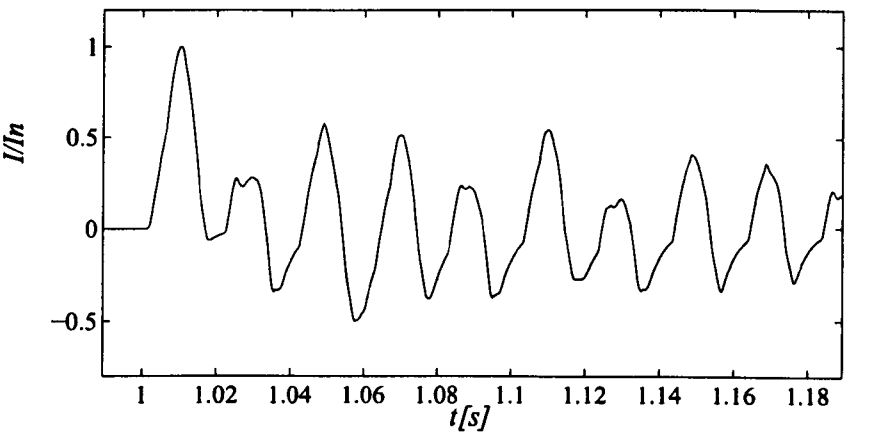

(a) Inrush signal 2

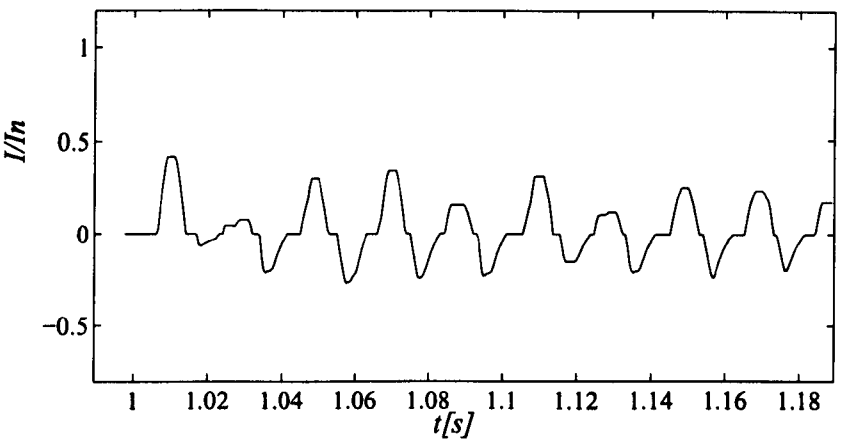

(b) Its partial reconstruction with $\kappa = 0.08$

Figure 3.11: Inrush signal 2 and its reconstruction

the more computational effort is required for to the morphology operation.

The variation of δ_I with respect to the maximal structuring function in the first cycle is given in Figure 3.14, for both inrush and internal fault waveform. It indicates that before point A at 0.008 second, the difference between inrush and fault current is not evident enough; whereas after A, the prolonged structuring function will lead to extra computation load. Therefore 0.008 second is chosen as the maximal length of structuring function in our study.

For off-line simulations where computation time is not critical, the structur-

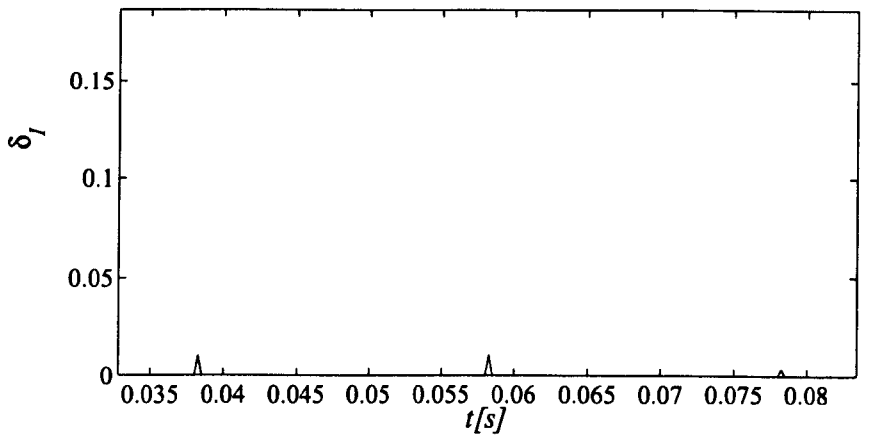

(a) Internal fault

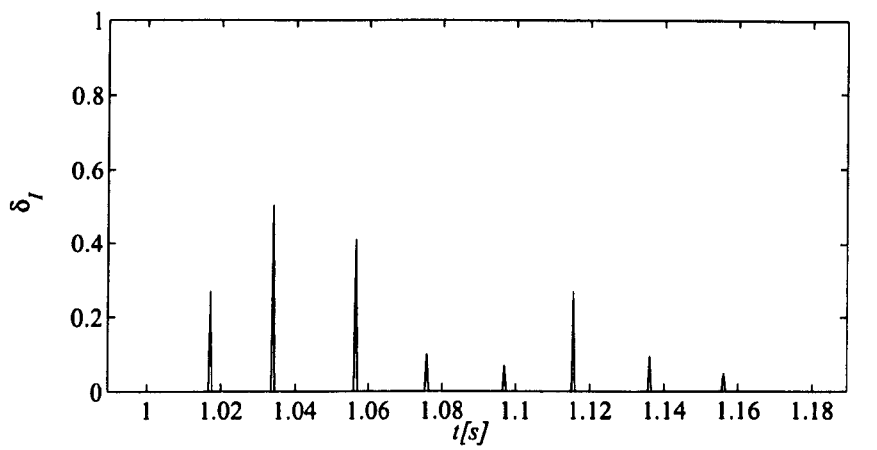

(b) Inrush 1

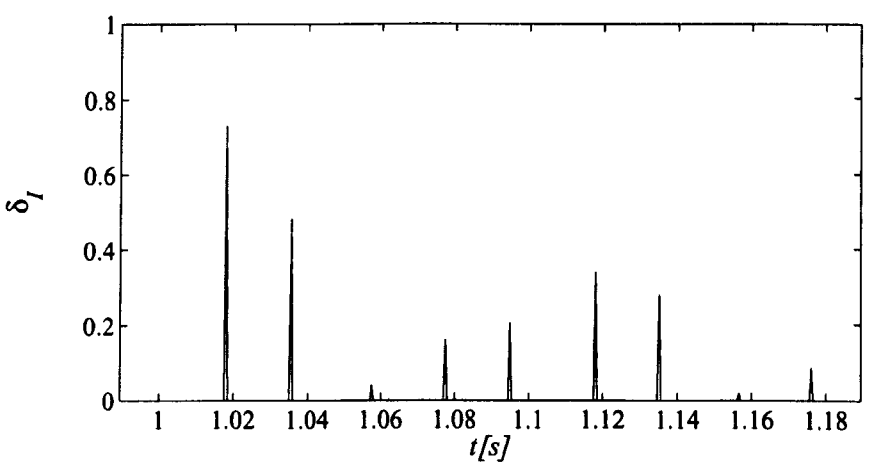

(c) Inrush 2

Figure 3.12: The asymmetries on peak and valley amplitudes

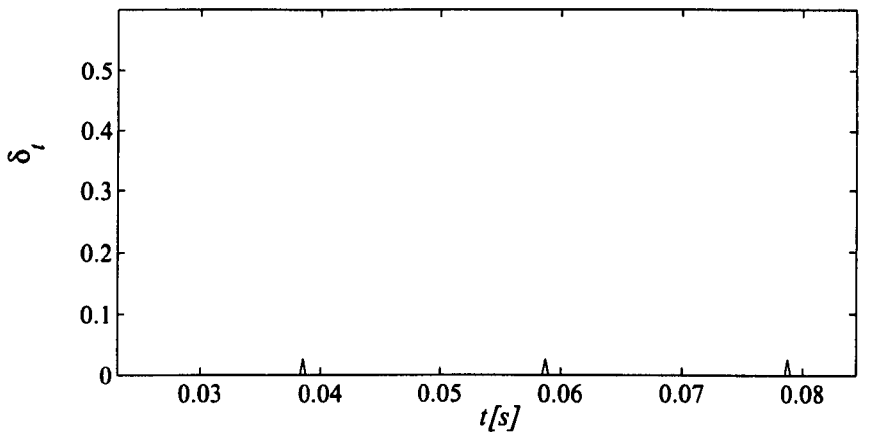

(a) Internal fault

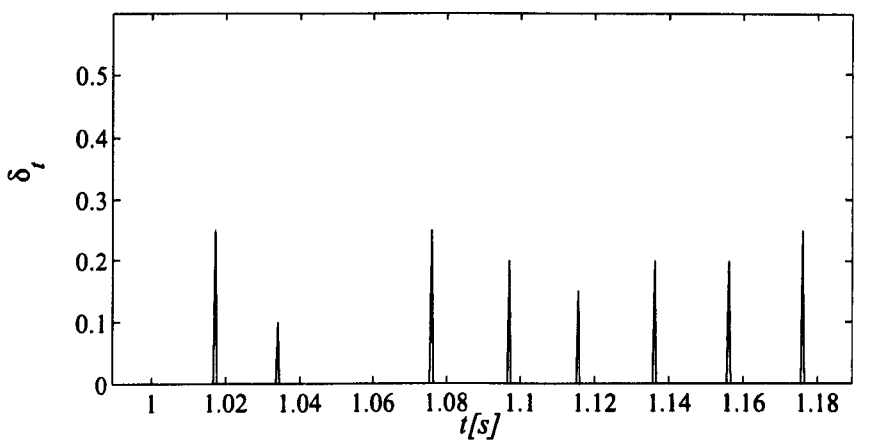

(b) Inrush 1

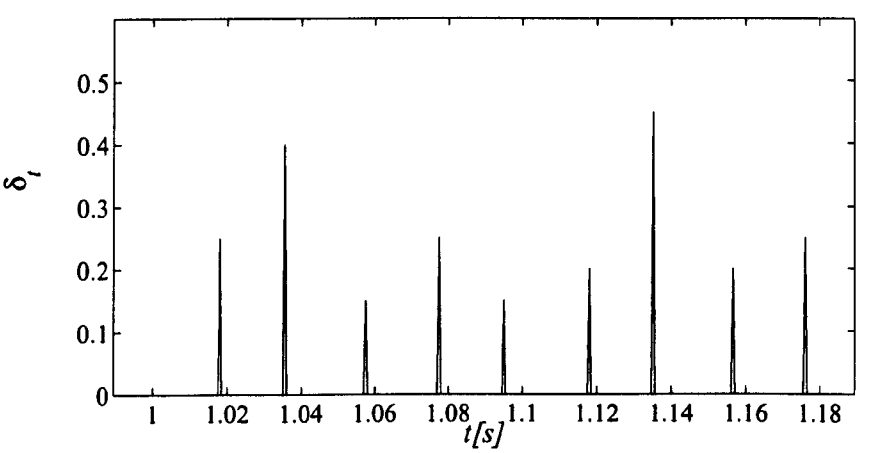

(c) Inrush 2

Figure 3.13: The asymmetries on peak-to-valley intervals

Signal	1st period	2nd period	3rd period
inrush1	27%	50.51%	41.1%
inrush2	73.11%	48.38%	4.19%
internal fault	4.05%	0.2%	1.17%

Table 3.1: δ_I of the inrush and internal fault currents

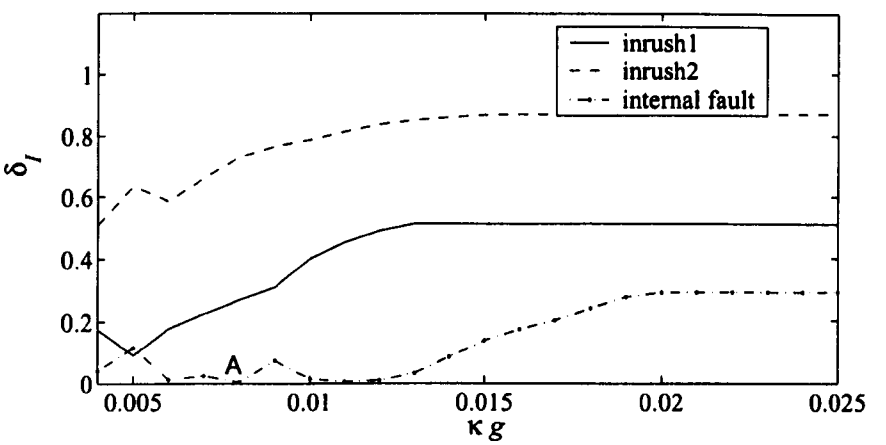

Figure 3.14: Variation of the detected amplitude asymmetry δ_I with respect to the maximal structuring function

ing element may be adjusted, or may be adaptive, to achieve better accuracy at the expense of computing time. For a real-time implementation, in the case where an inrush occurs at zero phase and the 0.008 second length structuring function is applied, the identification requires one power system cycle for obtaining the $A_{\max}$ and $A_{\min}$, plus 0.008 second for the dilation and erosion involved in the opening for decomposition.

3.6 Discussion and conclusions

This chapter describes an original work on applying morphological filtering techniques to the design of power transformer protective relays, to identify inrush current taking into consideration the CT saturation condition. The tech-

nique is fundamentally different from conventional methods, as it decomposes the signal based on time domain features instead of in the frequency domain. Since it works directly upon the geometric characteristics of the input, there is no need for abstract transform techniques such as Fourier, Laplace, and Hilbert transforms, nor is there a requirement for transform-world concepts such as frequency, convolution, effective bandwidth and ripple.

As shown by the results obtained, the advantages of the proposed scheme are:

1. reliable identification of inrush in cases when inrush current contains less than 10% of the second harmonic component (inrush current detection is based on time domain recognition);

2. reliable operation of protection when the CTs are saturated;

3. reduced computational complexity by using nonlinear morphological operations with only addition/subtraction and finding local maxima/minima in calculation [27];

4. the classification scheme is an simple yet effective way of assigning an observed signal to a particular group;

5. it provides flexibility in the choice of structuring function which can be adjusted by modifying its shape.

Research on improving the performance of the harmonics constraint based inrush current identification algorithms continues. However, most of these studies are either based on the transformer equivalent circuit model or require some transformer data, and this may become susceptible to parameter variations. By morphologically decomposing the signal and partially reconstructing it with a certain level of details, the asymmetrical features of the inrush waveform are exposed, whereas other irrelevant components are attenuated. With a

set of simple criteria, a much better signal characterisation and a more reliable discrimination can be obtained.

Further improvement on the identification performance may be achieved by optimising the structuring function to obtain a more effective decomposition.

Chapter 4

Morphological approach for neonatal ECG signal processing

This chapter presents a set of morphological algorithms for normalising, processing and analysing the neonatal electrocardiogram (ECG). Following an introduction to the terms used to describe the ECG, a morphological filtering scheme that adapts to subject specific information is described, to estimate and remove the baseline wander from the signal, while introducing less distortion to the ECG waveform. The normalised signals are then processed to obtain a set of ECG measurements. The studies are conducted on ECGs with simulated interference and also on actual noisy records. The results obtained are investigated.

4.1 Introduction

This study aims to develop and evaluate a new MM based ECG processing and analysis system for use on neonates.

Monitoring the neonatal ECG is a well recognised and routine part of the care of babies on a neonatal intensive care unit. Rolfe [59] states that the

most convenient way of monitoring heart rate in the newborn is from an ECG signal. Therefore unless a specific cardiac defect is suspected, the majority of these ECGs are used primarily for this purpose. They are not routinely used to achieve a detailed analysis of the ECG parameters as these measurements would usually involve the time consuming act of manual interpretation and measurement. This may also be influenced by the fact that existing technology has not yet been able to accurately monitor ECG parameters in neonates due to the rapid heart rate of both pre-term and term babies. There is also a distinct lack of existing commercial equipment for the automatic processing and measurement of the neonatal ECG waveform.

It is possible that there may be more information held within the neonatal ECG. This regards impairment of the blood and oxygen supply to the baby, during the perinatal period. In particular a link has been proposed between the shape of the neonatal ECG during the hours after birth, and myocardial ischaemia as a result of hypoxia-ischaemia during the intrapartum period. Barberi *et al.* [60] support this hypothesis, stating that in asphyxiated neonates, hypoxia is often responsible for myocardial ischaemia. Their study found a clear relationship between the clinical pattern of asphyxiated newborn infants and alterations of ECG. The theory being that asphyxia severe enough to injure the brain could also affect the myocardium. Mallard *et al.* [15] used a sheep model to highlight that ECG abnormalities in asphyxiated fetal sheep are proportional to the development of the severity of brain injury sustained. If this were found to be the case in humans it would allow for the identification of babies at high risk of the complications of asphyxia using ECG measurements, thus allowing intervention at an early stage, which may improve overall outcome. Evaluation of this hypothesis necessitates the accurate analysis of the neonatal ECG, highlighting the need for a more sophisticated technology.

The need for new technology is evident within the literature on the general subject of neonatal ECG monitoring. As far back as 1977 Emery called for

refinement in our tools of assessing neonatal ECGs [61]. Although one may assume that in the decades since, some advancement in technology has occurred, it seems this is still not sufficient. Zupancic *et al.* [62] highlight this need for advancement, concluding that the cost effectiveness of neonatal ECG screening for prolongation of the QT interval, depends heavily on the efficacy of monitoring. The practice of manual interpretation of the neonatal ECG has been repeatedly criticised. Martin *et al.* [63] condemns the use of visual interpretation of neonatal ECG, suggesting there is a much greater degree of variability than with computer based measurements.

There are other areas of neonatology where the role of the ECG, in both diagnostic and surveillance terms, has been controversially highlighted. Schwartz *et al.* [64] studied the prolongation of the QT interval with relation to the sudden infant death syndrome (SIDS). Their research concludes that prolongation of the QT interval in the first week of life is strongly associated with SIDS. Therefore neonatal ECG screening may permit early identification of infants at high risk, allowing the potential for implementation of preventative measures. However both the results and methodology of this study have been criticised. Martin *et al.* [63] highlight the fact that 800 of the surviving infants in this study had elevated ST segment. They conclude that the data from Schwartz *et al.* suggests that ECG analysis for the QT interval does not meet the criteria for an acceptable screening test. Perhaps a more automated and reliable technique, such as the aforementioned morphological approach, could hold the key to creating a more consistent and useful way of screening for markers of SIDS, and moreover, to discover the usefulness and reliability of neonatal ECGs.

4.2 The ECG signal

The parts of the heart normally beat in an orderly sequence. Contraction of the atria (*atrial systole*) is followed by contraction of the ventricles (*ventricular*

systole), and during *diastole* all four chambers are relaxed. The heartbeat originates in a specialised cardiac conduction system (see Figure 4.1) and spreads via this system to all parts of the myocardium. The structures that make up the conduction system are the *sinoatrial node* (SA node), the *internodal pathways*, the *atrioventricular node* (AV node), the *bundle of His* and its branches, and the *Purkinje system* [65].

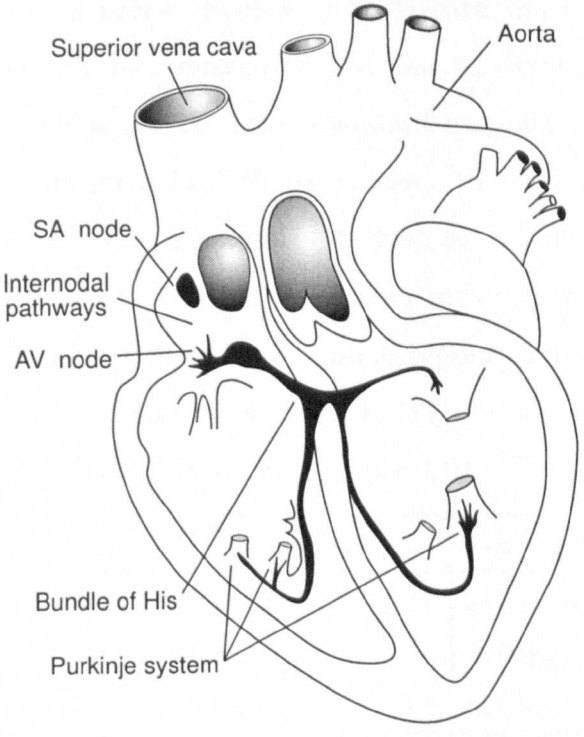

Figure 4.1: Human cardiac conduction system

The SA node is the normal cardiac pacemaker; its rate of discharge determines the rate at which the heart beats. Impulses generated from the SA node pass through the atrial pathways to the AV node, through this node to the bundle of His, and through the branches of the bundle of His via the Purkinje system to the ventricular muscle.

Because the body fluids are good conductors, fluctuations in potential that represent the algebraic sum of the action potentials of myocardial fibres can be

recorded extracelluary. The record of these potential fluctuations during the cardiac cycles is the ECG.

The ECG may be recorded by using an *active* (or *exploring*) electrode with an indifferent electrode at zero potential (*unipolar* recording), or by using two active electrodes (*bipolar* recording). In a volume conductor, the sum of the potentials at the points of an equilateral triangle with a current source in the centre is zero at all times. Such a triangle with the heart at its centre (*Einthoven's triangle*) can be approximated by placing electrodes on both arms and on the left leg. These are the three standard unipolar limb leads used in electrocardiography, designated by VR (right arm), VL (left arm), and VF (left foot). If they are connected to a common terminal, an indifferent electrode that stays near zero potential is obtained. The other universally accepted form of ECG is 12-lead ECG, in addition to the three bipolar limb leads (Lead I, II and III), there are six unipolar chest leads V_1–V_6 and three augmented limb leads aVR, aVL, aVF (see Table 4.1 and Figure 4.2).

Name	Type of load	Active electrode	Neutral electrode
Lead I		Right arm	Left arm
Lead II	Bipolar limb	Right arm	Left leg
Lead III		Left arm	left leg
aVR		Right arm	Left arm and leg
aVL	Unipolar limb	Left arm	Left leg and right arm
aVF		Left leg	Right and left arm
V1 to V6	Unipolar chest	One of six chest sites	Both arms and left leg

Table 4.1: Arrangements of standard leads for ECG signal acquisition

Figure 4.3 illustrates a cycle of a human adult's ECG. By convention, an upward deflection is written when the active electrode becomes positive relative to the indifferent electrode, and a downward deflection is written when the active electrode becomes negative. Major waves and intervals in ECG duration

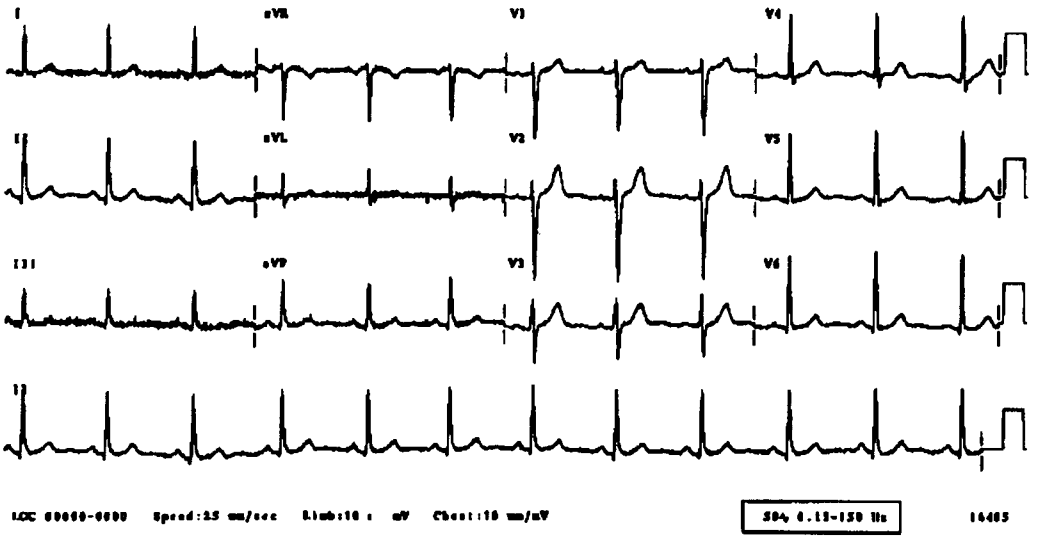

Figure 4.2: A standard 12-lead ECG record

and their corresponding activities in the heart are given as follows:

P Wave: Produced by atrial depolarisation. Increased voltage or duration of the P wave is usually diagnostic. Absence of P waves occurs in atrial stanstill, during periods of sinus arrest, and in SA block. In atrial flutter and fibrillation, the P waves are replaced by other oscillations called F and f waves, respectively.

PR interval: Atrial depolatisation and conduction through AV node, ranged from 0.12 to 0.20 seconds for adults.

QRS interval: Ventricular depolarisation and atrial repolarisation. The initial downward and upward deflection after P wave are called Q and R waves respectively. S wave usually represents the terminal part of ventricular activation. The normal duration of QRS is about 0.08 to 0.10 seconds.

ST interval: Comprises ST segment and T wave and stands for ventricular repolarisation, normally from 0.32 to 0.43 seconds.

U wave: An inconstant finding, believed to be due to slow repolarisation of the papillary muscles. It is not included in our study.

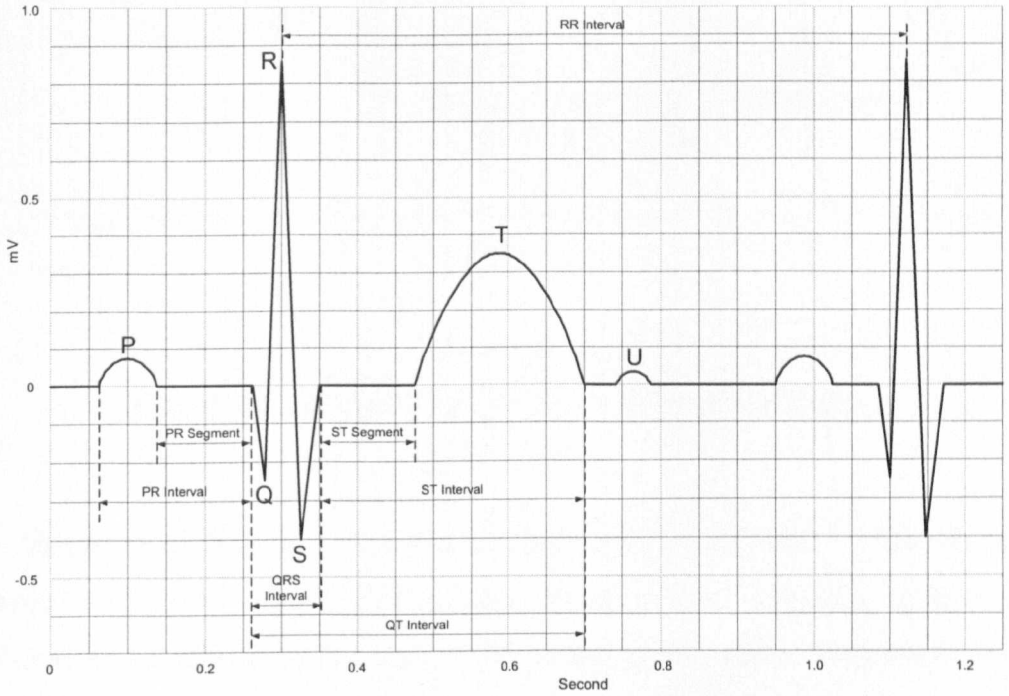

Figure 4.3: Waves of the ECG

4.3 MM for integrated QRS detection and background normalisation

4.3.1 Background

ECG signals are frequently plagued by impulsive noise due to, e.g., muscle activities and power line interference [17]. Moreover, background normalisation is required to correct the baseline wander caused by respiration and motion of the subject [66] (see Figure 4.4. In the following discussions, 'artefact' is used to designate the impulsive noise and baseline wander).

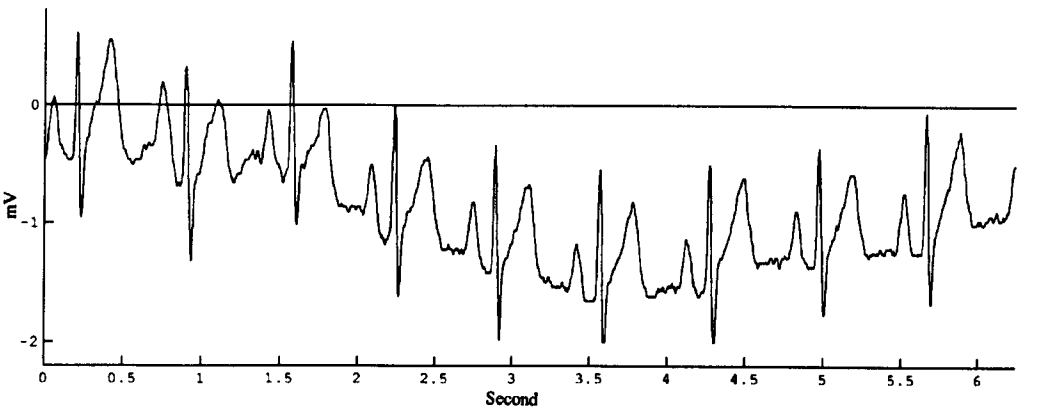

Figure 4.4: A typical ECG signal with baseline wander

Impulsive noise suppression and background normalisation are usually performed as the first step of ECG signal processing. It is important to limit the distortion introduced by the artefact suppression algorithms, before such tasks as QRS detection or temporal alignment can be carried out. We also note that issues such as preserving the subtle notches and slurs in individual waves are significant for clinical diagnostic use.

The most common approach to high frequency noise suppression is by low-pass filtering, which is ineffective for reducing impulsive noise [16]. Since baseline wander is assumed to have a relatively low frequency, baseline correction is normally achieved by high-pass filtering the ECG data [67]. However, as it requires the subject to be in a resting condition, it is neither suitable for the neonates which exhibit movements from time to time, nor for an accurate quantitative measurement of the ST segment. Alternatives to the conventional linear filtering techniques, particularly when dealing with impulsive noise, are nonlinear operators such as median filter [68] or other ranked ordering methods [69].

Morphological filtering techniques, as described in previous chapters, are

known for their robust performance in preserving the shape of a signal while suppressing the noise. Morphological approaches for artefact suppression and QRS detection have been proposed [1] [18], where the authors suggest the following advantages that the MM based method may possess:

- It is formal, based on mathematically well defined operators. Hence, any *ad hoc* schemes that are usually employed in signal analysis are avoided.
- It is simple and intuitively appealing. The operators employed are simple, conceivable and efficient that can be used in signal analysis problems.
- It is robust since it is applied without any prerequisites concerning the ECG signals. The only assumption made concerns the abruptness of the peaks that constitute the QRS complexes, which coincides with our perception of these complexes.
- It is computationally efficient since it employs only opening and closing which are implemented as addition/subtraction and minimum/maximum operations. Moreover, VLSI architectures for their implementation have also been proposed [70], which make morphological processing extremely fast. Consequently, real-time implementation of the proposed QRS detection scheme is feasible, which is important in ambulatory patient monitoring.

4.3.2 Proposed algorithm

As already mentioned, artefact suppression is the first step in ECG signal processing. However, when performing morphological baseline correction before QRS detection, there is significant distortion to the waveform around the QRS complex. This condition is mostly due to the distinct shape of the QRS complex. When considering the fore-and-aft P and T waves, the waveforms

between them are similar to the P and T waves, in both duration and amplitude (an illustration will be given in the following sections). In the baseline produced by morphological filtering, as proposed in [1], there exists a frequency component that matches the heart rate, as shown in Figure 4.5.

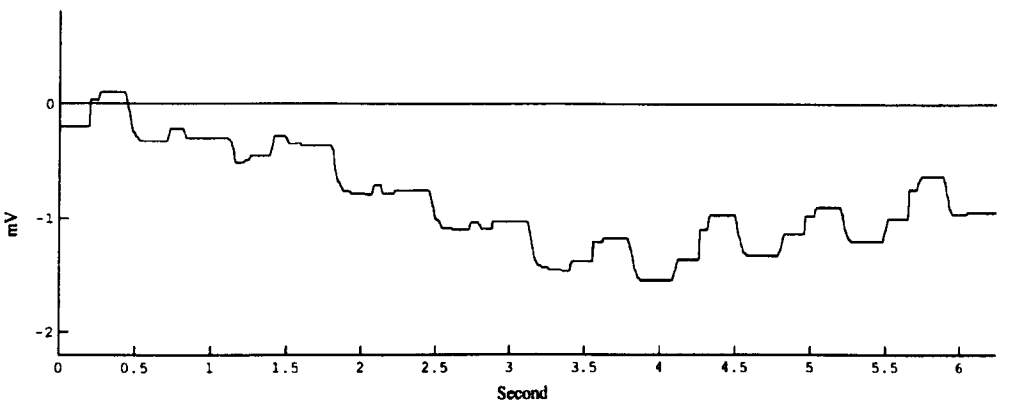

Figure 4.5: The baseline produced by filtering Figure 4.4 with [1]

The importance of finding the baseline correctly is obvious, since any subsequent measurement is subject to the accuracy of the baseline normalisation algorithm. Intuitively, if the QRS complexes can be removed from the input signal before baseline correction, to obtain a residue consisting of mainly the P and T waves, a better result may be achieved by morphologically filtering this residue. In the following sections a new algorithm based on an inverted sequence of processing is described, in which the QRS complexes are first extracted from the mains interference filtered (Section 5.2) ECG signal, and then the baseline wander is detected and corrected on this QRS removed signal. Various waves and parameters can therefore be allocated and measured on the normalised signal, including the PR, QRS, QT intervals, P and T amplitudes, ST segment elevation, etc.

As illustrated in Figure 4.6, the removal of baseline wander from neonatal

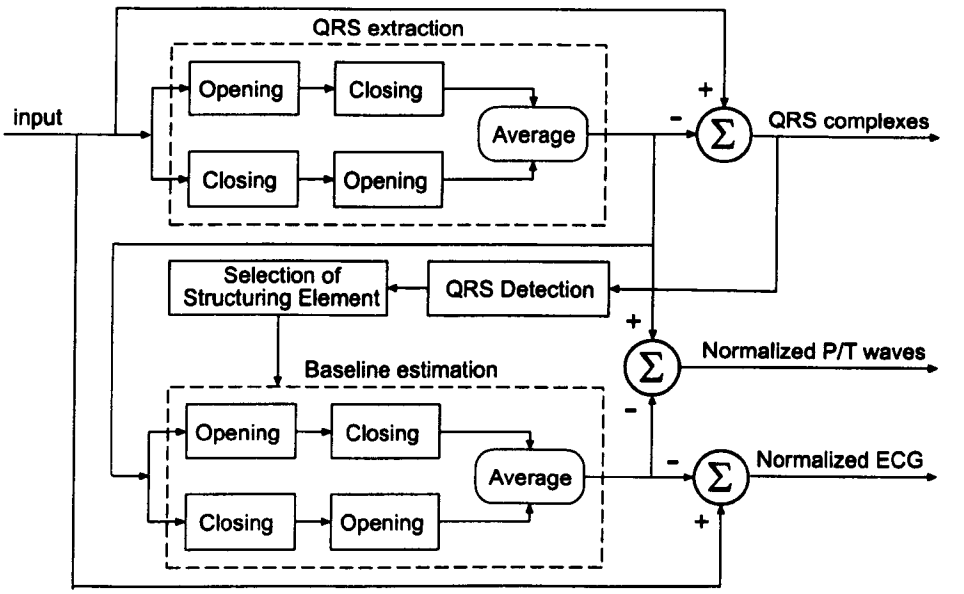

Figure 4.6: Block diagram of the proposed background normalisation algorithm

ECG is divided into two stages of morphological operations with an identical structure, namely QRS extraction and baseline estimation. The output of the second stage, which is the evaluated baseline wander, is then subtracted from the corrupted input signal to obtain a normalised ECG.

The morphological operations involved in each stage can be found in literature [1] [18]. However, the proposed algorithm is distinguished by its sequence and application of these operations, as well as the selection of corresponding SE. In addition to impulsive noise suppression, the first stage is also for the purpose of QRS complex detection and extraction. Due to its shape and amplitude, the QRS complex is the most dominant event among various ECG components. The morphological operation opening-closing and closing-opening, which have the effect of removing sharp peaks and valleys, can therefore be applied to extract the QRS complex and noise components as follows (Section 2.3)

$$y_1 = (x \circ s_1 \bullet s_1 + x \bullet s_1 \circ s_1)/2, \tag{4.3.1}$$

where x is the input ECG signal with artefact, s_1 the SE and y_1 the output signal with QRS complexes removed. To use the more effective implementation of real-time morphological operators [27] [71], a symmetrical SE with all its values equal to zero and the origin at the centre is taken. For removal of the QRS complexes, the length of the SE should be less than the length of the P or T waves, but longer than the QRS interval and noise components to be extracted. If the duration of the QRS complex is T seconds and the sampling frequency is f_s Hz, then the corresponding interval will be $T \times f_s$ samples. Therefore the length of the SE should be longer than $T \times f_s$. The QRS duration in normal newborns ranges from 25 ms to 69 ms (5% centile and 95% centile, respectively) [72]. Therefore 69 ms is chosen as the length of the symmetrical SE, with the origin at its centre. The remaining components in y_1 are mainly the P, T waves and baseline fluctuation, as shown in Figure 4.7(b), where Figure 4.7(a) is a simulated ECG signal for illustration. Subtracting y_1 from x, a signal containing mostly QRS complexes and impulsive noise can be obtained (Figure 4.7(c)). With this signal, the R waves are then allocated by finding local maxima in the waveform that exceed a predefined threshold value, and the RR intervals can be derived accordingly. In our studies, a satisfactory result can be achieved when using 50% of the global maximum as the threshold. Alternatively, a more complicated adaptive method can be employed to further improve the performance [18].

The morphological operations in the second stage are used to remove the P and T waves from y_1. Therefore, compared to s_1, the length of the SE s_2 should be increased to exceed the length of these waves. When the same operations as in (4.3.1) are applied to y_1, with s_2 as the SE, the remaining ECG components will be removed and only the fluctuation of baseline is left, as follows

$$y_2 = (y_1 \circ s_2 \bullet s_2 + y_1 \bullet s_2 \circ s_2)/2 \tag{4.3.2}$$

Since in most circumstances the duration of the T wave is longer than that

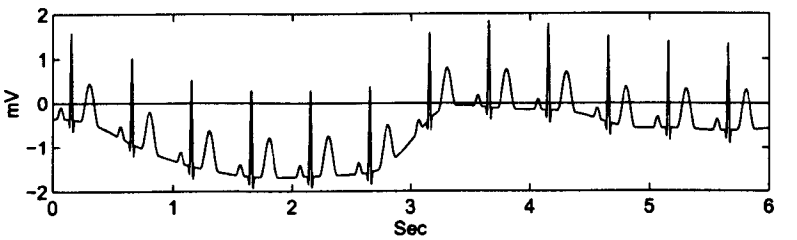

(a) the input signal

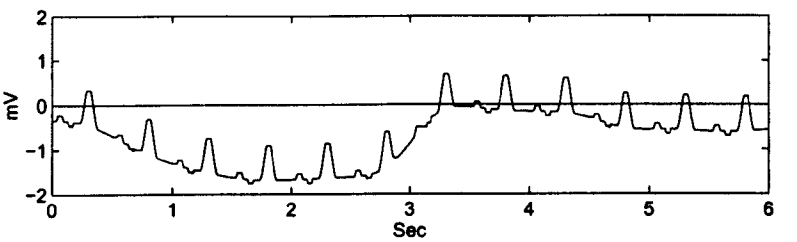

(b) result of QRS complex extraction

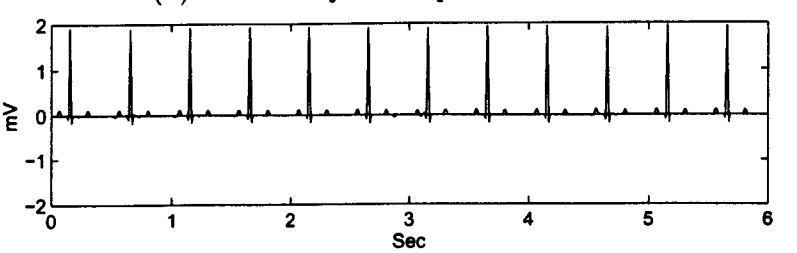

(c) extracted QRS complexes ((a) - (b))

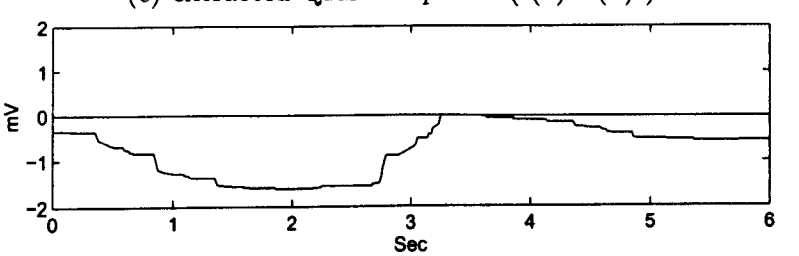

(d) the estimated baseline

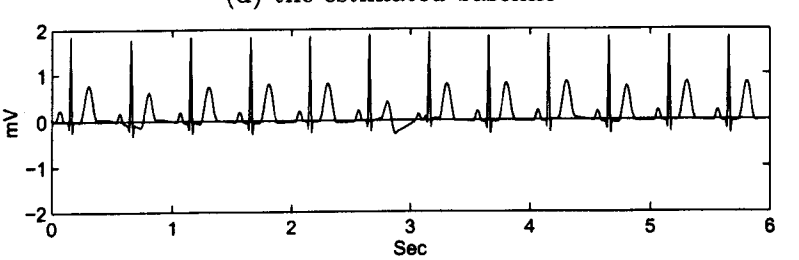

(e) the normalised signal: Output I ((a) - (d))

Figure 4.7: An example of the processing sequence

of the P wave, it can be chosen to determine the length of s_2, while the values of s_2 remain zeros as in s_1, with its origin at the centre. However, during the newborn period the T waves may be altered by many factors that lead to ST segment elevation or depression [72]. In this case the beginning of the T wave may not be isoelectric. A distorted baseline will be produced if the beginnings of such T waves are mistakenly considered as isoelectric.

Since the baseline between the P and Q waves still remains at zero potential when variations occur in the ST segment, the QT interval is more preferable for the determination of the length of s_2. Although the duration of the QT interval is sensitive to heart rate variation [73] and can not be considered as a constant, it can be corrected by applying Bazett's formula [74] as follows

$$\mathrm{QTc} = \frac{\mathrm{QT}}{\sqrt{\mathrm{RR}}}, \tag{4.3.3}$$

where QTc is the corrected QT interval, QT and RR represent QT interval and RR interval, respectively.

QTc remains remarkably constant throughout childhood, with a certain amount of variation during the neonatal period. The QTc of normal infants varies from a mean of 397($\pm$18) ms aged four days, to a mean of 409($\pm$ 15) ms at two months [75]. If QTc is considered as a constant, then the QT interval can be described as

$$\mathrm{QT} = \mathrm{QTc} \times \sqrt{\mathrm{RR}} \tag{4.3.4}$$

Therefore the QT interval, i.e., the length of s_2 is solely determined by the RR interval, which is already available after the first stage of QRS extraction. The estimated baseline of Figure 4.7(a) is shown in Figure 4.7(d), with the QTc of 389 ms measured before processing; Figure 4.7(e) is the corrected ECG signal, i.e., $x - y_2$ (denoted as Output I).

After the baseline wander has been removed from the input, the impulsive noise components may still exist in the normalised output signal. If a noise-filtered signal is required, the extracted QRS signal (Figure 4.7(c)) with

another signal that contains corrected P, T waves (subtracting Figure 4.7(d) from Figure 4.7(b)), can be considered as an artefact filtered and decomposed output signal (denoted as Output II). Since the ECG components existing in the QRS signal are mainly the QRS complexes, information related to different ECG components can be allocated accordingly in the decomposed output: either QRS complexes from the QRS signal, or the P, T waves from the corrected P, T signal.

4.4 P, T waves detection

4.4.1 ST intervals and T waves detection

In certain cases the P wave can be near to the T wave. It would therefore be a mistake to try to identify the T waves without considering the location of the P waves, as is attempted by the current T wave detection algorithms in literature (e.g., [76] and [77]). A more reliable approach would be to detect the ST interval before identifying the T waves [78]. When later the P waves are detected, T waves can therefore be separated. The T waves are positive or sometimes negative or even bipolar. They may occur immediately after the QRS offset. The T waves are usually flat compared to the duration of QRS and they have higher amplitude than the P waves. The following descriptions illustrate the proposed algorithm for ST interval detection.

1. Locate the interval between current QRS offset and the next QRS onset (*search area*), within which to perform following analysis.

2. Apply open-closing (*opcl*) to the search area. Experimental results suggest that a flat SE of size 9 ms satisfies the demands.

3. Calculate the first derivative of the filtered data in the search area (denoted as *deriv1*).

4. Find the maximum absolute value among 1/8 of the full interval range of *opcl* and remember its location. Find out the real sign of the relevant maximum. Denote it as *max18*.

5. The T waves can never closely follow the QRS complexes, therefore possible fluctuations and/or ST segment elevations should be ignored. Then search rightward from the location of *max18*, with consideration of *deriv1* and the amplitude of *opcl*, to reach a flat area.

6. Find the maximum of the absolute value of *opcl*, from the above point to half of the full range of search area, as it is the most possible range to locate the T wave. Denote the location of this maximum as *max12*.

7. Move leftward and rightward from the location of *max12* to find the onset and offset of the T wave with the similar technique as for finding QRS onset and offset, with consideration that T waves are always more flat than the QRS complexes.

8. Evaluate the detected onset and offset. They should be in appropriate ranges and distances from the offset of the corresponding QRS complexes. If they are beyond the acceptable ranges, then reject them.

4.4.2 Residue

For difficult rhythms (where atrial waves are on top of ST intervals, or they spread all over the ECG with no fixed temporal relation to the QRS), it is better to form one single template of the ST for all the complexes which look alike. Moreover if the ST interval is close to isoelectric, then it is not possible to find any atrial waves buried inside T waves or in the ST segments. Reddy *et al.* apply ST median and QRS interpolation to obtain a residue [79]. The following algorithm is adapted from this method.

1. The correlation among all detected ST intervals is evaluated first. If the correlation exceeds a threshold, the corresponding segments are categorised as the same template, otherwise a new template is built. The value for the threshold should be decided very careful. The higher the level of the threshold, the more the number of templates, and vice versa.

2. After categorising the ST intervals into different groups, the median of each group is found.

3. Each ST interval is subtracted from the median of its group.

4. All QRS complexes are substituted by interpolation of the values of their onsets and offsets. They are not replaced by zero values in order to avoid the abrupt discontinuities in the subtracted waveform.

Applying the above algorithm will produce a residue mostly carrying information about the P waves.

4.4.3 P wave detection

Reddy et al. apply a nine-point central differentiator upon the residue as follows [80]

$$\begin{aligned} y(n) &= \frac{-x(n-4)}{256} - \frac{3x(n-3)}{32} - \frac{x(n-2)}{2} - x(n-1) \\ &+ \frac{x(n+4)}{256} + \frac{3x(n+3)}{32} + \frac{x(n+2)}{2} + x(n+1) \end{aligned} \tag{4.4.1}$$

Then they investigate the second difference, $z(n)$, of the signal x, computed as:

$$z(n) = y(n) - y(n-1) \tag{4.4.2}$$

A composite function f is then constructed by rectifying and adding the first and second difference as:

$$f(n) = |y(n)| + |z(n)| \tag{4.4.3}$$

We, instead, use morphological filtering as follows:

1. Compute the absolute value of the open-close of the residual signal. Considering the width of the P wave, a flat SE of size 9 ms is adequate. Take the mean value of these signals, denoted as $opcl_2(n)$, for following analysis.

2. Calculate the first derivative of the above signal.

3. Investigate all the intervals between the offset of the current QRS and the onset of the next one.

4. Find the local maxima inside the intervals.

5. Find the onset and offset around each maximum with similar techniques to those previously applied for T wave detection.

6. Evaluate the validity of the candidate points as the onsets and offsets of different P waves by investigating their amplitudes and widths.

Figure 4.8 illustrates the processing flow of detecting the P and T waves on an ECG data file.

4.5 Results and analysis

4.5.1 Method of analysis

To investigate the performance of the proposed algorithm in a controlled manner, the experiments were conducted on two types of test data: one was synthetic signals obtained by adding artificial interference to actual noise-free ECG components with well-known properties; the other was real signals with both baseline wander and noise components.

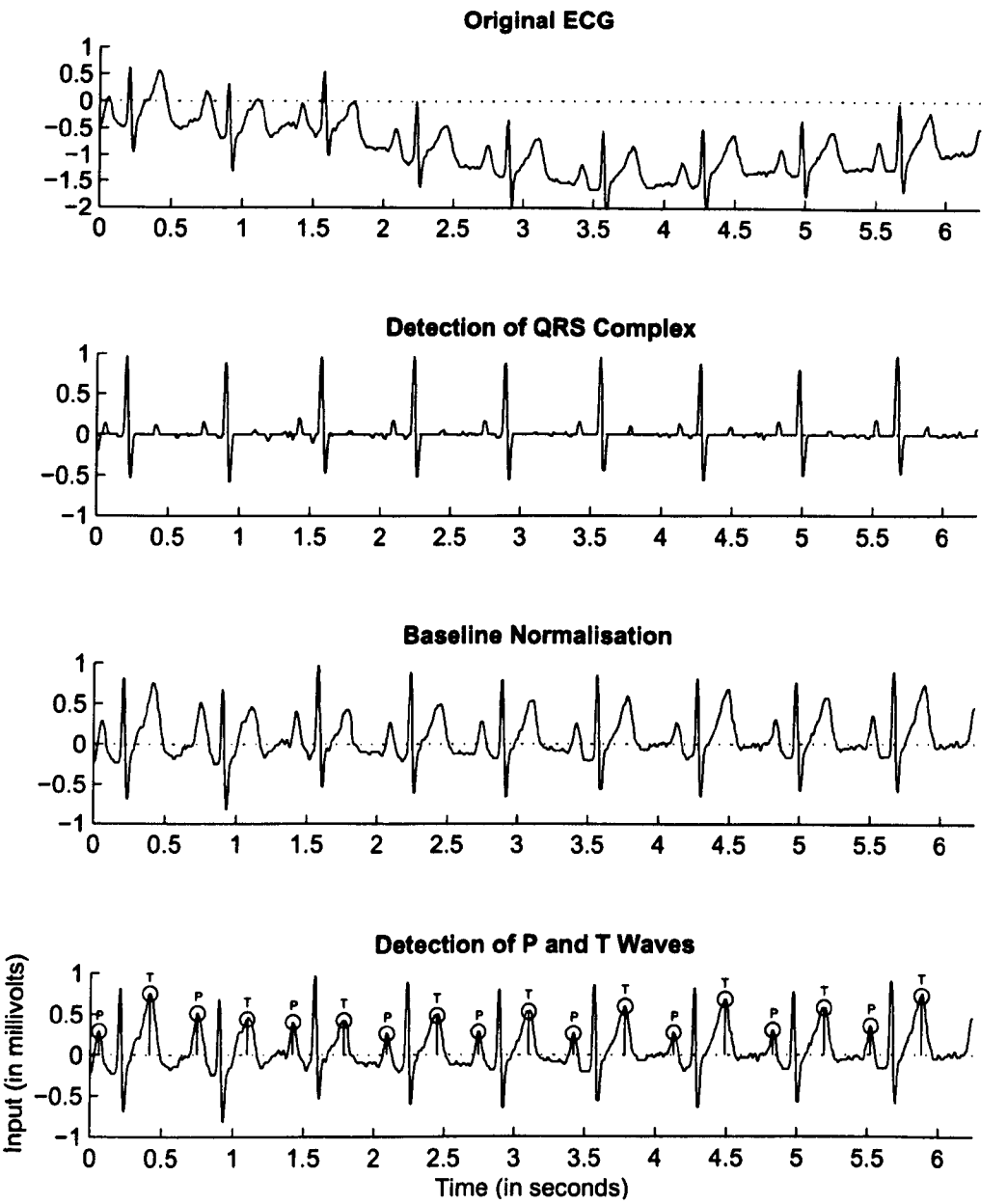

Figure 4.8: Detection of the P and T waves.

To evaluate the level of artefact in the simulated ECGs and the normalised output signals and also to quantify and compare the improvements in the results, the signal-to-noise-ratio (SNR) is used [81]. This is defined as

$$\text{SNR} = 10 \times \log_{10} \frac{S_\sigma}{N_\sigma}$$

where S and N are the noise-free ECG signal and the simulated artefact, respectively. For a given signal X, X_σ is defined as

$$X_\sigma = \sum_{l=0}^{L-1} (X(l) - \mu_X)^2$$

where μ_X, L are the mean and length of signal X, respectively.

The synthetic signal is constructed by first choosing a noise-free ECG beat. Then, after adjusting the interval that follows the T wave to be normally distributed, numbers of such beat are concatenated to construct an ECG epoch with predefined length. Finally, artificial noise components, as well as baseline wander, are added to this signal. Therefore by adjusting the degree of different disturbances that mimic various types of artefact, the improvements on the output signal can be evaluated and compared.

In the test signal, the ECG beat is selected at the heart rate of 130 bpm, the amplitudes of R, P and T waves are 1.6 mV, 0.15 mV and 0.55 mV respectively. The isoelectric interval after the T wave is adjusted to be normally distributed, with a mean of 30 ms and standard deviation of 10 ms. After concatenation of 15 such beats, an arbitrary portion with a length of 6 seconds is chosen to be the source of the test signal. To simulate baseline wander and other noise components, we firstly generate a signal $i(n)$, with ϵ mixture of Gaussian noise, described by the probability distribution

$$P_i(y) = (1-\epsilon)\Phi(\frac{y}{\sigma_1}) + \epsilon\Phi(\frac{y}{\sigma_2}),\ 0 < \epsilon < 1$$

where $\Phi(y)$ is a normal distribution function with zero mean and unit standard deviation. The parameters σ_1 and σ_2 determine the standard deviation of

the two elements: the low level background noise with probability of $(1 - \epsilon)$ and the high level impulsive noise corresponding to ϵ. The signal $i(n)$ is then passed through a low-pass and a high-pass fifth-order Butterworth filter respectively, with adjustable and 40 Hz of cut-off frequency respectively. The baseline wander is generated by adding the output of the low-pass filter to a step function at the 3rd second, with amplitude of 1 mV, to simulate an abrupt change of the baseline level. The signal of artificial disturbances is obtained by adding the output of the high-pass filter to the simulated baseline wander, and finally, it is multiplied by a gain factor corresponding to 0dB SNR and added to the noise-free ECG signal.

For real signals with baseline wander and noise components, due to the indeterminate nature of both the ECG components and the disturbances, the output signals are evaluated and compared by means of measuring the variance of major ECG parameters on the normalised signal. Although this is not as accurate and intuitive an indication of improvement as the SNR, for a stable and periodical ECG epoch, the rhythmic components should be fairly similar in each cardiac cycle. If the baseline wander has been successfully removed, only slight variance should occur on these measured parameters. This is quantified by using the coefficient of variation (CV) in percentage, defined as

$$\mathrm{CV} = \frac{100 \times \mathrm{SD}}{\mu_X}, \tag{4.5.1}$$

where the standard deviation (SD) is given as

$$\mathrm{SD} = \sqrt{\frac{X_\sigma}{(L-1)}}, \tag{4.5.2}$$

L is the number of beats in the test signal, with incomplete leading and trailing complex in the record discarded. X represents the parameter to be evaluated, including the amplitudes of R, P, T waves and ST segments, and the durations of PR, QT, QRS and RR intervals.

4.5.2 Result and discussion

The ECG signals from standard limb leads (Lead I, II and III, see Table 4.1) were acquired by an analogue bioamplifier BMA-200(CWE, Philadelphia) with an ISO-Z isolation head-stage (gain=10). The cut-off frequency of the built-in low-pass filter was adjusted to 1 kHz. To avoid any distortion introduced by the built-in high-pass analogue filter [67], the bioamplifier was configured to be DC coupling and the gain was set to 100, therefore an overall amplification of 1000 was obtained. To prevent the device from saturation, it was sometimes necessary to reduce the gain to 500 or even less. The output of the amplifier was digitised by a PCI-6023E data acquisition board (National Instruments, Austin), using 12-bit resolution with a sampling frequency of 1 kHz.

The results of applying the proposed method to a synthetic signal that contains noise components and baseline wander are shown in Figure 4.9 and Table 4.2, where the parameters for noise generation are $\epsilon = 0.1$, $\sigma_1 = 0.02$, $\sigma_2 = 0.2$. The frequency of baseline wander ranges from 0.5-4.0 Hz, which ranges from less than half of the heart rate to about twice of it. When the frequency of baseline wander is increased to above the heart rate, the SNR is rapidly degraded. In such case, the fundamental frequency of the ECG components overlaps with that of the baseline wander, i.e., they have similar duration. It then becomes difficult to separate these similar shapes using either morphological or linear-filtering approaches. However, due to the large amplitude and very short duration of the QRS complex, the SNR remains fairly high. Similar results for an ECG signal with only baseline wander have been also obtained, but with a higher degree of SNR due to the reduction of noise components, as illustrated by Figure 4.10 and Table 4.3.

In the results of processing two real signals, as shown in Figure 4.11, Figure 4.12 and Table 4.4, the P wave and ST segment amplitudes, and QRS intervals exhibit much higher levels of variation in both Output I and II. For

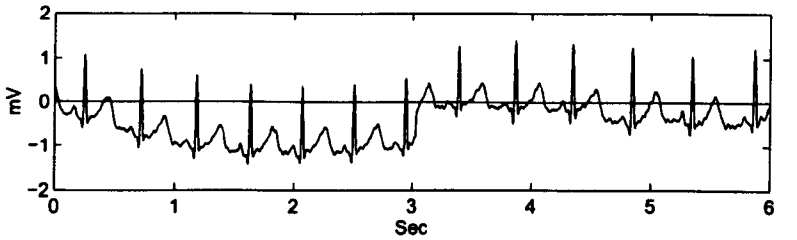

(a) the input signal

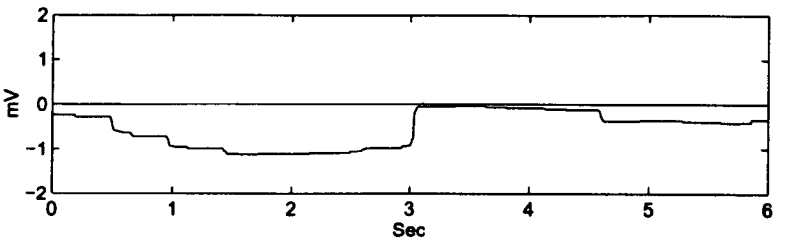

(b) the estimated baseline

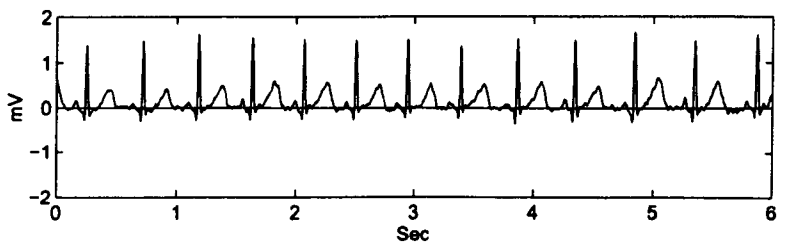

(c) normalised output signal (Output I)

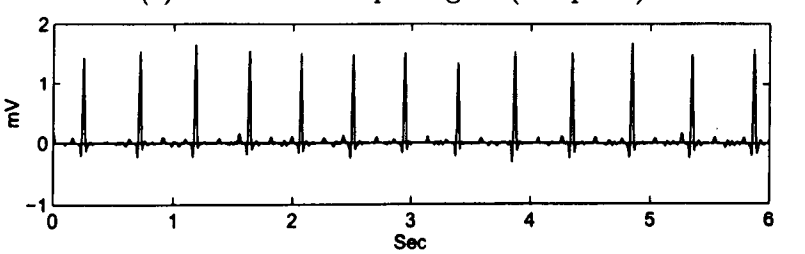

(d) the extracted QRS complex (QRS signal of Output II)

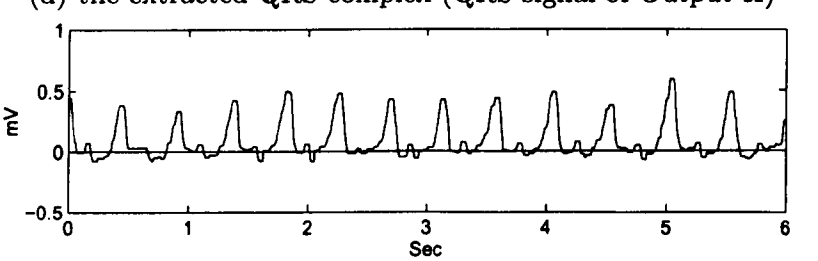

(e) normalised P, T waves (P, T signals of Output II)

Figure 4.9: Baseline correction on synthetic neonatal ECG with artificial disturbances. ($\epsilon = 0.1$, $\sigma_1 = 0.02$, $\sigma_2 = 0.2$, cut-off frequencies: 1 Hz, 40 Hz)

Cut-off frequency of baseline wander, Hz	Output I	Output II	
		QRS	P,T
0.5	17.7	31.3	14.3
1.0	17.4	32.1	12.7
1.5	16.5	30.2	11.8
2.0	15.9	29.1	9.21
2.5	13.1	27.7	8.54
3.0	10.2	26.3	7.33
3.5	7.81	26.4	6.21
4.0	6.93	24.6	6.54

Table 4.2: SNR improvements (dB) on synthetic neonatal ECGs with artificial noise components (below 40 Hz, $\epsilon = 0.1$, $\sigma_1 = 0.02$, $\sigma_2 = 0.20$) and different frequencies of baseline wander, the heart rate is 130 bpm

Cut-off frequency of baseline wander, Hz	Output I	Output II		MM2
		QRS	P,T	
0.5	21.6	35.2	21.2	16.2
1.0	21.7	32.4	17.8	15.4
1.5	20.1	33.2	16.0	13.7
2.0	18.1	30.6	16.3	11.9
2.5	17.4	31.9	12.1	10.1
3.0	14.7	28.8	10.3	9.23
3.5	11.5	25.2	9.73	7.34
4.0	10.6	25.0	9.42	6.63

Table 4.3: SNR improvements (dB) on synthetic neonatal ECGs with baseline wander, using different MM based algorithms. The heart rate is 130 bpm

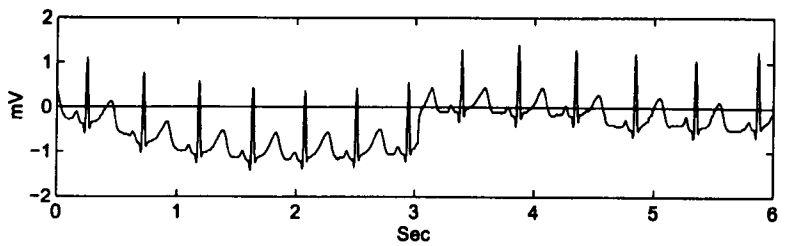

(a) the input signal

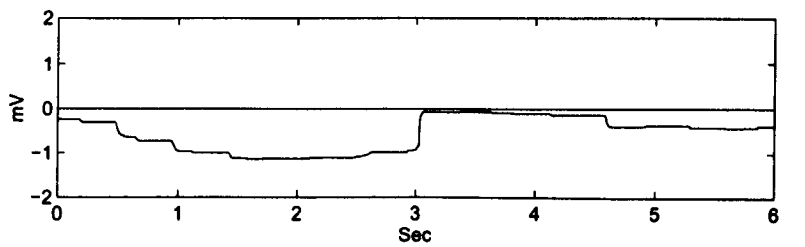

(b) the estimated baseline

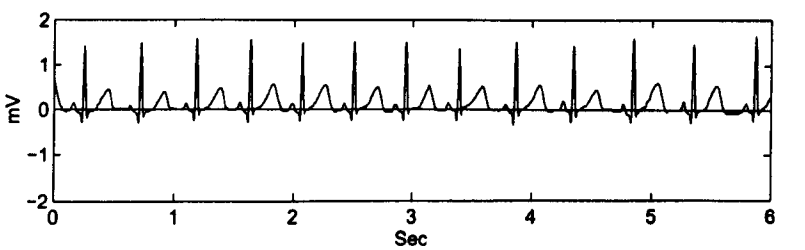

(c) the normalised output signal

Figure 4.10: Baseline correction on synthetic neonatal ECG with only baseline wander (cut-off frequencies: 1 Hz).

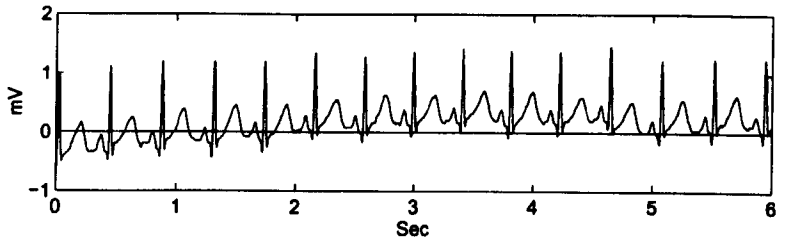

(a) the input signal

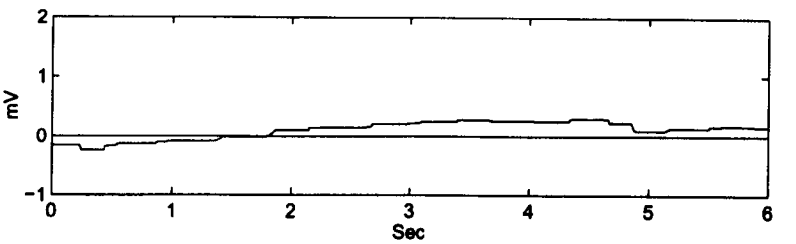

(b) the baseline

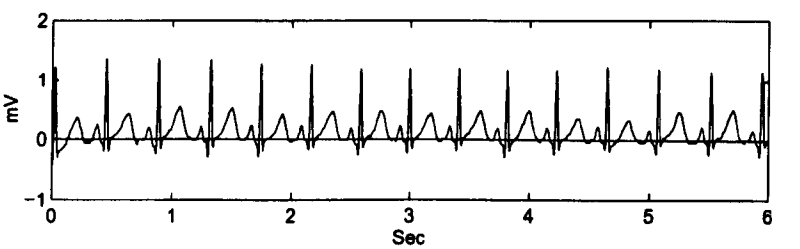

(c) Output I

Figure 4.11: Baseline correction on real neonatal ECG with a relative low level of noise.

Output II, since the morphological operations have the effect of removing the peaks of signal. These variations are much lower than in Output I.

The trend of measurements and the box and whisker plot, for major ECG parameters, are also given (Figures 4.13 and 4.14) for each individual subject. These are to facilitate the analysis of development and distribution of the ECG parameters, measured over periodical recordings.

To compare the proposed method with a morphological approach in literature [1] (denoted as MM2), the synthetic ECG in Figure 4.9 is processed by

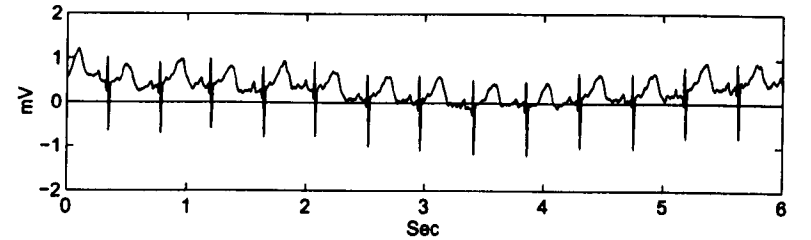

(a) the input signal

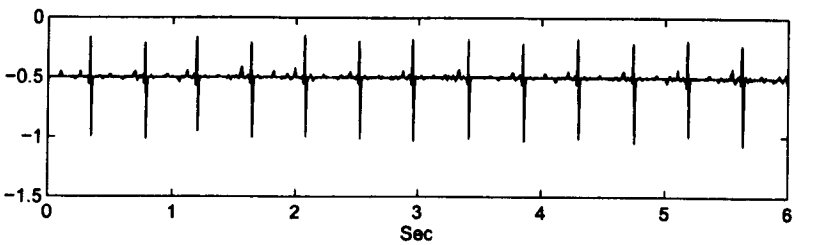

(b) QRS signal of Output II

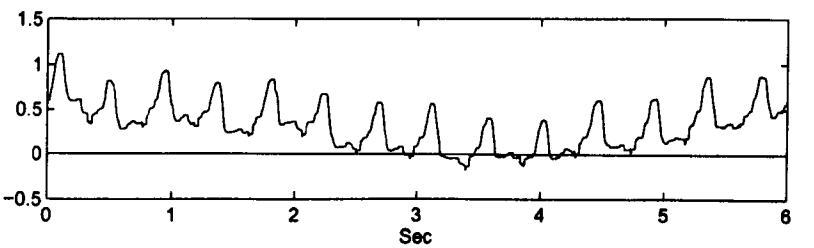

(c) P, T signal of Ouput II

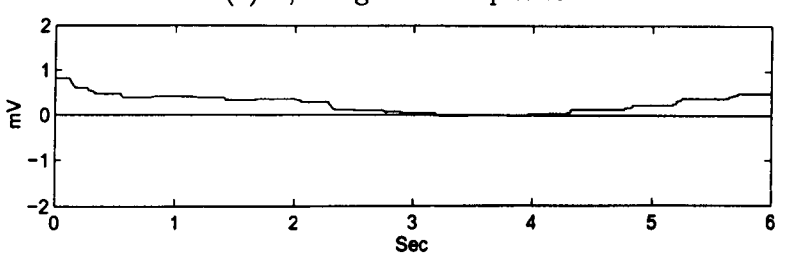

(d) The baseline

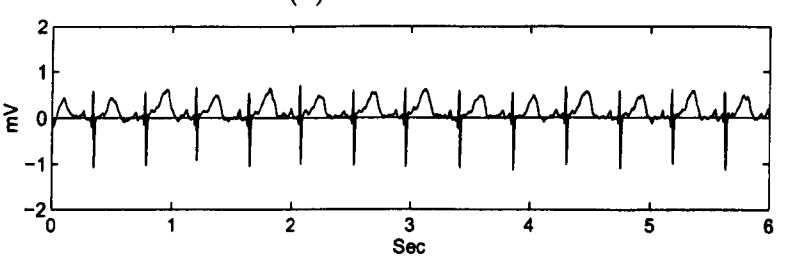

(e) Output I

Figure 4.12: Baseline correction on real neonatal ECG with a relative high level of noise.

Signal	Output	Amplitudes				Intervals			
		R	P	T	ST	RR	PR	QRS	QT
Figure 4.11	I	0.6	12	7.2	13	2.6	5.6	9.7	2.0
	II	0.6	7.2	4.1	8.2	2.6	5.6	9.7	2.0
Figure 4.12	I	4.4	37	12	32	2.0	2.4	1.1	1.3
	II	4.4	17	9.0	23	2.0	2.3	1.1	1.2

Table 4.4: The coefficient of variance (in percentage) of measurements on real neonatal ECGs

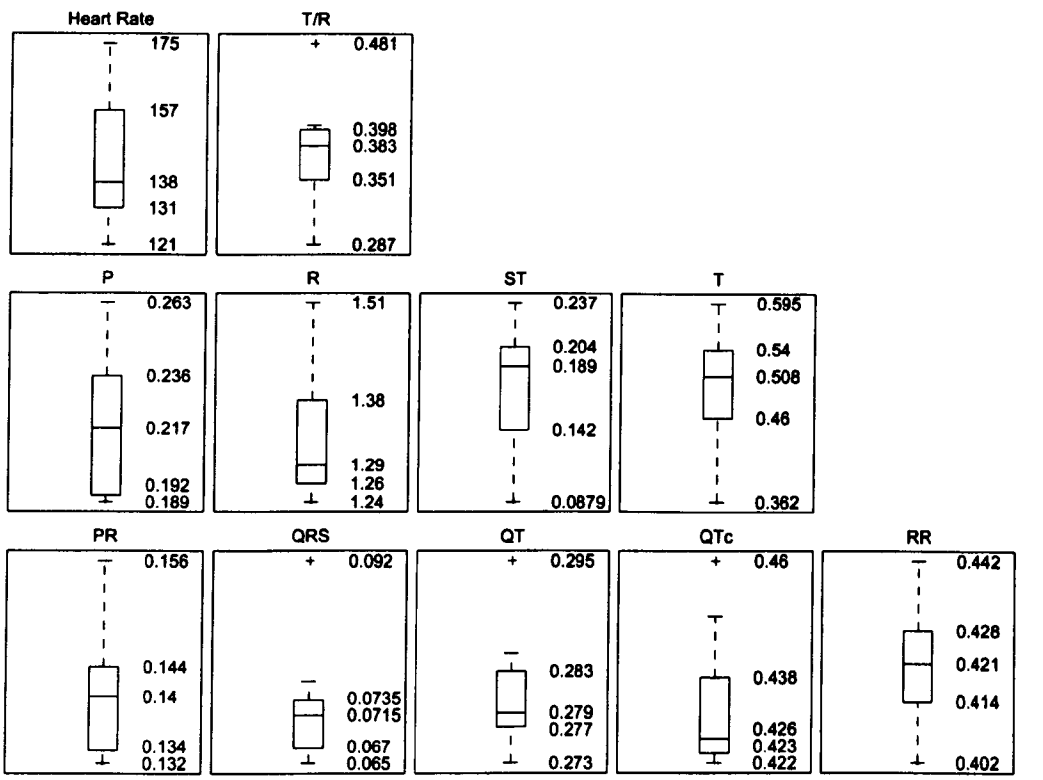

Figure 4.13: The box and whisker plot.

both algorithms. The reason for using this signal is that the original method will perform noise-filtering over the input signal; by choosing an ECG without noise components it is possible to limit the comparison to baseline correction performance only. The results given in Table 4.3 indicate a substantial im-

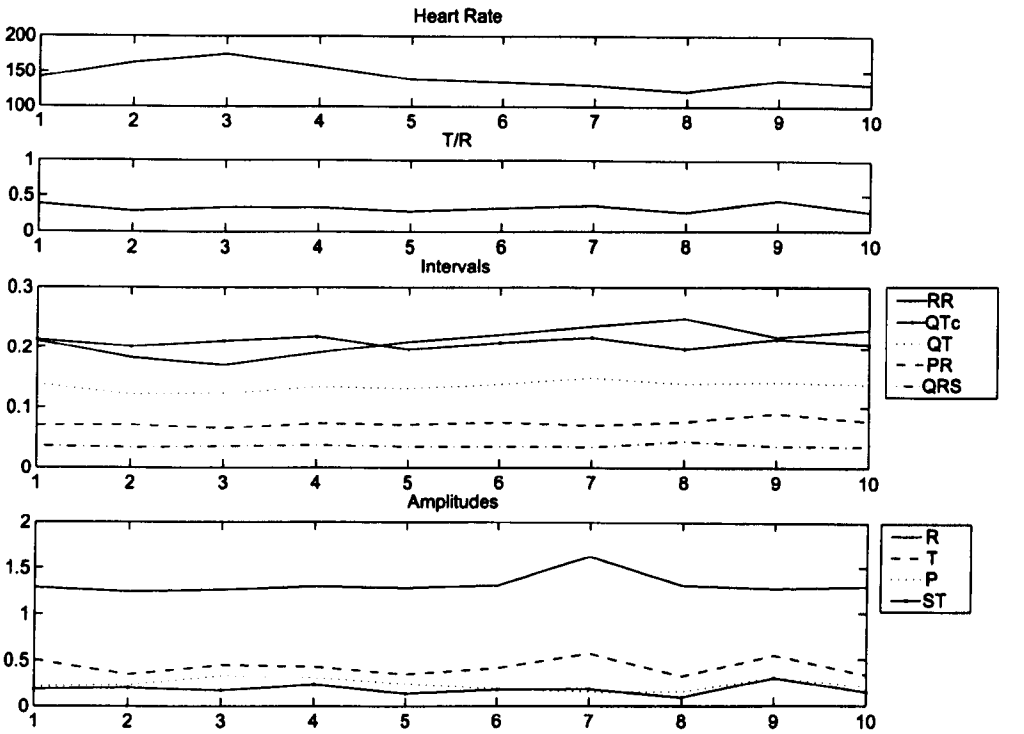

Figure 4.14: The trend of ECG measurements.

provement of the proposed method over MM2, in both Output I and II.

As illustrated by Figure 4.15, noting the result after opening and closing operations, the distortion introduced by MM2 can be related to two aspects. One is due to the 'gap' between P, R or Q, T waves, where the result of opening will be above the real baseline, if the lengths of these gaps are less than the length of SE. The other aspect is that if the length of SE is less than the T wave, there will be a residual of the T wave in the estimated baseline. Therefore, by elimination of the QRS complex and choosing a proper length of SE as aforementioned, such distortion can be avoided or greatly reduced.

An individual's QTc may differ considerably, which indicates that the square root approximation of Bazett's formula is a poor method under certain conditions [82]. For adults, better results can be obtained by using the cubic root method [83] [84]. In our study, for 16 newborns with QTc ranges from

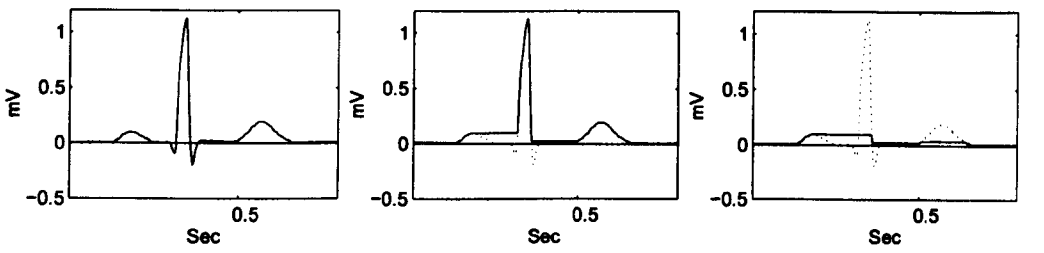

(a) Original method without QRS extraction

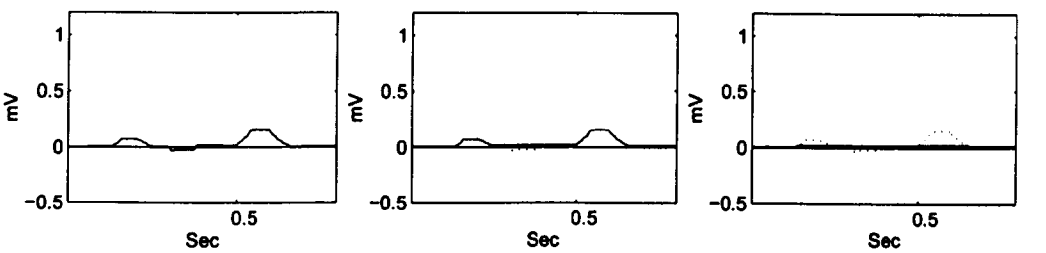

(b) Proposed method with QRS extraction and time-varying SE

Figure 4.15: Comparison of morphological approaches for baseline correction. From left to right: input signal; after opening; after closing

0.38 to 0.5, there are 10 cases with CV less than 5%, while the others are less than 15% (see Figure 4.16). The ease of use is the main reason for the use of Bazett's formula in determining the QT interval, i.e., the length of the SE for morphological operators in baseline correction. In the subjects studied the variation of QTc is acceptable, since compared to a constant length, the QTc adjusted SE introduces much less distortion to the baseline in ST segment and T wave. However, more comprehensive investigation is necessary to justify the application of Bazett's formula in processing the neonatal ECG.

The correction of baseline wander within ECG signals can be performed in different stages of processing: either before or after QRS detection and beat classification [85]. The advantage of obtaining the QRS complex before baseline correction is that the heart rate information can be incorporated into the later baseline correction algorithm. This heart rate dependent filtering technique was first proposed for off-line processing by means of linear phase FIR filters

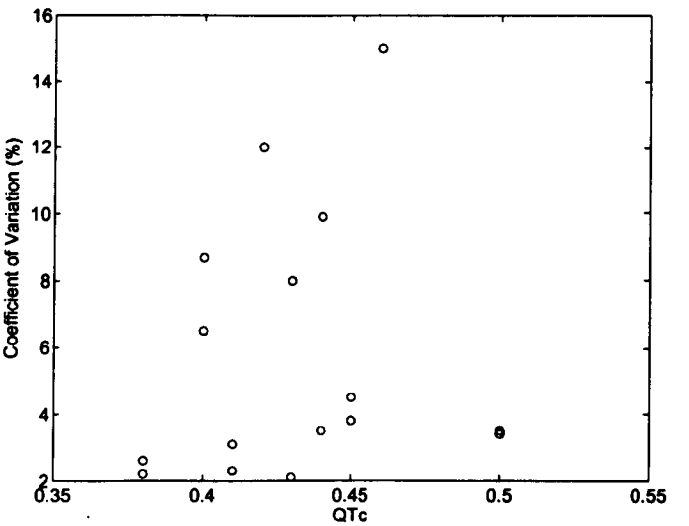

Figure 4.16: Coefficient of variation (%) of QTc from 16 newborns.

[86]. These authors concluded that when choosing a cut-off frequency below or equal to the heart rate, neither normal nor ectopic beats exhibit visible distortion. For these studies, there are six reasons for performing QRS complex extraction before baseline estimation, as follows:

1. the existence of QRS complex may affect the result of morphological operations on the PR and QT intervals, and it is therefore necessary to remove it for subsequent processing.

2. it is essential to have the information of the RR intervals before constructing the SE in the second stage of baseline estimation.

3. the QRS complex is the most distinguished event among various ECG waves, in both its amplitude and period. Therefore, compared to other measurements, such as the P and T waves, the output of QRS detection is the most reliable result that we can obtain without any specific assumption.

4. due to the small size of the SE involved in QRS extraction (about 1/10

of the SE length for baseline correction), the adjustment procedure using the heart rate is considerably faster than performing baseline correction prior to QRS detection.

5. moreover, because of the similarity in duration between the QRS complex and impulsive noise, it is possible to determine if there exists high level noise that needs additional filtering, within the first stage of processing.

6. in this application of off-line processing of ECG signals, the input signal has been limited to a fixed time duration. Therefore, any incomplete leading and trailing heart beats must be removed. By locating the QRS complex at the beginning, those unnecessary samples can be removed before any subsequent analysis.

Compared to high-pass filtering, which will suppress any signal with frequency lower than the designated cut-off frequency, morphological operators have very high performance in preserving shapes that contain various frequency components, as illustrated by the baseline in Figure 4.9(b), at the position of the step function. Also, in the normalised signal Figure 4.9(c), only minor distortion to the adjacent beats can be found. Another advantage that the proposed method possesses is that the obtained baseline will be on the zero line, i.e., measurement of various amplitudes can be performed directly on the output without considering the constant DC component, which may exist after high-pass filtering.

Compared with linear filtering techniques, the proposed method not only reduces the distortion to the ECG waveform, but is also efficient in terms of computational load. Generally, the operations of addition/subtraction and finding local maxima/minima, which are the fundamental operations that constitute morphological operators, are much faster than the multiplication/division involved in linear filtering. In the presented algorithm, by using a symmetrical SE with all the values zero, the amount of computation can be further reduced

since the only calculation involved is to find local maxima/minima. By choosing an appropriate hardware architecture, as proposed in previous studies [27] [71] [87], the real-time implementation of this algorithm is feasible for online monitoring.

4.6 Possible extension to fetal ECG

As discussed in this chapter, promising results have been obtained for reliable processing and analysis of neonatal ECGs. Moreover, the ECG, recorded from the maternal abdomen, can in principle be used to monitor the electrical activity of the fetal heart during the pregnancy period [88] [89].

The fetal ECG (FECG) signal is a measurement of the electrical activity from the heart muscles, i.e., myocardia. Intercardiac signals, generated by the action potentials of the different cardiac parts, pass through various body layers, and are finally picked up by electrodes on the skin surface of the mother. It is important to note that the signal has to penetrate through a complex system, experiencing various effects. In a pregnant woman, the ECG signals are commonly measured at two locations, the chest and the abdomen. By comparing the chest and abdominal composite signals, a method may be devised for extracting information about the FECG from the composite signal. This is highly desirable due to the noninvasive nature of the process. Moreover, as an extension to the current study on neonatal ECG, if it is successful, early intervention in the gestation period may be possible for fetuses at high risk of asphyxia.

However, the extracted FECG can vary between different techniques. The chest signals contain primarily the maternal ECG (MECG), with little if any contribution from the FECG. In contrast, the abdominal leads pick up a composite signal, consisting of the contributions from both the MECG and the FECG. The energy of the latter has been estimated as less than one quarter

of the total signal energy [88]. An ECG profile depends on the position where the signal is recorded. The different paths, from the heart to the various lead locations on the skin surface, can modify the intracardiac signal significantly [90].

Different methods have been proposed for the detection and (or) extraction of FECG. These can be classified based on the principle signal processing methodologies that are employed [91].

A method employing the auto-correlation and cross-correlation properties has been used in [92] and [93]. Linear weighted combination of signals from multiple leads, and adaptive filtering are discussed in [94] and [95], respectively. A scheme based on singular-value decomposition (SVD) is proposed in [96]. Also there are Wavelet based approaches [97] [98]. Exploiting various assumptions, these methods each use different signal features and (or) characteristics. The main drawbacks of these techniques are their underlying simplistic assumptions, namely the additive model for the composite signal and the assumed high correlation between the chest and the mother-component of abdominal signal profiles. In particular, the validity of the latter assumption can be questioned due to a variety of complex effects from the different body layers that each signal passes through.

In order to extract the fetal signal from the composite signal robustly, it is desirable to exploit those features of the signal that remain relatively invariant with respect to the lead position. The so-called *singular points*, which represent the shapes and positions of the high peaks of the ECG signals, may be employed for identifying the FECG. It is expected that the locations of the singular points remain relatively invariant, though the profile of the ECG signal may vary drastically with respect to the lead position. Therefore the locations instead of the amplitude, of the singular is more likely a better choice for determining the singular point. These have previously been employed in the detection of the ECG characteristic points [99]. The QRS and baseline

extraction technique discussed in the former sections can probably be slightly modified, with consideration of the signal feature, to facilitate the discrimination between the singular points of the maternal and fetal ECGs, both present in the composite abdominal signal.

4.7 Conclusions

In this chapter, a morphological method for processing and measuring the neonatal ECG signals is proposed, with improvements to an existing morphological approach for baseline correction. The possibility of extending this study to the fetal ECG is also discussed. Results with less distortion to the normalised signal were achieved by choosing a SE determined by the individual's QTc interval, which suggests that it is a successful extension of Bazett's formula to the neonatal ECG.

As the implementation of the proposed algorithms, a prototype of an integrated neonatal ECG analysis system is developed (Chapter 5). It aims to be a valuable tool for computerised analysis of the ECG signal, particularly to allow the user to examine the reliability of the results. Important features like ST segment measurement, trend analysis and cardiac vector calculation are also provided for adding diagnostic power to the routine examination and the standard interpretive features. This is the first step in developing a commercial system for monitoring the blood supply to the babies by means of analysis of the ECG signals. A set of experiments are also devised (Chapter 6) in order to determine the general variability of ECG measurements with the integrated system, as well as to validate the morphological techniques in neonatal ECG signal processing and analysis. These experiments were carried out by neonatalogists in a clinical environment, with promising results obtained which will facilitate further study of the neonatal ECG.

Chapter 5

System implementation and integration

In this chapter, the development and functionality of an integrated neonatal ECG analysis system are described, including the hardware design and integration, user interface, and various processing algorithms related to filtering and measuring ECG parameters.

This is the system used for the pilot trial described in Chapter 6.

5.1 Hardware

The neonatal ECG analysis system is based on a personal computer (IBM x86). It also contains a bio-amplifier BMA-200 (CWE, Philadelphia. see Appendix D for technical details), and an isolation head-stage ISO-Z (CWE) connected to the bio-amplifier for additional safety. The BMA-200 provides adjustable gain, high-pass and low-pass filters control, and an built-in audio monitor. The amplified signal from the BMA-200 is then acquired by the PC, with an 12-bit resolution analogue-to-digital convertor board PCI6025E (National Instruments, Austin), at a sampling rate of 1000 Hz.

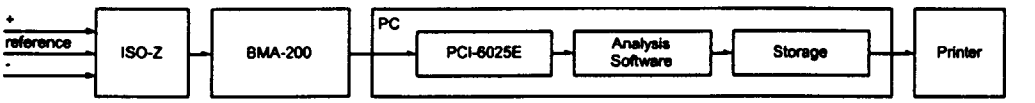

Figure 5.1: Hardware architecture of the system

The hardware architecture of the system is shown in Figure 5.1.

5.2 Software architecture

The software is written in the LabVIEW (National Instruments) graphical programming language, with basic morphological operators available in Matlab (Mathworks, Natick US). An illustration of the software architecture is shown in Figure 5.2, where the names of all the measurements obtained are printed in bold italic.

Two bipolar leads are applied to various positions on the neonate's limbs (Table 4.1) to obtain 3 ECG leads (I, II and III). The signal is amplified by the BMA-200, with built-in gains and offset controls, and high and low-pass filters. It is then acquired by the PCI6025E with a built-in anti-alias filter for analogue-to-digital conversion, and finally the digitised signal is passed to the analysis software. The software is built from following functional blocks:

- Mains filtering, it is a linear filter to remove the 50 Hz power line interference, as described in the following section.
- Baseline correction (Chapter 4), to detect and measure the waveform of the QRS complexes, and using these information to correct the baseline wander.
- Waves detection (Chapter 4), to detects the ST interval, the T and P waves, and to provide all the measurements from these waves. It also calculate the QRS axis as described in the following section.

- Subject and record information, to enter information related to the subject and the recording process.
- Information gathering, to provide facilities for producing graphical printouts and summary reports in spreadsheet format, hard disk archival, serial comparison of ECGs etc.
- Debug and configuration, to provide control of the program, e.g., its version, data file formats, etc. It also displays intermediate signals of morphologically processing the signal, as well as to configure the parameter to be used in the morphological filtering.

The applications of this system are described in detail in Chapter 6. The operation procedures and the format of the files produced by the system are given in Appendix D.

Calculation of other unipolar leads (Section 4.2) are also incorporated in the software. Given leads I and II are available, other leads (defined in Section 4.2) can be computed as follows

$$\begin{aligned} \text{III} &= \text{II} - \text{I}, \\ \text{aVR} &= -(\text{I} + \text{II})/2, \\ \text{aVL} &= \text{I} - \text{II}/2, \\ \text{aVF} &= -(\text{I} - 2\text{II})/2 \end{aligned}$$

However, because the BMA-200 is a single channel amplifier, the accuracy of the results obtained by using the above formulae is limited. If a multi-channel bio-amplifier become available, it could greatly expand the system's functionality, e.g., with a more accurate cardiac axis result or multi-lead synchronised analysis.

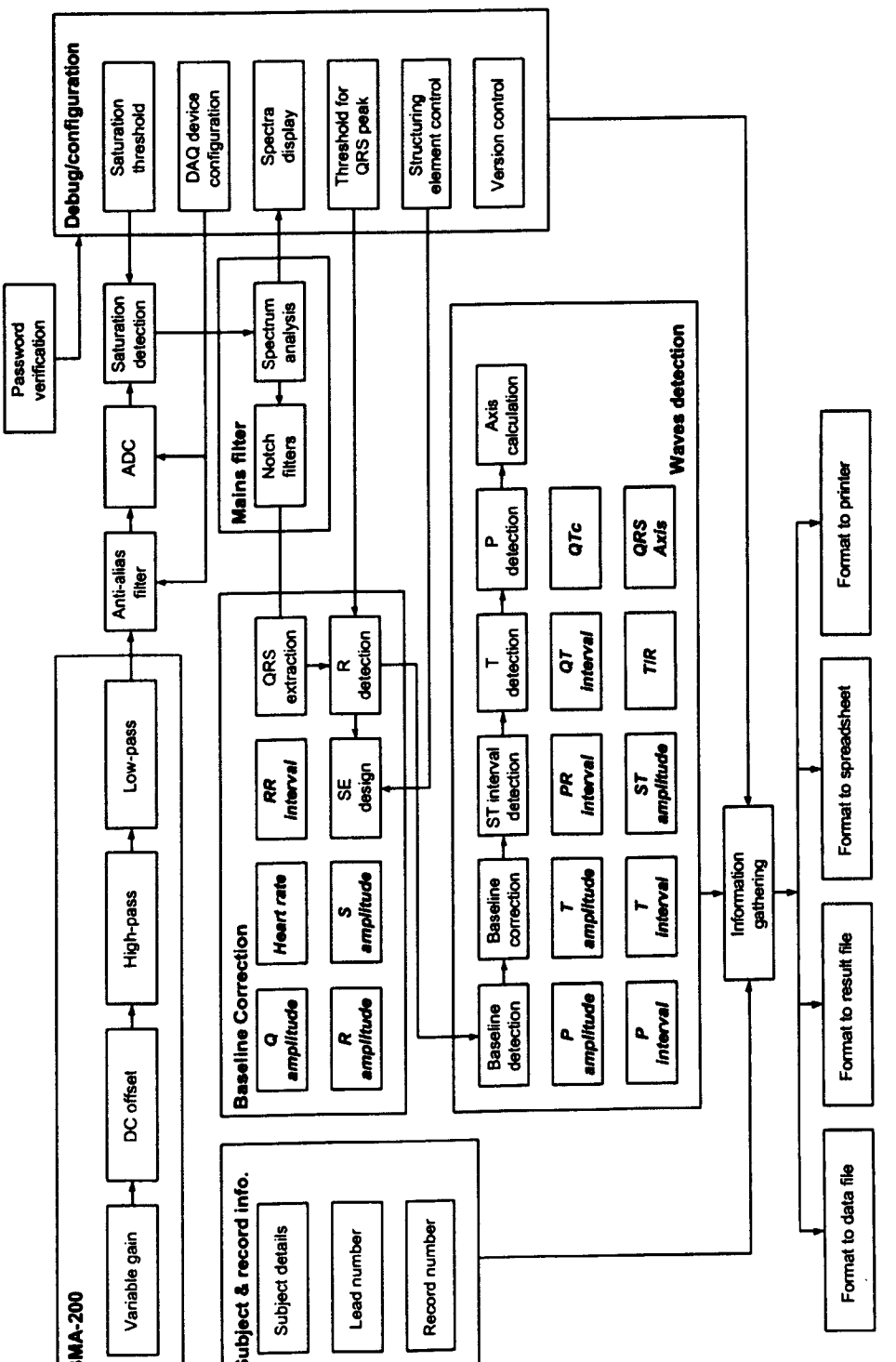

Figure 5.2: Software architecture of the system

5.2.1 Mains interference filtering

Finite Impulse Response (FIR) filter is commonly used for filtering the 50 Hz mains interference, e.g., the algorithms proposed in [100] [101] [102]. However, the large number of coefficients involved in theses methods results in heavy computational load.

For reducing the amount of calculation so that to allow real-time processing, an Infinite Impulse Response (IIR) filter was chosen for filtering mains interference. The design procedure is the pole-zero placement method [103], with notch frequency at 50 Hz, width 5 Hz and sampling frequency at 600 Hz.

The mains interference component in the ECG signal may be rejected by placing a pair of zeros on the unit circle of the z-plane corresponding to 50 Hz, as shown in Figure 5.3. Hence the zero placement is $2\pi \times \frac{50}{600} = 0.523$.

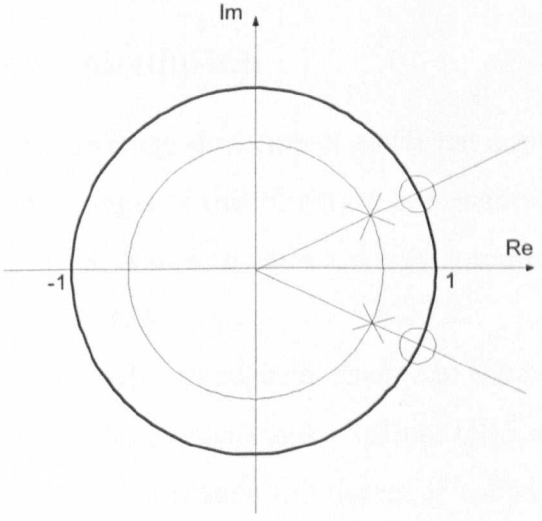

Figure 5.3: The pole-zero diagram for designing the mains interference filter

The position of the poles in relation to the zeros determines the sharpness and amplitude response at either side of the notch. The poles are placed on the same angle as the zeros with a radius $r < 1$ and $r \approx 1 - \frac{\mathrm{BW}}{f_s}\pi$, where BW is the required notch width, f_s the sampling rate. Hence $r = 1 - \frac{10}{600}\pi = 0.9476$.

Following the method given in [103], the transfer function can be derived as follows:

$$H(z) = \frac{z^2 - 1.732z + 1}{z^2 - 1.6413z + 0.898}.$$

Therefore the difference equation is:

$$y(n) = x(n) - 1.732x(n-1) + x(n-2) + 1.6413y(n-1) - 0.898y(n-2),$$

where y is the output signal, x the input signal and n the index of samples. Hence the coefficients of the notch filter are $a_0 = 1$, $b_0 = 1$, $a_1 = -1.732$, $b_1 = -1.641$, $a_2 = 1$, $b_2 = 0.898$. The implementation of the filter was achieved by using a standard digital filter provided by LabVIEW with the coefficient values as parameters.

The result of filtering a signal (Figure 5.6) containing mains interference is demonstrated in Figure 5.7.

5.2.2 QRS axis calculation

The QRS axis is the average direction of electrical activity during ventricular depolarisation. The angle of this direction is measured on the coordinate system given in Figure 5.4, where the directions of standard bi-polar and unipolar leads are also illustrated.

The QRS axis may shift due to physical change in the position of the heart, chamber hypertrophy, or conduction block. Normal QRS axis of adult is from around -30 to +90 degrees. Less than -30 degree is called left axis deviation, whereas greater than +90 degree is called right axis deviation.

Determining QRS axis by inspection

The inspection method of determining axis requires to check QRS orientation in specific leads. It is usually much faster than the vector method mentioned later, and provides the same clinical information. This method can be carried out as follows:

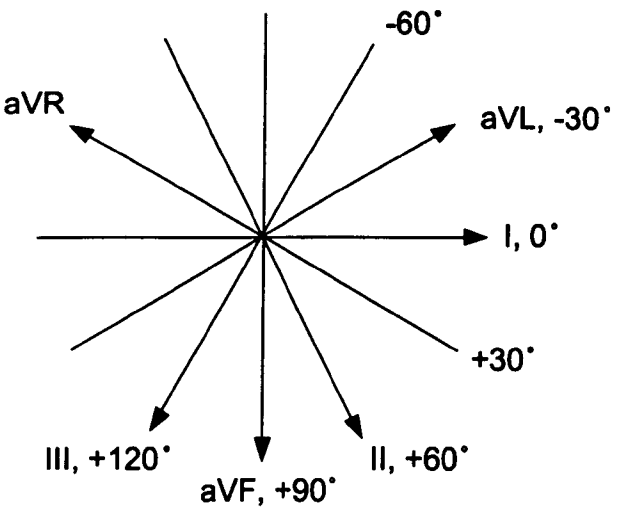

Figure 5.4: The frontal plane coordinate system for measuring QRS axis

- First check lead I. If the QRS is "positive overall" (comparing negative deflections to positive deflections), right axis deviation is ruled out.
- If the QRS in lead I is negative, right axis deviation is mild. Now check lead aVR. If the QRS is overall positive, right axis deviation is definite.
- Now check for left axis deviation by inspecting lead III. If the QRS is overall positive, left axis is ruled out.
- If the QRS is negative in III, check lead II. If lead II also shows an overall negative QRS, left axis deviation is diagnosed.

Vector method for determining QRS axis

Determining QRS axis by the vector method is most easily done using lead aVF and lead I. These leads are convenient because in the coordinate system, they are at a perpendicular angle to each other.

In this method, the first is to determine lead I's QRS size and orientation (the *algebraic sum*) by subtracting the S wave height from the R wave height. Then determine lead aVF's algebraic sum of QRS in the same way.

Start from the origin of the coordinate, plot out the overall lead I QRS size on the horizontal line representing lead I. Positive is to the right, negative to the left. From the same origin, plot out the QRS size of lead aVF on the line representing lead aVF. If aVF's QRS is positive, draw downward. If negative, draw up.

Draw lines perpendicular to the end points of the two lines, to form a rectangle. Draw a line from the origin of the coordinate to the other corner of the rectangle. The orientation of this line represents the QRS axis.

A computerised method for QRS axis calculation

From the above vector method, it is clear that the QRS axis can be obtained by calculating the vector sum of the algebraic sums of QRS on various leads. Since in our ECG system only lead I, II and III are available, to obtain the QRS axis from these three signals, a formulae using the measurement principle of Einthoven trigonometry (Section 4.2) is employed.

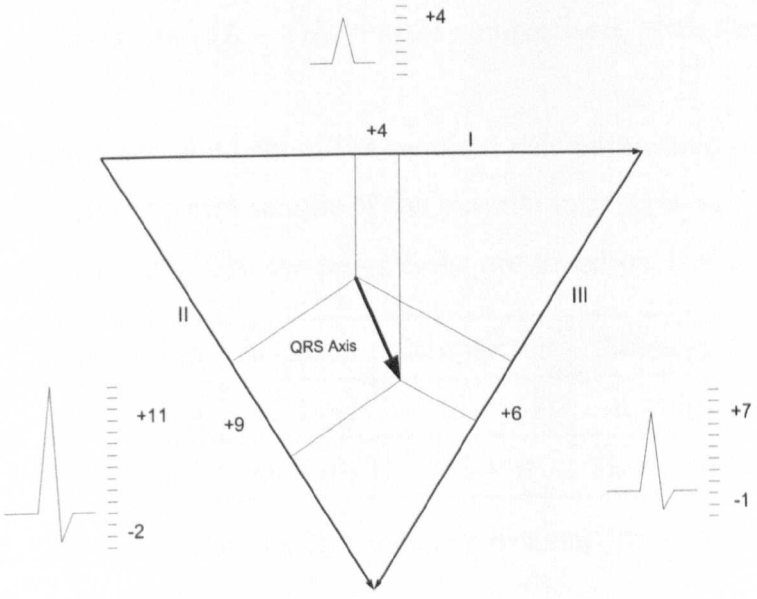

Figure 5.5: Calculation principle of QRS axis deflection angle

Figure 5.5 shows the principle of the algorithm, where the QRS axis is the

vector sum of any two algebraic sum of QRS, from lead I, II or III. Therefore the angle of the QRS axis β can be derived, e.g., from lead I and II, as

$$\beta = \arctan \frac{2II - I}{\sqrt{3}I},$$

where I and II are the algebraic sum of lead I and II respectively.

5.2.3 Morphological operators

A fast implementation of 1-D grey-scale morphological operations is adopted in the system [78]. In this method a special SE is required, which is a flat segment with its origin at the centre and all the values equal to zero (Chapter 4).

With such an SE, this algorithm avoids unnecessary operations and does not maintain intermediate results. Therefore it is much faster than the classical cascade methods for opening, closing, open-closing and close-opening operations, where the intermediate results are needed. For example if the signal size is $N = 512$ and the SE size is $L = 3$, the calculation required for erosion is $LN = 1536$ additions and $(L-1)N = 1024$ comparisons, with the size of the buffer is N.

Table 5.1 shows the numbers of the required calculation and memory unit of the algorithm (for the first sample of the output) in respect to L, the size of the SE. The numbers given in the parenthesis are based on $L = 3$.

Operation	Addition	Comparison	Memory
Opening	2L-2 (4)	2L-2 (4)	3L-3 (6)
Open-closing	4L-4 (8)	4L-4 (8)	5L-5 (10)

Table 5.1: Required calculations and memory element for 1-D morphological operations

5.2.4 User interface

The user interface of the system provides the user with a convenient means for performing various tasks as described below.

Data acquisition: Provides an interactive interface (Figure 5.6) for on-line acquisition of an ECG signal, as follows

- Entering subject information, including name, gender, unit number, date of birth, birth weight, gestational age at the time of recording, and notes or comments on the subject.
- Record information, including record number, lead number, time and comment on the record.
- An indicator to identify the arrangement of leads.
- An interactive interface for acquiring signals.
- Loading and displaying the ECG record file.
- An alarm to indicate amplifier saturation.

The interface shown in Figure 5.6 contains an acquired ECG signal with power-line interference.

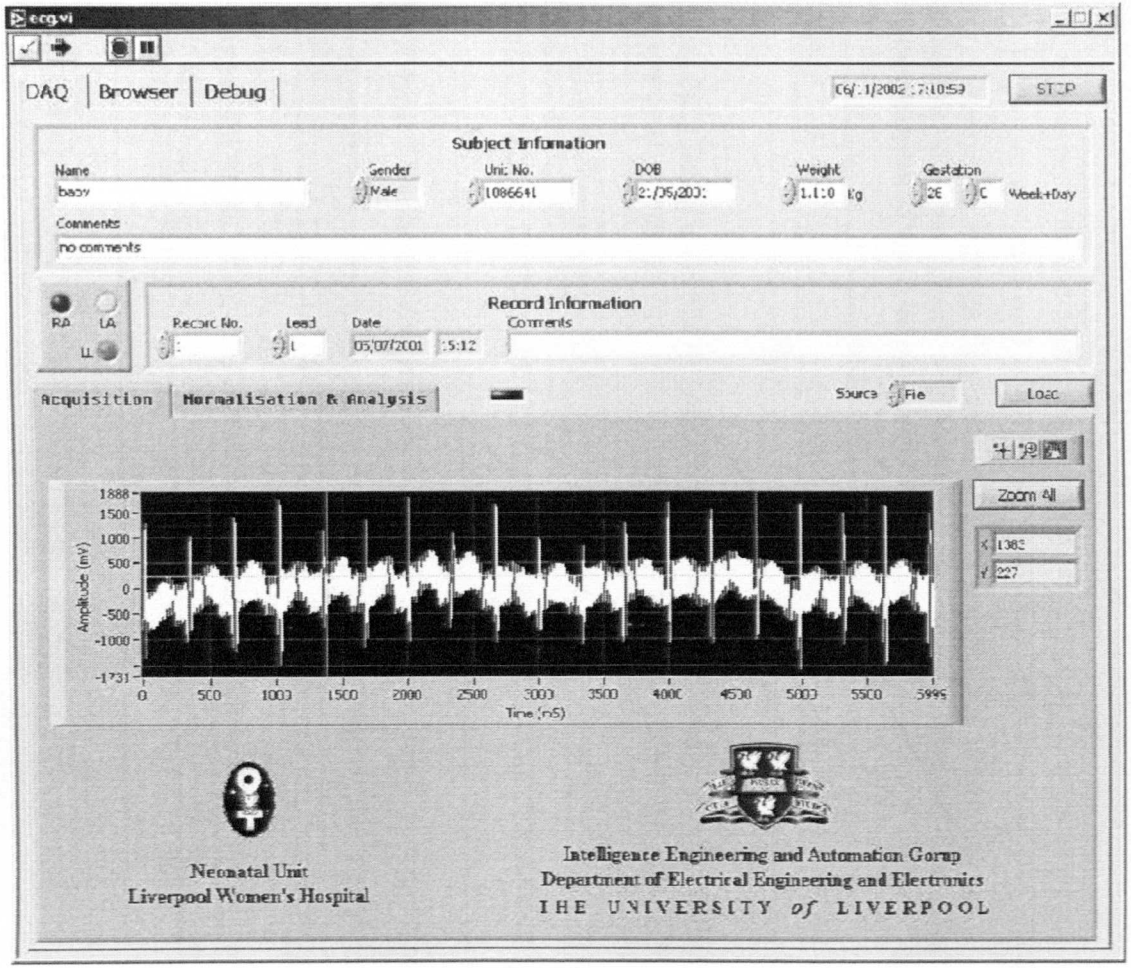

Figure 5.6: The data acquisition interface, with an acquired noisy ECG

Data processing: In addition to subject and record information, this interface also provides the processing and analysis results for the acquired signal, as follows

- The noise filtered signal (for diagnostic purposes, the result of baseline correction is not shown).
- Markers on the signal to indicate, e.g., peaks of the P, R and T waves, beginning and end of the PR, QRS and QT intervals etc., with corresponding legends displayed on the interface for reference.
- Results of processing, including quantitative measurements of heart rate, interval and amplitude measurements and their variation.
- Printing of signals and results.

The interface shown in Figure 5.7 contains the noise filtered version of the signal in Figure 5.6.

Result browsing: This provides multi record browsing for comparison of ECGs acquired at different times, including waveform browsing, trend display, a table of measurements, and a buffer for exporting data. The interface shown in Figure 5.8 contains the trends of all measurements over the number of record.

Result export: This provides signal selection and export. The exported files are compatible with Microsoft Excel. The interface shown in Figure 5.9 contains a table of all the results available from the subject, from which the user can select the data to be exported and append them to the buffer.

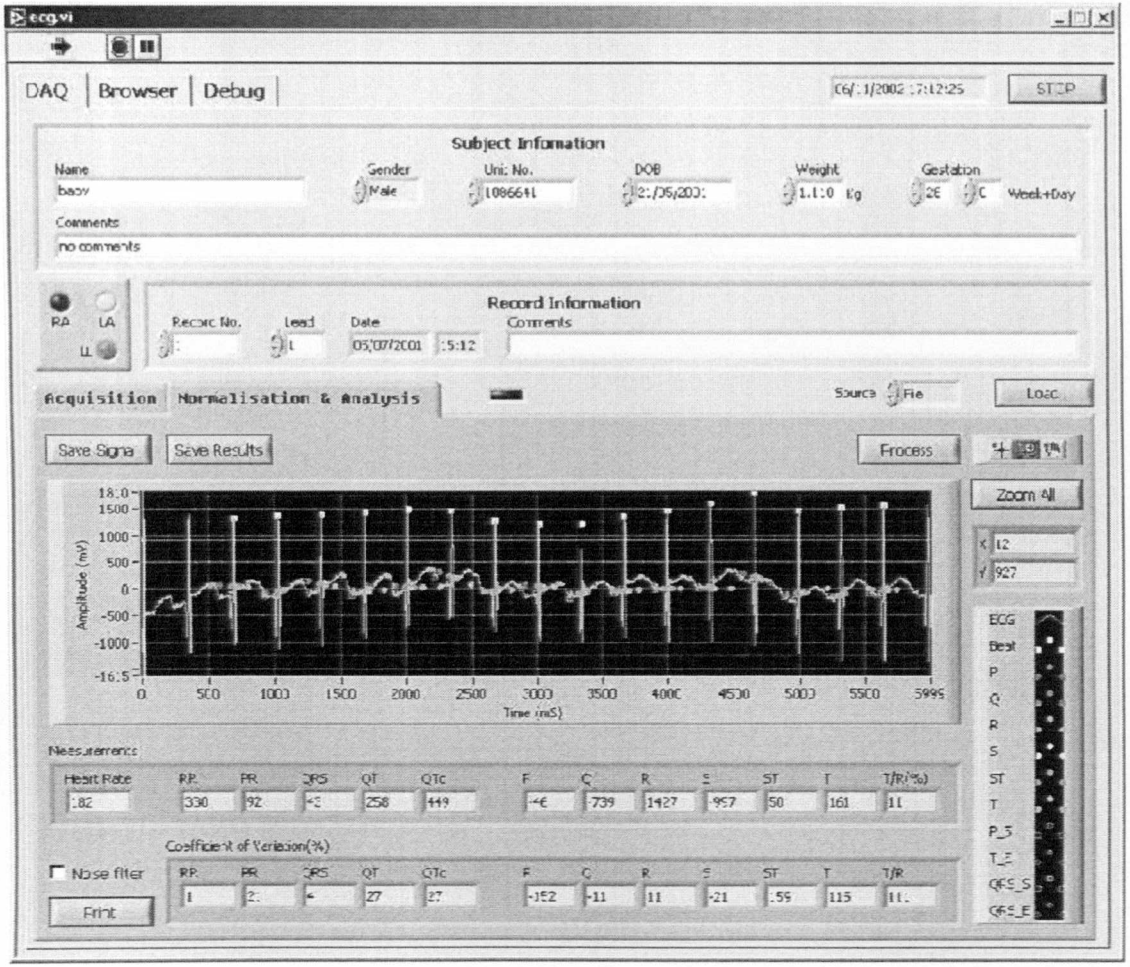

Figure 5.7: The processed ECG, with markers and measurements of each ECG component

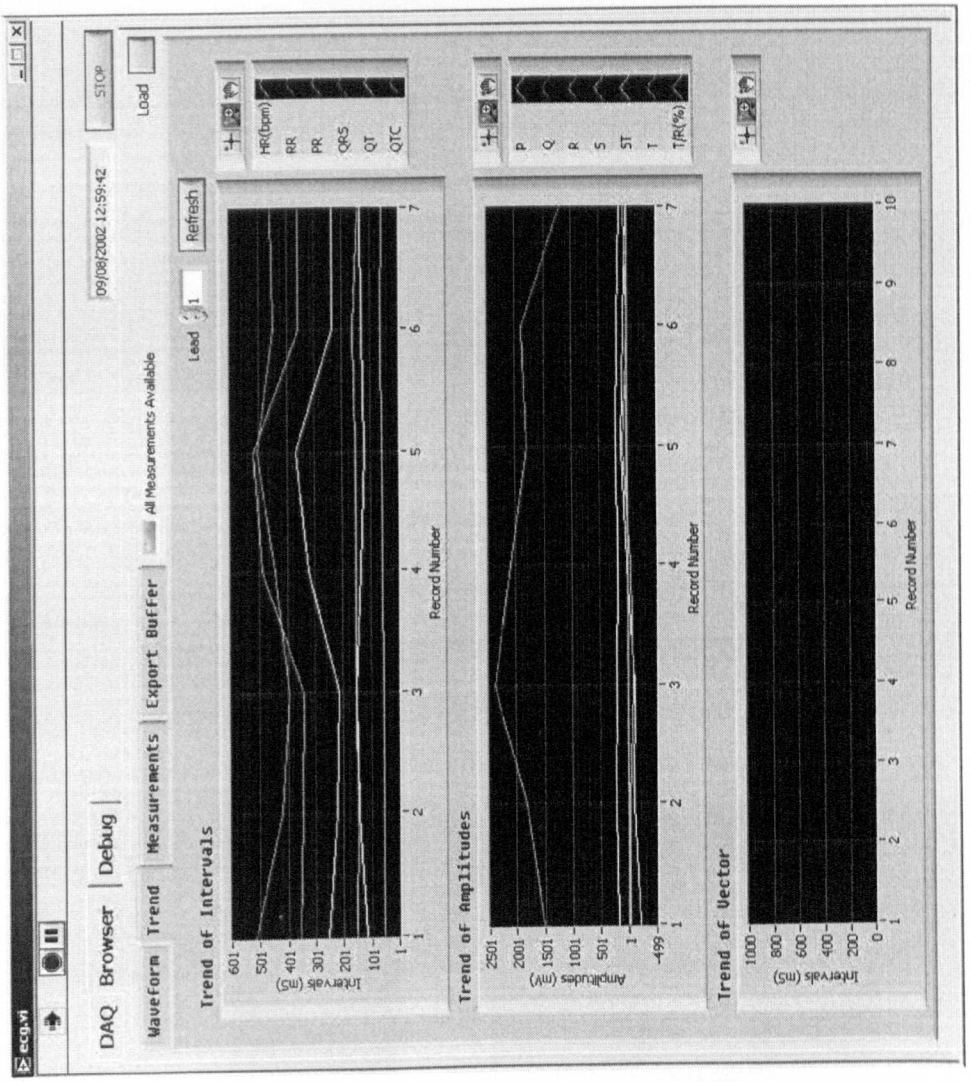

Figure 5.8: The trend of ECG parameters from multiple records

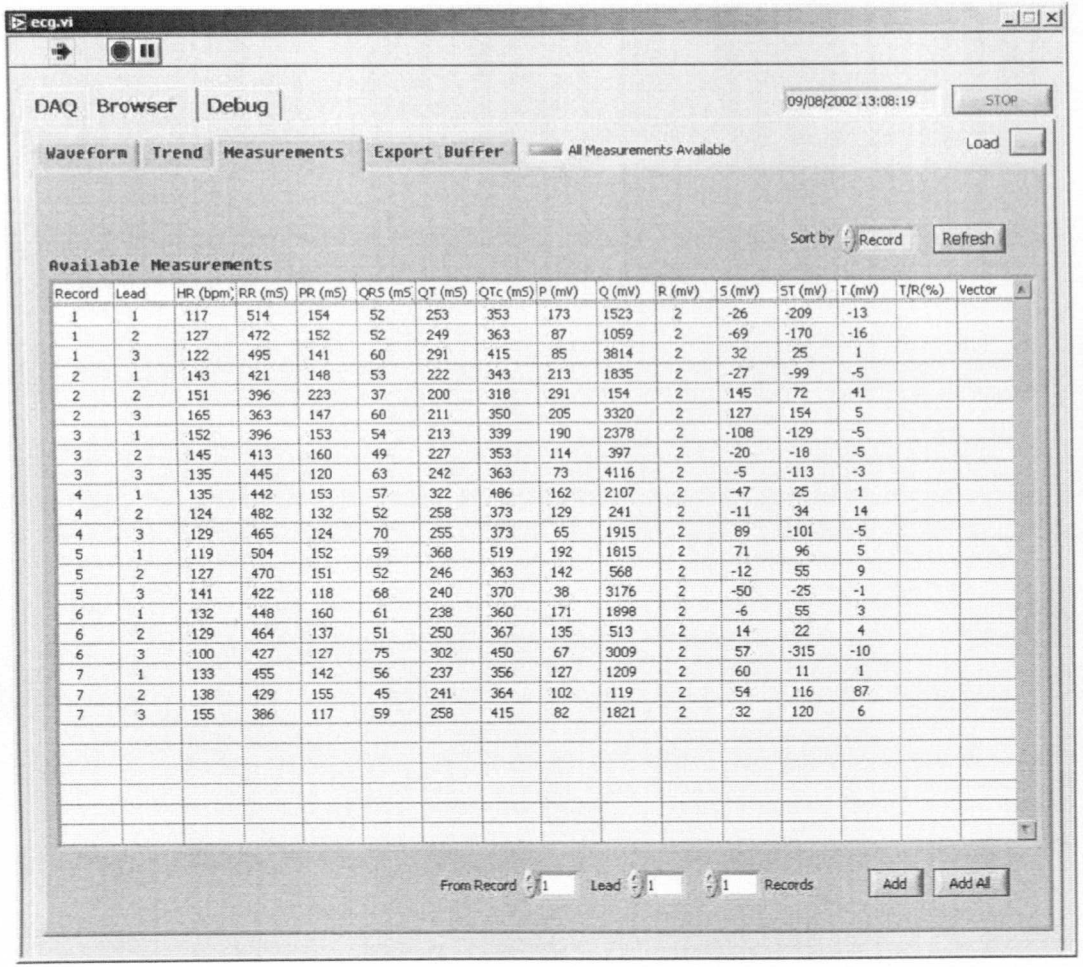

Record	Lead	HR (bpm)	RR (mS)	PR (mS)	QRS (mS	QT (mS)	QTc (mS)	P (mV)	Q (mV)	R (mV)	S (mV)	ST (mV)	T (mV)	T/R(%)	Vector
1	1	117	514	154	52	253	353	173	1523	2	-26	-209	-13		
1	2	127	472	152	52	249	363	87	1059	2	-69	-170	-16		
1	3	122	495	141	60	291	415	85	3814	2	32	25	1		
2	1	143	421	148	53	222	343	213	1835	2	-27	-99	-5		
2	2	151	396	223	37	200	318	291	154	2	145	72	41		
2	3	165	363	147	60	211	350	205	3320	2	127	154	5		
3	1	152	396	153	54	213	339	190	2378	2	-108	-129	-5		
3	2	145	413	160	49	227	353	114	397	2	-20	-18	-5		
3	3	135	445	120	63	242	363	73	4116	2	-5	-113	-3		
4	1	135	442	153	57	322	486	162	2107	2	-47	25	1		
4	2	124	482	132	52	258	373	129	241	2	-11	34	14		
4	3	129	465	124	70	255	373	65	1915	2	89	-101	-5		
5	1	119	504	152	59	368	519	192	1815	2	71	96	5		
5	2	127	470	151	52	246	363	142	568	2	-12	55	9		
5	3	141	422	118	68	240	370	38	3176	2	-50	-25	-1		
6	1	132	448	160	61	238	360	171	1898	2	-6	55	3		
6	2	129	464	137	51	250	367	135	513	2	14	22	4		
6	3	100	427	127	75	302	450	67	3009	2	57	-315	-10		
7	1	133	455	142	56	237	356	127	1209	2	60	11	1		
7	2	138	429	155	45	241	364	102	119	2	54	116	87		
7	3	155	386	117	59	258	415	82	1821	2	32	120	6		

Figure 5.9: The table of measurements to be exported, from multiple records of a baby

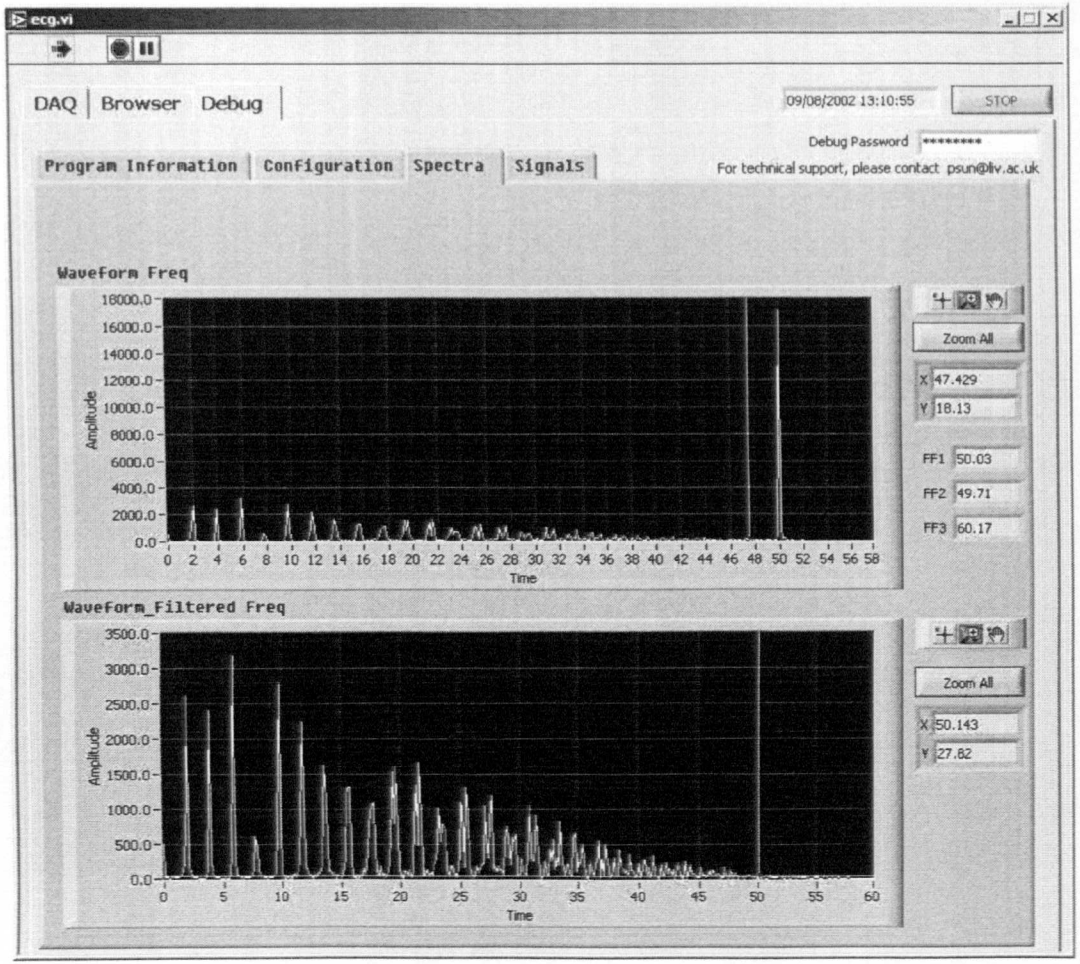

Figure 5.10: The debugging interface, with spectra of input and mains interference filtered signals

Debugging: provides an interface to investigate intermediate signals, and to adjust the parameters for the signal processing algorithms in the system (Figure 5.10), including

- Information of the program, e.g., its version, data file formats, etc.
- Configuration of the parameters used in signal filtering and morphological operations.
- Spectra of the acquired signal, for investigating the performance of the noise filtering algorithm.
- Intermediate signals of morphologically processing the signal.

This function is for developers only and is protected by a password.

5.3 Conclusions

In this chapter, the implementation of the integrated neonatal ECG analysis system is introduced. This system was designed to aid neonatologists in the Liverpool Women's Hospital, in diagnosing complicated cases, conducting research, archiving important results, creating an electronic ECG data bank etc. It is preferred when high-precision electrocardiography is needed, especially in the case of neonatal ECGs that have a higher heart rate than adults. It also aims to be a valuable tool for computerised analysis, particularly as it allows the user to examine the reliability of the results. Important features like ST segment measurement, trend analysis and cardiac vector calculation provide the opportunity of adding diagnostic power to the routine examination and the standard interpretive features. Theoretical support, algorithm development (Chapter 4), interaction with physicians, hardware and software design, debugging, system validation (Chapter 6) are integrated in this system, which provides flexibility and modularity, and is continuously upgradable.

Chapter 6

Pilot trial of the integrated ECG analysis system

This chapter describes a set of experiments that were devised in order to determine the general variability of ECG measurements with the prototype system (see Chapter 5), as well as to validate the morphological techniques in neonatal ECG signal processing and analysis (see Chapter 4). With the assistance of a medical student, these experiments were carried out in Liverpool Women's Hospital, and took approximately one month to finish. The measurements obtained and the statistical data derived are given in Appendix C and discussed in following sections.

6.1 Background

The study was carried out on a busy medical neonatal intensive care unit located in the Liverpool Women's Hospital. Babies included in the study were all resident on the neonatal unit at the time, within a variety of locations (intensive care unit, high dependency rooms and nurseries). Parents were provided with an appropriate amount of information, both in verbal and written form,

before giving written informed consent. With regards to ethical considerations, the procedure involved was not likely to cause any distress or discomfort to the subject. Nor was there any potential harm that could result from participating in the study. As this was a pilot trial of the prototype system, babies not participating in the research would not be put at any disadvantage with respect to interventions and general management.

To validate the prototype system, the normal ranges of neonatal ECG measurements were firstly examined. Fowler and Finlay [104] documented these normal ranges (mean values) for premature babies as being:

- heart rate 141 beats per minute,
- PR interval 0.12 second,
- QRS interval 0.04 second,
- QTc 0.412 second,
- P wave amplitude 0.3 mV,
- R wave amplitude 0.4 mV,
- axis of the QRS complex 107-135° depending on gestational age.

These values are extremely similar to those quoted by Hubsher [73] thus can be assumed to be an accurate guide.

The ECG waveform was recorded by the analyser (see Chapter 5), which was in turn linked to standard ECG leads used routinely on the neonatal unit. Where no ECG was being routinely monitored, leads were applied for the duration of the signal acquisition (approximately five minutes). In total four leads were used: right arm (RA), left arm (LA), right leg (RL) and left leg (LL). These were each labelled appropriately to ensure correct recording of leads I, II, and III. A combination of three leads was plugged into the acquisition machine at a time (see Table 4.1). To get a lead I recording LA, RA and RL were used. To get a lead II recording LL, RA and RL were used. To get a lead III reading

LL, LA and RL were used. The RL lead used in all readings was needed as the reference signal for the differential amplifier used in the system.

The analyser automatically filters noise, identifies P, Q, R, S, ST and T waves, recognises specific wave segments and calculates key parameters. The following segments were automatically calculated: RR interval, PR interval, duration of the QRS complex, QT interval and the corrected QT interval (QTc). The QTc was calculated using Bazett's formula (as described in (4.3.3)) and provides the QT interval corrected with the heart rate. The amplitude of the P, R, and T waves were also calculated alongside the ST segment amplitude and T/R ratio. The system also automatically calculated the heart rate and axis of the QRS complex. As described in Chapter 5, the system provides a user friendly interface, which is designed in such a way that someone without detailed knowledge of the signal acquisition and analysis techniques can use it without much difficulty.

6.2 Trial method

There are three sets of experiment devised and carried out in the pilot trial, as follows.

Experiment I

Aims to discover the hourly changes in ECG characteristics of stable babies.

Five stable pre-term babies were monitored every 12 minutes, for a period of one hour each, i.e., five measurements for each baby. This approximated to one measurement every twelve minutes. Stable was defined clinically as having no additional oxygen requirements or serious problems, thus being nursed on the neonatal unit due to immaturity.

Experiment II

Aims to discover the daily changes in ECG characteristics in neonates of different gestations and postnatal ages.

Babies were divided into three groups depending on gestational age at birth. Each group contained three babies. Groups contained a mixture of stable and unwell babies as the gestational age was the only variable to be tested. These were group A (24 to 26 weeks gestation), Group B (27 to 29 weeks gestation) and Group C (30 to 32 weeks gestation). An ECG recording was done on day 1 of the experiment and then further recordings taken once daily on days 3, 5 and 7 thereafter.

Experiment III

Aims to discover the changes in ECG characteristics during the first 72 hours after birth.

Two babies admitted to the unit immediately after birth had ECG recordings done from as close to birth as practicable, with further measurements every 12 hours for the first 72 hours of life. These were to be followed by single measurements on days 4, 7 and 10 of life to detect any further changes occurring after the initial measurements.

Statistical analysis

The coefficient of variation (CV, see (4.5.1)) was calculated for each measurement, to enable examination of the size of the standard deviation (SD, see (4.5.2)) relative to the mean. This measures the relative variation where groups of values have very different means. The CV is provided as a percentage.

The median value and range were also calculated for each parameter. The median value was used in preference to the mean due to the fact that it minimises the impact of extreme measurements that may be inaccurate, on the

value.

6.3 Results of the trial

In total 16 babies on the neonatal unit took part in this study, conducted over a period of four weeks. All of these babies except one were pre-term. Details of individual babies can be found in Table B.1 of Appendix C. It took approximately 5 minutes to acquire the signals for all three leads. This process was extremely straight forward apart from the problem of movement of the babies. Skeletal muscle movements caused the quality of the signal to be greatly affected, with repeated attempts at recording necessary if babies were unsettled. This was more of a problem with the larger babies and those of greater gestational age.

For babies in experiments II and III the clinical risk index for babies (CRIB, see Table A.1) score was calculated [105] [106]. This neonatal scoring system is a robust index of neonatal risk that is more accurate than birth weight and simple enough for routine use. The CRIB score was deemed not to be relevant to the stable babies in experiment I therefore not calculated. As experiment II included babies with different gestational and postnatal ages, the corrected gestational age is included in tables to ease comparison.

The original measurements provided by the analysis system, from which the statistical calculations have been made, are included in Tables C.1 to C.3.

The results of the statistical calculation are given in Appendix C, where Table C.4 is for experiment I; Tables C.5 to C.7 for experiment II groups A, B and C, respectively; Table C.8 for experiment III. For each baby results are given as median values of the multiple measurements, with ranges (minimum–maximum) shown in brackets. Tables illustrate values regarding both the intervals and amplitudes of relevant ECG parameters. For each parameter the CV is given. The number of heart beats recorded is also tabulated alongside

both medians and ranges for heart rate (HR) and axis of the QRS complex (AQRS).

A number of modifications to the original study design were made. It was intended that the babies in experiment III would be followed up beyond the first 72 hours of life on days 4, 7 and 10. However due to the four week time constraint of this research this was not possible. It was also not possible to do a measurement at 72 hours of age for baby 16 for the same reason, thus measurements cover the first 60 hours of life only. Baby 10 only had three of the four measurements done due to clinical deterioration of the infant on the day. Babies 8 and 11 do not have a complete set of ECG recordings because the amplifier was saturated. It is likely that this noise was from other pieces of monitoring equipment in the room.

6.4 Discussion

In terms of validation of the morphological technique some measurements can certainly be considered both useful and reliable. However others are questionable and should possibly be rejected as accurate values. Measurements of ECG parameters are found to be near to the reference values cited previously. In general, analysis of the results reveals specific trends. For the purpose of our work a CV value of 15% or less is considered acceptable variation. It is evident throughout the results of all three experiments that interval CV values are generally lower than the amplitude ones. In particular, the amplitudes of the P waves and ST segments show consistently high CV values in each experiment. As experiment I had all measurements taken within one hour these could be considered the most informative results with regards to the accuracy of the morphological technique. This is because a smaller hourly variation would be expected, compared to daily. Thus high CV values are more likely to reflect inaccurate measuring of parameters.

In experiment I, the median CVP values are unacceptably high for all five babies ranging from 23-108%. The median CVST values are similarly high (see Table C.4 (c)). The ranges for the CVP values contain some figures that could be considered rejectable eg. 108% for baby 3. Again this pattern is repeated for the CVST ranges.

It must be recognised that there may be another explanation for this trend. It is possible that the small values for parameters such as the P wave and ST segment amplitudes create a smaller mean value which when divided into the SD gives a larger CV value. One may notice that when compared to other small values such as the duration of the QRS complex, the CV values for the aforementioned parameters are still much larger. This factor indicates that perhaps this is a case of inaccuracy. However, since the waveform of QRS complex is dominant in terms of amplitude, its beginning and ending and therefore the interval can be determined with less difficulty and higher accuracy. This is confirmed by the lower CV when the ST segment is elevated, i.e., the larger the ST value the lower its CV (see Table C.4). Therefore, as long as the ST segment is not elevated, a higher level of variation is not much a problem for its interpretation. Nevertheless, a more intuitive representation and indication of the ST segment elevation, instead of solely using the amplitude, should be considered in a later study. Inaccuracy regarding calculation of the ST elevation is significant to the research into neonatal myocardial ischaemia, mentioned previously.

Analysis of the results for experiment II shows that Group A has the highest number of CV values above 15% (11 in total) followed by Group B (9 in total) then Group C (4 in total). This observation suggests that gestational age may be a factor in the variability of ECG characteristics, where measurements are made every other day. It is also important to acknowledge sources of potential bias regarding the results alongside limitations of the study. The most obvious of these sources is the small sample size of the study. This was

due to two factors. Firstly, the short time period available for the research, and secondly the fact that the technology is still in the early stages of development. The small sample size was deemed appropriate for such a preliminary trial of the technique. It is also necessary to note that the varied postnatal ages of babies could have affected results in experiments I and II. Another possible source of bias is the fact that extremely unwell babies were not included in the experiments. This was because when approached, nursing staff understandably felt it to be inappropriate.

6.5 Conclusion

There are numerous ways in which this study could be extended to form a more comprehensive analysis of both the reliability of the new technique and the variables affecting the neonatal ECG. Using the existing data, it would be useful to carry out a more extensive statistical analysis of the impact of variables such as CRIB score and gestational/postnatal age. The changes occurring in the hours after birth could also undergo a more detailed analysis.

If a more reliable multi-channel ECG amplifier, instead of the generic single-channel bio-amplifier being used, is available, it would present a relatively easy method of ECG measurement in neonates, causing minimal disturbance to the babies.

This technology has the potential to fill the existing gap present in neonatal monitoring. It could also help the progression of research in fields such as the link between birth asphyxia and myocardial ischaemia. Nevertheless, the findings of this study are valid and useful in the on going process of evaluating the new acquisition and analysis system for neonatal ECGs, as well as in regard of the automated analysis of many clinically useful parameters. It is delivered, after a few refinements, as a clinical research tool for a comprehensive study on neonatal ECG, to extend the research to a larger sample size.

Chapter 7

Concluding remarks

This chapter concludes the dissertation. It summarises the major results of the presented research work and indicates directions for future investigations based on this work.

7.1 Goals achieved

This thesis is concerned with exploiting and applying morphological signal processing techniques for feature identification and extraction, with promising results obtained from the applications on power transformer inrush waveform identification and ECG signal processing. Morphological algorithms for neonatal ECG analysis are also implemented as an integrated system for use in medical research, and results from a pilot trial carried out in clinics are presented.

7.2 Problems

One of the major limitations for using MM is the lack of analytical methods. This is due to the nonlinear nature of the MF operators, as we have seen on the evaluation of the neonatal ECG processing results. The next drawback

is in assessing the transformer inrush current detection algorithm. It was not possible to test this approach in a real environment, as there are stringent limits on undertaking a trip test in power transmission substations. Also there were only very limited resources of logged fault and inrush waveforms available. In general, apart from simulation, it has not been applied or tested on a real-time basis.

A limitation of the research on neonatal ECG is in regard to the application of Bazett's formula. This subject adapted method is not fully justified unless it has been investigated on a comprehensive neonatal ECG database (such databases are only available for adults), or a larger number of babies, which was not possible as the time for this research is limited.

7.3 Recommendations for future work

This section outlines additional areas that can be investigated, to further develop and improve the algorithms and applications described in this thesis.

7.3.1 Structuring element design and optimisation

Further research in this direction is likely to reveal additional properties of the design and optimisation of the SEs, particularly in the cases of ECG signal and transformer inrush current detection, in the operator design and thus contribute to our understanding of how such SEs act on the underlying features of the signals.

7.3.2 Real-time optimisation

Real-time optimisation is worth investigating further. The present system for transformer inrush current detection is optimised on pre-recorded data to give an indication of a class of transformer. Starting with this it is possible

to optimise this further to a more generic form that satisfies the demand of prompt response time. For the neonatal ECG analysis system, it is on an on-line basis at the moment. If it could provide its results in real-time, it would be helpful for early intervention of the babies at risk. Also it can be further refined to become a commercial product, with additional experiments to justify its methodology and clinical usefulness.

7.3.3 Fetal ECG signal acquisition and processing

This is highly desirable due to the noninvasive nature of the process. Moreover, as an extension to the current study on neonatal ECGs, morphological filtering seems appropriate for discovering the singular points of the baby and the mother, therefore allow separation between these signals.

Appendix A

The CRIB Score

The *clinical risk index for babies* (CRIB) score has been developed by the International Neonatal Network to simplify and refine the assessment of neonatal mortality and morbidity [106], and sometimes of the general outcome, in *very low birth weight* (VLBW) preterm infants.

Based on routine data collected during the first 12 hours after birth, this score derives from six factors as given in Table A.1, three of which have an intrinsic nature (birth weight, gestational age, and the presence or absence of congenital malformations) and three indices of physiological status (maximum base excess, minimum and maximum appropriate FiO_2), which together determine the final score defined as

$$\text{CRIB} = \text{BW} + \text{GA} + \text{CM} + \text{MBE} + \text{MinAF} + \text{MaxAF}. \qquad \text{(A.0.1)}$$

The CRIB score ranges from 0 to 23; with increasing scores there is increased morbidity and mortality [105]. As illustrated in Table A.2, major cerebral abnormalities on ultrasound have been found in 5% of surviving VLBW preterm infants at discharge home with CRIB scores 0–5, 12% of those with scores 6–10 and 20% of those with scores > 11.

Factor	**Score**
Birthweight (gram)	**BW**
> 1350	0
851–1350	1
701–850	4
≤ 700	7
Gestational Age (weeks)	**G**
> 24	0
≤ 24	1
Congenital Malformations	**CM**
None	0
Not acutely life threatening	1
Acutely life threatening	3
Maximum Base Excess in first 24 hours (mmol/L)	**MBE**
> −7.0	0
-7.0 to -9.9	1
-10.0 to -14.9	2
≤ −15.0	3
Minimum Appropriate FiO_2 in first 12 hours	**MinAF**
≤ 0.40	0
0.41–0.60	2
0.61–0.90	3
0.91–1.00	4
Maximum Appropriate FiO_2 in first 12 hours	**MaxAF**
≤ 0.40	0
0.41–0.80	1
0.81–0.90	3
0.91–1.00	5

Table A.1: The CRIB score

CRIB score	hospital mortality	major cerebral abnormality in survivors before discharge
0–5	8%	5%
6–10	38%	12%
11–15	70–76%	20%
> 16	85–90%	20%

Table A.2: CRIB scores with morbidity and mortality rate

Appendix B

Information of the babies involved in the pilot trial

This appendix contains the clinical data of the babies involved in the pilot trial (see Chapter 6).

B.1 Details of the babies

Table B.1 gives the clinical data of the babies that took part in the study, including

Subject No. The reference number we arranged for the baby

Gender The gender of the baby

Unit No. The unit number arranged for the baby by the hospital

DOB Date of birth

BW Birth weight in kilograms

Gestation The gestational age of the baby in weeks/days.

Subject No.	Gender	Unit No.	DOB	BW	Gestation
1	M	1086641	21/05/01	1.110	27+5
2	F	1088442	28/06/01	1.880	31+6
3 (Twin 1)	F	1088950	03/07/01	1.946	35+1
4 (Twin 1)	M	1088951	03/07/01	1.946	35+1
5	M	1088815	29/06/01	1.975	34+1

(a) Experiment I

Subject No.	Gender	Unit No.	DOB	BW	Gestation
6	M	1082429	02/03/01	0.750	28+5
7 (Twin 2)	M	1089127	06/07/01	1.690	32
8 (Twin 2)	M	1089128	06/07/01	1.842	32
9	F	1089224	08/07/01	1.685	33
10	F	1084418	05/04/01	0.636	26
11	M	1089138	06/07/01	0.815	24+5
12	M	1089194	06/07/01	1.226	28
13	M	1086052	09/05/01	1.036	26+1
14	M	1091109	13/07/01	0.880	25+6

(b) Experiment II

Subject No.	Gender	Unit No.	DOB	BW	Gestation
15	F	1089483	13/07/01	5.800	38
16	M	1089726	18/07/01	3.520	42

(c) Experiment III

Table B.1: Clinical data of the babies involved in the trial

Appendix C

Results of the pilot trial

The results of the pilot trial (see Chapter 6) for the MM based neonatal ECG analysis system are given in this appendix. A detailed description of the algorithms and the system can be found in Chapter 4 and Chapter 5.

C.1 Results produced by the analysis system

Table C.1 to Table C.3 contain the original ECG parameters measured by the analysis system, from experiment I to experiment III. These measurements are the raw data from which the calculation of the statistical results (see Section C.2) is made. The information included is

Rec. Subject number followed by the record number

Vec. Cardiac vector in degrees

Bt./HR Number of heart beats in the record, followed by the heart rate in beats per minute

RR, PR, QRS, QT, QTc Interval measurements in seconds (RR normalised ratio for QTc)

P, R, T, ST, T/R Amplitude measurements in millivolts (R normalised ratio for T/R)

Data of intervals and amplitudes are given as median/CV (coefficient of variation, see (4.5.1)), measured from lead 2. A more detail description of the recording procedure can be found in Chapter 6.

C.2 Statistical results

The statistical results for each baby are given in Table C.4 to Table C.8, including information of the heart rate and QRS axis (AQRS), interval and amplitude measurements. Measurements are given as the median value of multiple records, with ranges shown in brackets. For each interval and amplitude measurement the coefficient of variation (CV, see (4.5.1)) is given as a percentage.

For babies in experiments II and III the CRIB score (see Appendix A) is calculated. As experiment II included babies with different gestational and postnatal ages, the corrected gestational age is included in tables to ease comparison.

			Intervals(Second)					Amplitudes(mV)				
Rec.	Vec.	Bt./HR	RR	PR	QRS	QT	QTc	P	R	T	ST	T/R
1/1	98	14/158	0.38/2.2%	0.13/4.4%	0.047/1.8%	0.28/3.0%	0.45/2.4%	0.10/25%	0.81/6.9%	0.22/22%	0.11/66%	0.26/24%
1/2	87	12/142	0.43/3.8%	0.13/20%	0.048/4.0%	0.29/6.6%	0.44/6.3%	0.05/160%	0.90/9.28%	0.21/43.2%	0.088/74%	0.24/44%
1/3	92	13/159	0.38/1.6%	0.13/2.0%	0.047/1.7%	0.28/2.7%	0.45/2.2%	0.09/22%	0.66/3.5%	0.23/13.6%	0.10/24%	0.34/14%
1/4	101	12/146	0.41/2.6%	0.12/6.7%	0.053/3.1%	0.30/4.8%	0.46/4.5%	0.06/35%	0.94/8.4%	-0.15/27%	0.10/120%	-0.59/37%
1/5	94	12/141	0.43/3.5%	0.11/12%	0.057/7.8%	0.31/5.3%	0.47/4.7%	0.05/31%	0.95/5.2%	-0.13/25.4%	0.014/86%	-0.13/27%
2/1	232	13/152	0.39/0.35%	0.15/6.3%	0.06/2.9%	0.38/2.6%	0.44/2.7%	0.12/13%	0.28/13%	0.33/8.9%	0.18/22%	1.18/47%
2/2	221	12/140	0.43/2.3%	0.17/9.3%	0.06/2.0%	0.28/0.71%	0.43/1.3%	0.12/16%	0.34/6.5%	0.31/6.6%	0.18/12%	0.92/12%
2/3	229	13/149	0.40/0.5%	0.14/6.5%	0.055/1.3%	0.28/3.1%	0.44/3.1%	0.092/9.2%	0.25/5.6%	0.31/5.1%	0.17/9.0%	1.2/16%
2/4	179	13/153	0.39/1.0%	0.14/5.7%	0.05/2.0%	0.27/2.1%	0.43/2.1%	0.08/8.3%	0.24/5.8	0.24/4.7%	0.13/10%	1.0/9.2%
2/5	203	13/148	0.41/1.1%	0.14/8.4%	0.05/1.5%	0.27/2.1%	0.42/1.8%	0.10/21%	0.35/7.0%	0.28/6.6%	0.16/17%	0.79/15%
3/1	93	6/108	0.56/1.1%	0.14/33%	0.06/35%	0.33/0.68%	0.44/15%	0.037/108%	0.32/4.5%	0.068/31%	0.055/28%	0.21/32%
3/2	103	6/111	0.54/2.1%	0.13/27%	0.061/2.0%	0.33/0.37%	0.45/16%	0.058/77%	0.32/32%	0.15/42%	0.038/63%	0.46/53%
3/3	94	7/90	0.67/3.1%	0.19/14%	0.054/38%	0.32/1.0%	0.39/2.33	0.01/130%	0.30/15.9%	0.18/16%	0.034/140%	0.60/35%
3/4	101	8/94	0.64/1.6%	0.18/13%	0.058/39%	0.32/0.6%	0.40/0.93%	0.0033/200%	0.34/16%	0.13/27%	0.045/110%	0.38/34%
3/5	112	8/98	0.61/3.6%	0.12/13%	0.06/31%	0.32/0.66%	0.41/1.7%	0.07/60%	0.26/14%	0.16/25%	0.067/60%	0.62/32%
4/1	148	9/113	0.54/4.9%	0.21/2.2%	0.056/5.9%	0.37/1.9%	0.51/3.4%	-0.07/16%	0.90/0.90%	0.43/2.2%	0.15/5.2%	0.48/4.9%
4/2	137	9/116	0.52/3.9%	0.22/2.8%	0.054/8.7%	0.34/0.74%	0.48/1.6%	-0.06/40%	1.05/2.5%	0.43/6.9%	0.13/19%	0.42/10.0%
4/3	142	10/130	0.45/25%	0.17/25%	0.056/38%	0.34/14%	0.51/17%	-0.05/210%	0.95/36%	0.45/8.9%	0.18/37%	0.47/42%
4/4	159	9/116	0.52/2.7%	0.15/4.6%	0.052/5.5%	0.36/3.9%	0.50/3.4%	-0.09/45%	1.27/0.54%	0.47/3.1%	0.18/3.8%	0.47/4.9%
4/5	154	9/118	0.52/6.6%	0.16/10%	0.052/4.2%	0.35/9.4%	0.48/22%	-0.12/42%	1.3/1.3%	0.45/5.1%	0.17/2.5%	0.35/8.4%
5/1	162	10/128	0.43/29%	0.14/13%	0.041/8.5%	0.32/3.1%	0.49/9.3%	0.09/24%	0.20/31%	0.28/23%	0.11/73%	1.43/33%
5/2	168	12/133	0.45/38%	0.12/6.8%	0.045/6.8%	0.33/17%	0.49/27%	0.080/14%	0.18/9.5%	0.24/9.5%	0.086/18%	1.3/13%
5/3	154	8/130	0.46/32%	0.14/18%	0.040/7.5%	0.32/11%	0.45/15%	0.072/180%	0.14/46%	0.23/9.9%	0.10/69%	1.6/52%
5/4	179	11/127	0.47/3.6%	0.12/7.6%	0.044/13%	0.31/1.5%	0.45/5.6%	0.078/12%	0.13/34%	0.26/9.3%	0.092/52%	2.0/47%
5/5	161	11/130	0.46/21%	0.09/8.4%	0.043/17%	0.31/7.4%	0.46/28%	0.06/23%	0.21/7.3%	0.31/7.2%	0.073/42%	1.5/12.3%

Table C.1: Original results of experiment I

			Intervals(Second)					Amplitudes(mV)				
Rec.	Vec.	Bt./HR	RR	PR	QRS	QT	QTc	P	R	T	ST	T/R
6/1	251	11/162	0.43/32%	0.11/12%	0.049/2.1%	0.29/4.2%	0.44/8.9%	0.12/9.0%	0.02/37%	0.19/13%	0.09/12%	9.5/42%
6/2	201	14/166	0.36/1.7%	0.10/13%	0.047/1.3%	0.25/4.7%	0.41/7.1%	0.10/13%	0.16/5.2%	0.15/8.9%	0.13/7.8%	0.94/10%
6/3	217	11/157	0.39/5.5%	0.12/10%	0.05/2.4%	0.27/3.2%	0.43/13%	0.15/47%	1.2/4.9%	0.49/17%	0.42/14%	0.40/17%
6/4	231	13/153	0.42/1.2%	0.12/3.2%	0.053/0.89%	0.27/3.7%	0.42/4.2%	0.08/11%	0.03/12%	0.28/6.1%	0.16/7.2%	9.2/13%
7/1	145	14/162	0.37/0.64%	0.14/10.8%	0.057/3.2%	0.26/10%	0.42/12%	0.11/13%	0.53/1.8%	0.39/24%	0.11/8.9%	0.73/27%
7/2	151	15/150	0.33/3.3%	0.12/13%	0.055/2.2%	0.21/6.0%	0.37/7.2%	0.032/19%	0.39/5.2%	0.36/5.9%	0.14/75%	0.92/6.3%
7/3	169	14/171	0.35/12%	0.11/35%	0.052/2.8%	0.24/7.5%	0.69/13.2%	0.047/35%	0.075/27%	0.15/37%	0.07/59%	3.2/39%
8/1	258	11/138	0.44/6.0%	0.14/20%	0.065/5.0%	0.30/3.7%	0.46/4.9%	0.023/30%	0.86/10%	0.38/21%	0.11/114%	0.45/22%
8/2	265	13/152	0.40/2.8%	0.14/7.9%	0.063/10%	0.31/2.7%	0.48/2.8%	0.084/33%	1.1/1.9%	0.38/5.6%	0.15/16%	0.34/17%
8/3	251	12/142	0.42/3.2%	0.15/17%	0.059/3.4%	0.33/3.1%	0.51/4.2%	0.029/12%	1.3/3.5%	0.39/14%	0.12/34%	0.30/15%
8/4	249	12/144	0.42/0.85%	0.14/15%	0.064/6.7%	0.33/2.0%	0.51/2.3%	0.017/13%	0.62/3.9%	0.33/8.0%	0.11/23%	0.53/9.2%
9/1	279	13/154	0.39/0.49%	0.12/11%	0.048/28%	0.24/3.0%	0.38/3.0%	0.17/11%	1.0/1.9%	0.12/20%	0.029/74%	0.12/23%
9/2	243	13/152	0.39/0.58%	0.11/12%	0.048/18%	0.24/3.9%	0.39/4.0%	0.085/33%	1.9/2.2%	0.31/16%	0.19/17%	0.16/19%
9/3	232	11/133	0.45/0.56%	0.11/0.66%	0.052/11%	0.27/1.3%	0.40/1.3%	0.078/9.8%	1.0/1.8%	0.14/14%	0.075/23%	0.13/17%
9/4	239	14/162	0.37/3.9%	0.08/13%	0.054/2.9%	0.23/8.4%	0.38/12%	0.15/27%	0.28/17%	0.25/11%	0.11/23%	0.89/20%
10/1	295	14/171	0.35/2.9%	0.10/5.2%	0.052/2.2%	0.22/7.3%	0.37/9.2%	0.13/23%	0.19/29%	0.21/13%	0.11/32%	1.1/31%
10/2	283	13/`81	0.33/2.2%	0.13/8.2%	0.05/3.1%	0.25/9.2%	0.43/8.2%	0.12/17%	0.25/19%	0.26/12%	0.14/21%	1.0/31%
10/3	230	11/133	0.45/3.1%	0.09/9.2%	0.051/3.3%	0.29/7.9%	0.43/11%	0.10/12%	0.31/7.9%	0.26/21%	0.07/38%	0.83/25%
10/4	267	13/136	0.44/4.9%	0.13/7.3%	0.053/2.1%	0.16/5.5%	0.24/6.3%	0.11/13%	0.27/5.4%	0.33/19%	0.15/29%	1.2/23%
11/1	323	13/162	0.37/0.48%	0.13/1.3%	0.055/0.88%	0.20/15%	0.33/15%	0.28/4.3%	0.74/6.0%	0.21/7.4%	-0.2176471	0.28/13.7%
11/2	264	12/143	0.42/1.1%	0.13/3.1%	0.054/5.3%	0.29/15%	0.45/15%	0.13/28%	0.55/3.9%	0.27/9.7%	0.17/14%	0.46/14%
11/3	251	11/133	0.45/2.2%	0.11/7.4%	0.049/3.1%	0.29/4.3%	0.43/4.7%	0.07/37%	0.47/2.7%	0.31/4.9%	0.19/2.1	0.66/14%
11/4	179	11/141	0.42/0.59%	0.14/9.0%	0.055/1.6%	0.28/3.0%	0.44/3.1%	0.12/70%	0.64/5.6%	0.33/8.8%	0.17/19%	0.51/10%
12/1	82	14/161	0.37/3.6%	0.14/9.4%	0.047/13%	0.27/7.6%	0.45/7.2%	0.037/400%	1.2/6.2%	0.18/34%	0.079/130%	0.15/33%
12/2	93	13/154	0.40/5.2%	0.14/14%	0.057/18%	0.28/4.6%	0.45/3.8%	0.056/270%	1.8/4.0%	0.37/22%	0.19/37%	0.21/21%
12/3	87	12/146	0.41/0.51%	0.15/16%	0.048/11%	0.28/1.2%	0.44/2.1%	0.059/29%	1.3/4.8%	0.16/29%	0.076/46%	0.13/27%
13/1	74	14/165	0.36/0.47%	0.12/1.1%	0.045/1.4%	0.20/0.25%	0.33/0.29%	0.084/8.0%	0.63/2.3%	-0.031/30%	-0.031/47%	-0.05/28.5%
13/2	78	13/140	0.43/24%	0.13/5.7%	0.037/11%	0.26/1.9%	0.40/30%	-0.0048/42%	0.33/6.8%	0.12/3.1%	0.037/59%	0.36/9.2%
13/3	72	13/158	0.38/0.74%	0.14/7.1%	0.034/13%	0.25/6.5%	0.41/6.6%	0.053/53%	0.68/10%	0.13/24%	-0.022/73%	0.21/25%
13/4	71	15/174%	0.34/0.74%	0.13/12%	0.036/10%	0.23/6.1%	0.39/6.3%	0.074/52%	0.69/9.2%	0.14/23%	0.009/221%	0.19/31%
14/1	68	14/158	0.38/0.49%	0.13/5.3%	0041/11%	0.27/2.7%	0.43/2.6%	0.13/19%	1.4/3.1%	0.39/8.1%	0.13/33%	0.29/8.6%
14/2	49	14/159	0.38/1.4%	0.14/13%	0.044/7.4%	0.27/4.2%	0.44/4.4%	0.11/31%	0.77/3.8%	0.34/9.6%	0.13/24%	0.45/9.4%
14/3-4	**Signal Filtering is not possible because the amplifier is saturated by noise.**											

Table C.2: Original results of experiment II

			Intervals(Second)					Amplitudes(mV)				
Rec.	Vec.	Bt./HR	RR	PR	QRS	QT	QTc	P	R	T	ST	T/R
15/1	74	10/127	0.47/0.55%	0.16/6.6%	0.051/2.9%	0.29/2.9%	0.42/3.1%	0.082/33%	1.1/1.0%	-0.19/7.5%	-0.07/16%	-0.16/12%
15/2	103	13/142	0.42/0.72%	0.11/7.2%	0.050/3.2%	0.26/12.3%	0.42/13.2%	0.21/15%	0.67/4.9%	-0.15/12%	0.01/32%	0.22/14%
15/3	84	12/145	0.41/0.80%	0.20/12%	0.041/1.6%	0.22/3.6%	0.34/3.7%	0.16/25%	0.26/5.4%	0.02/19%	0.01/79%	0.03/21%
15/4	97	10/124	0.47/1.5%	0.13/1.4%	0.053/8.2%	0.26/2.1%	0.3/1.8%	0.14/8.2%	0.20/5.7%	0.045/32%	0.02/53%	0.24/35%
15/5	89	11/127	0.47/4.3%	0.15/2.4%	0.050/8.4%	0.28/12%	0.41/12%	0.12/19%	0.60/4.8%	0.052/49%	0.01/85%	0.09/74%
15/6	78	11/129	0.46/2.2%	0.14/1.5%	0.050/1.4%	0.29/2.4%	0.43/3.1%	0.11/9.1%	0.51/4.8%	-0.20/13%	0.01/366%	0.39/15%
15/7	102	11/138	0.43/4.9%	0.15/24%	0.051/2.8%	0.24/0.92%	0.37/2.5%	0.072/115%	0.27/27%	0.17/35%	0.02/57%	0.63/41%
16/1	143	9/121	0.49/1.2%	0.13/6.7%	0.05/9.3%	0.26/2.0%	0.37/2.3%	0.095/15%	0.26/8.6%	0.017/59%	-0.053/49%	0.060/110%
16/2	154	9/108	0.56/1.1%	0.12/7.2%	0.054/9.4%	0.35/3.8%	0.47/4.2%	0.093/13%	0.37/5.2%	0.08/21%	-0.017/54%	0.22/63%
16/3	151	8/105	0.47/2.5%	0.15/27%	0.062/6.1%	0.29/0.46%	0.38/1.5%	0.065/10%	0.59/14%	-0.23/23%	-0.064/96%	-0.34/28%
16/4	154	9/116	0.52/2.7%	0.14/5.7%	0.082/31%	0.28/3.7%	0.38/4.5%	0.086/12%	0.27/9.2%	-0.073/34%	0.005/66%	-0.26/41%
16/5	159	9/111	0.54/3.2%	0.14/2.1%	0.05/30%	0.26/0.26%	0.35/1.6%	0.092/19%	0.13/22%	-0.09/19%	0.02/96%	-0.69/23%
16/6	152	9/108	0.57/5.3%	0.12/13%	0.059/10%	0.28/0.72%	0.38/2.9%	0.10/110%	0.69/13%	-0.10/100%	0.004/290%	-0.14/110%

Table C.3: Original results of experiment III

Subj. No.	Beats	HR	AQRS
1	12 (12-14)	146 (141-159)	94 (87-101)
2	13 (12-13)	149 (140-152)	221 (179-232)
3	7 (6-8)	98 (90-111)	101 (93-112)
4	9 (9-10)	116 (113-130)	148 (137-159)
5	11 (8-12)	130 (127-133)	162 (154-179)

(a) Heart rate and QRS axis

Subj. No.	RR	CvRR	PR	CvPR	QRS	CvQRS	QT	CvQT	QTc	CvQTc
1	0.41 (0.38-0.43)	2.60% (1.6-3.8)	0.13 (0.11-0.13)	6.70% (2.0-20)	0.048 (0.047-0.057)	3.10% (1.7-7.8)	0.29 (0.28-0.31)	4.80% (2.7-6.6)	0.45 (0.44-0.47)	4.50% (2.2-6.3)
2	0.4 (0.39-0.43)	1.00% (0.35-2.3)	0.14 (0.14-0.17)	6.50% (5.7-9.3)	0.055 (0.05-0.06)	2.00% (1.3-2.9)	0.28 (0.27-0.38)	2.10% (0.71-3.1)	0.43 (0.42-0.44)	2.10% (1.3-3.1)
3	0.61 (0.54-0.67)	2.10% (1.1-3.5)	0.14 (0.12-0.19)	14% (13-33)	0.06 (0.058-0.061)	35% (2.0-39)	0.32 (0.32-0.33)	0.60% (0.37-1.0)	0.41 (0.39-0.45)	2.33% (0.93-16)
4	0.52 (0.45-0.54)	4.90% (2.7-25)	0.17 (0.15-0.22)	5% (2.2-25)	0.054 (0.052-0.056)	5.90% (4.2-38)	0.35 (0.34-0.37)	3.90% (0.74-14)	0.5 (0.48-0.51)	3.40% (1.6-22)
5	0.46 (0.43-0.47)	29% (3.6-38)	0.12 (0.09-0.14)	8.40% (6.8-18)	0.043 (0.041-0.045)	8.50% (6.8-17)	0.32 (0.31-0.33)	7.40% (1.5-17)	0.46 (0.45-0.49)	15% (5.6-28)

(b) Interval measurements

Subj. No.	P	CvP	R	CvR	T	CvT	ST	CvST	T/R	CvT/R
1	0.06 (0.05-0.10)	31% (22-160)	0.9 (-0.81-0.95)	6.90% (3.5-9.28)	0.21 (-0.15-0.23)	27% (22-43.2)	0.088 (0.01-0.11)	74% (24-120)	0.24 (-0.59-0.34)	27% (14-44)
2	0.1 (0.08-0.12)	13% (8.3-21)	0.28 (-0.24-0.35)	6.50% (5.6-13)	0.31 (0.24-0.33)	6.60% (4.7-8.9)	0.17 (0.13-0.18)	12% (9.0-22)	1 (0.79-1.18)	16% (9.2-47)
3	0.058 (0.0033-0.07)	108% (60-200)	0.32 (-0.26-0.34)	15.90% (4.5-32)	0.15 (-0.068-0.18)	27% (16-42)	0.045 (0.034-0.067)	63% (60-140)	0.46 (0.21-0.62)	34% (32-53)
4	-0.7 (-0.12 - -0.05)	42% (16-210)	1.05 (0.90-1.3)	1.30% (0.54-36)	0.45 (-0.43-0.47)	5.10% (22-8.9)	0.17 (0.13-0.18)	5.20% (3.8-37)	0.47 (0.35-0.48)	8.40% (4.9-10.0)
5	0.078 (-0.06 -0.09)	23% (12-180)	0.18 (-0.13-0.21)	31% (7.3-46)	0.26 (0.23-0.31)	9.50% (7.2-23)	0.092 (0.073-0.11)	52% (18-73)	1.5 (1.3-2.0)	33% (12.3-52)

(c) Amplitude measurements

Table C.4: Statistical results of experiment I

Subj. No.	Beats	HR	AQRS
6	13	143	241
	(11-14)	(133-162)	(232-279)
7	14	161	75
	(13-15)	(140-174)	(71-78)
8	13	154	87
	(12-14)	(146-161)	(82-93)

(a) Heart rate and QRS axis

Subj. No.	CGA	CRIB	RR	CvRR	PR	CvPR	QRS	CvQRS	QT	CvQT	QTc	CvQTc
6	25+4	10	0.39	0.57%	0.11	11.50%	0.05	14.50%	0.235	3.45%	0.385	2.15%
			(0.37-0.45)	(0.49-3.9)	(0.08-0.12)	(0.66-13)	(0.048-0.054)	(2.9-28)	(0.23-0.27)	(1.3-8.4)	(0.38-0.40)	(1.3-12)
7	26+7	4	0.37	0.74%	0.13	6.40%	0.0365	10.50%	0.24	4.00%	0.395	6.45%
			(0.34-0.43)	(0.47-24)	(0.12-0.14)	(1.1-12)	(0.034-0.045)	(1.4-13)	(0.20-0.26)	(0.25-6.5)	(0.33-0.40)	(0.29-30)
8	36+1	3	0.4	3.60%	0.14	14%	0.048	13%	0.28	4.60%	0.45	3.80%
			(0.37-0.41)	(0.51-5.2)	(0.14-0.15)	(9.4-16)	(0.047-0.057)	(11-18)	(0.27-0.28)	(1.2-7.6)	(0.44-0.45)	(2.1-7.2)

(b) Interval measurements

Subj. No.	CGA	CRIB	P	CvP	R	CvR	T	CvT	ST	CvST	T/R	CvT/R
6	25+4	10	0.12	19%	1	2.05%	0.2	15%	0.1	23%	0.15	19.50%
			(0.078-0.17)	(9.8-33)	(0.28-1.9)	(1.8-17)	(0.14-0.31)	(14-20)	(0.0029-0.19)	(17-74)	(0.12-0.89)	(0.12-0.89)
7	26+7	4	0.07	47%	0.66	8.00%	0.125	23.50%	-0.01	66%	0.2	27%
			(-0.0048-0.084)	(8-53)	(0.33-0.69)	(2.3-10)	(-0.031-0.14)	(3.1-30)	(-0.031-0.037)	(47-221)	(-0.05-0.36)	(9.2-31)
8	36+1	3	0.056	270%	1.3	4.80%	0.18	29%	0.079	46%	0.15	27%
			(0.037-0.059)	(29-400)	(1.2-1.8)	(4.0-6.2)	(0.16-0.37)	(22-34)	(0.076-0.19)	(37-130)	(0.13-0.21)	(21-33)

(c) Amplitude measurements

Table C.5: Statistical results of experiment II, group A

Subj. No.	Beats	HR	AQRS
9	12	143	254.5
	(11-13)	(138-152)	(249-265)
10	14	162	151
	(14-15)	(150-171)	(145-169)
11	14	159	58.5
	(-14)	(158-159)	(49-68)

(a) Heart rate and QRS axis

Subj. No.	CGA	CRIB	RR	CvRR	PR	CvPR	QRS	CvQRS	QT	CvQT	QTc	CvQTc
9	Term+13/7	8	0.42	3.00%	0.14	16.00%	0.0635	5.85%	0.32	2.90%	0.5	3.50%
			(0.40-0.44)	(0.85-6.0)	(0.14-0.15)	(7.9-20)	(0.059-0.065)	(3.4-10)	(0.30-0.33)	(2.0-3.7)	(0.46-0.51)	(2.3-4.9)
10	Term+8/52	4	0.35	3.30%	0.12	13.00%	0.055	2.80%	0.24	7.50%	0.42	12.00%
			(0.33-0.37)	(0.64-12)	(0.11-0.14)	(0.8-35)	(0.052-0.057)	(2.2-3.2)	(0.21-0.26)	(6.0-10)	(0.37-0.69)	(7.2-13.2)
11	29+5/40	3	0.38	0.95%	0.135	9.15%	0.0425	9.20%	0.27	3.45%	0.435	3.50%
			(0.38)	(0.49-1.4)	(0.13-0.14)	(5.3-13)	(0.041-0.044)	(7.4-11)	(0.27)	(2.6-4.4)	(0.43-0.44)	(2.6-4.4)

(b) Interval measurements

Subj. No.	CGA	CRIB	P	CvP	R	CvR	T	CvT	ST	CvST	T/R	CvT/R
9	Term+13/7	8	0.026	21.5%	0.6	3.70%	0.38	11%	0.115	29%	0.395	16.00%
			(0.017-0.084)	(12-30)	(0.062-1.3)	(1.9-10)	(0.33-0.39)	(5.6-21)	(0.11-0.15)	(16-114)	(0.30-0.53)	(9.2-22)
10	Term+8/52	4	0.047	19%	0.39	5.20%	0.36	24.00%	0.11	59%	0.92	27%
			(0.032-0.11)	(13-35)	(0.075-0.53)	(1.8-27)	(0.15-0.39)	(5.9-37)	(0.07-0.14)	(8.9-75)	(0.73-3.2)	(6.3-39)
11	29+5/40	3	0.12	25%	1.08	3.45%	0.365	8.85%	0.13	29%	0.37	9.15%
			(0.11-0.13)	(19-31)	(0.77-1.4)	(3.1-3.8)	(0.34-0.39)	(8.1-9.6)	(0.13)	(24-33)	(0.29-0.45)	(8.6-9.5)

(c) Amplitude measurements

Table C.6: Statistical results of experiment II, group B

Subj. No.	Beats	HR	AQRS
12	12	142	257.5
	(11-13)	(133-162)	(179-323)
13	12	154	275
	(11-13)	(133-181)	(230-295)
14	12	160	224
	(11-14)	(153-166)	(201-251)

(a) Heart rate and QRS axis

Subj. No.	CGA	CRIB	RR	CvRR	PR	CvPR	QRS	CvQRS	QT	CvQT	QTc	CvQTc
12	32+4	0	0.42	0.35%	0.13	5.25%	0.0545	2.35%	0.285	9.65%	0.435	9.85%
			(0.37-0.45)	(2.2-4.9)	(0.11-0.14)	(1.3-9.0)	(0.049-0.055)	(0.88-5.3)	(0.2-0.9)	(3-15)	(0.33-0.45)	(3.1-15)
13	32+4	0	0.4	0.85%	0.115	7.75%	0.0515	2.65%	0.24	7.60%	0.4	8.70%
			(0.37-0.45)	(0.48-2.2)	(0.09-0.13)	(5.2-9.2)	(0.050-0.053)	(2.1-3.3)	(0.16-0.29)	(5.5-9.2)	(0.24-0.43)	(6.3-11)
14	33+2	0	0.41	3.60%	0.115	11.00%	0.0495	2.25%	0.27	3.95%	0.425	8.00%
			(0.36-0.43)	(1.2-32)	(0.10-0.12)	(3.2-13)	(0.047-0.053)	(0.089-2.4)	(0.25-0.29)	(3.2-4.7)	(0.41-0.44)	(4.2-13)

(b) Interval measurements

Subj. No.	CGA	CRIB	P	CvP	R	CvR	T	CvT	ST	CvST	T/R	CvT/R
12	32+4	0	0.125	32.50%	0.6	4.75%	0.29	8.10%	0.17	14.00%	0.49	13.85%
			(0.07-0.28)	(4.3-70)	(0.47-0.74)	(2.7-6.0)	(0.21-0.33)	(4.9-9.7)	(0.17-0.19)	(2.1-19)	(0.28-0.66)	(10-14)
13	32+4	0	0.115	15.00%	0.26	13.45%	0.26	16.00%	0.13	30.50%	1.05	28.00%
			(0.10-0.13)	(12-23)	(0.19-0.31)	(5.4-29)	(0.21-0.33)	(12-21)	(0.07-0.15)	(21-38)	(0.82-1.2)	(23-31)
14	33+2	0	0.11	12.00%	0.095	8.60%	0.24	10.90%	0.145	8.90%	5.07	15.00%
			(0.08-0.15)	(9-47)	(0.02-1.2)	(4.9-37)	(0.15-0.49)	(6.1-17)	(0.09-0.42)	(7.2-14)	(0.4-9.5)	(10-42)

(c) Amplitude measurements

Table C.7: Statistical results of experiment II, group C

Subj. No.	Beats	HR	AQRS
15	11	129	89
	(10-13)	(124-145)	(74-103)
16	9	110	153
	(8-9)	(105-121)	(143-159)

(a) Heart rate and QRS axis

Subj. No.	CRIB	RR	CvRR	PR	CvPR	QRS	CvQRS	QT	CvQT	QTc	CvQTc
15	1	0.46	1.50%	0.15	6.60%	0.5	2.90%	0.26	2.90%	0.41	3.10%
		(0.41-0.47)	(0.55-4.9)	(0.11-0.16)	(1.4-24)	(0.41-0.53)	(1.4-8.4)	(0.22-0.29)	(0.92-12.3)	(0.30-0.43)	1.8-13.2
16	3	0.53	2.60%	0.135	6.95%	0.056	9.70%	0.28	1.36%	0.38	2.60%
		(0.49-0.57)	(1.1-5.3)	(0.12-0.15)	(2.1-27)	(0.05-0.082)	(6.1-30)	(0.26-0.35)	(0.26-3.8)	(0.35-0.47)	(1.5-4.5)

(b) Interval measurements

Subj. No.	CRIB	P	CvP	R	CvR	T	CvT	ST	CvST	T/R	CvT/R
15	1	0.12	15%	0.51	4.90%	0.02	19%	0.01	57%	0.22	21%
		(0.072-0.21)	(8.2-115)	(0.2-1.1)	(1-27)	(-0.20-0.17)	(7.5-49)	(-0.07-0.02)	(16-336)	(-0.07-0.63)	(12-74)
16	3	0.0925	14%	0.32	11.10%	-0.0815	28.50%	-0.0065	81%	-0.2	52%
		(0.065-0.10)	(10-110)	(0.13-0.69)	(5.2-22)	(-0.23-0.08)	(19-100)	(-0.064-0.02)	(49-290)	(-0.69-0.22)	(23-110)

(c) Amplitude measurements

Table C.8: Statistical results of experiment III

Appendix D

Information for the neonatal ECG analyser

This appendix encloses some technical details of the integrated neonatal ECG analyser, including information regarding the bio-amplifier, the format of data files, and the system operating procedure.

D.1 Technical information for the BMA-200 bio-amplifier

The BMA-200 bio-amplifier [107], used in the acquisition of neonatal ECG signals, is a battery powered AC/DC differential pre-amplifier for the low-noise recording of muscle, nerve, ECG, or other biopotentials. The wide gain range of the BMA-200 allows its use as a primary amplifier whose output can be fed directly to tape or chart recorders, or as in this case, an analogue-to-digital converter (PCI-6025E, National Instruments).

The band-pass filters contained in the BMA-200 are of the Butterworth type, providing the flattest response and minimal peaking. The slope of the filters is -12dB/octave. These six-position high and low pass filters have a sharp

roll-off to effectively limit the signal to the desired frequency bandwidth. The frequency response of the BMA-200 covers the range DC-50kHz. A built-in audio monitor is also provided to allow instant verification of the signals being recorded.

As positive and negative supply voltages may be present on the input connector for the purpose of powering external devices, considering the absolute safety of the neonates, in this application the BMA-200 was used with an ISO-Z head-stage. This head-stage guarantees that no current will flow to the subject, and complies with UL544 safe current limits.

The specification for the BMA-200 is as follows:

Input type:	differential instrument amplifier
Input impedance:	>10,000 megohms
Input connector:	7-pin Amphenol 703-91T-3475-001
Noise, wideband, referred to input:	<7 μV P-P, < 3 μV RMS
Common mode rejection:	>100dB @ 60Hz
Input voltage range:	$\pm$1V
Input offset adjustment ranges:	$\pm$2, $\pm$20, $\pm$200 mV
Bandpass filters:	Butterworth, -12 dB/octave
Low frequency filter:	DC, 1, 3, 10, 30, 100 Hz
High frequency filter:	0.1, 1, 3, 10, 30, 50 kHz
Output range:	$\pm$6V @ 10 mA
Output connector:	BNC jack
Calibrator:	1 mV square wave, 10 Hz
Stim/Record control input:	TTL negative or switch closure
Headphone jack:	3.5 mm stereo mini-phone jack
Battery life:	> 30 hours between charges
Battery charger/adapter:	20 VDC @ 200 mA

Dimensions: 6W × 1.5H × 8D in.

Weight: 3.5 lbs

D.2 File formats

Several file formats are used in the system, including the subject information file, ECG record file, processing result file and exported spreadsheet file. Except the spreadsheet file, all other files for a subject should be stored in one sub-directory.

The details of these formats are given as follows.

D.2.1 Subject information file

These files (*.rcd) provide the clinic information for a subject under trial, including

Line Number	Content	Identifier
1	integer (version of information file)	:Version
2	string (name of the subject)	
3	boolean (0 for male, 1 for female)	:Gender
4	integer (unit number)	:Unit
5	integer (date of birth)	:DOB
6	single (birth weight)	:Weight
7	integer (gestation weeks)	:Weeks
8	integer (gestation days)	:Days
9	string (comments)	

D.2.2 ECG record file

These files (*.ecg) contain the acquired ecg data, as follows

Line Number	Content	Identifier
1	integer (version of record file)	:Version
2	string (date of record)	:DOR
3	integer (record number)	:Record
4	integer (lead number)	:Lead
5	blank	
6	integer (first sampled data)	
⋮		
7006	integer (last sampled data)	

D.2.3 Processing result file

These files (*.rst) archive the processing result of one subject, consists of a number of identically formatted lines (depending on the number of records from the subject). Each line contains

column number	content
1	integer (record number)
2	integer (lead number)
3	integer (hear rate)
4	integer (RR interval)
5	integer (PR interval)
6	integer (QRS interval)
7	integer (QT interval)
8	integer (QTc)
9	integer (P amplitude)
10	integer (Q amplitude)
11	integer (R amplitude)
12	integer (S amplitude)
13	integer (ST amplitude)
14	integer (T amplitude)

15 integer (T/R)

16 integer (Axis)

D.2.4 Exported spreadsheet

The exported spreadsheet files contain comma-separated data that can be read by Microsoft Excel. The contents in each column are the same as in the processing result file.

D.3 Operating procedures for the system

The operating procedures for data acquisition, data processing and storage, and result export are given in Figure D.1.

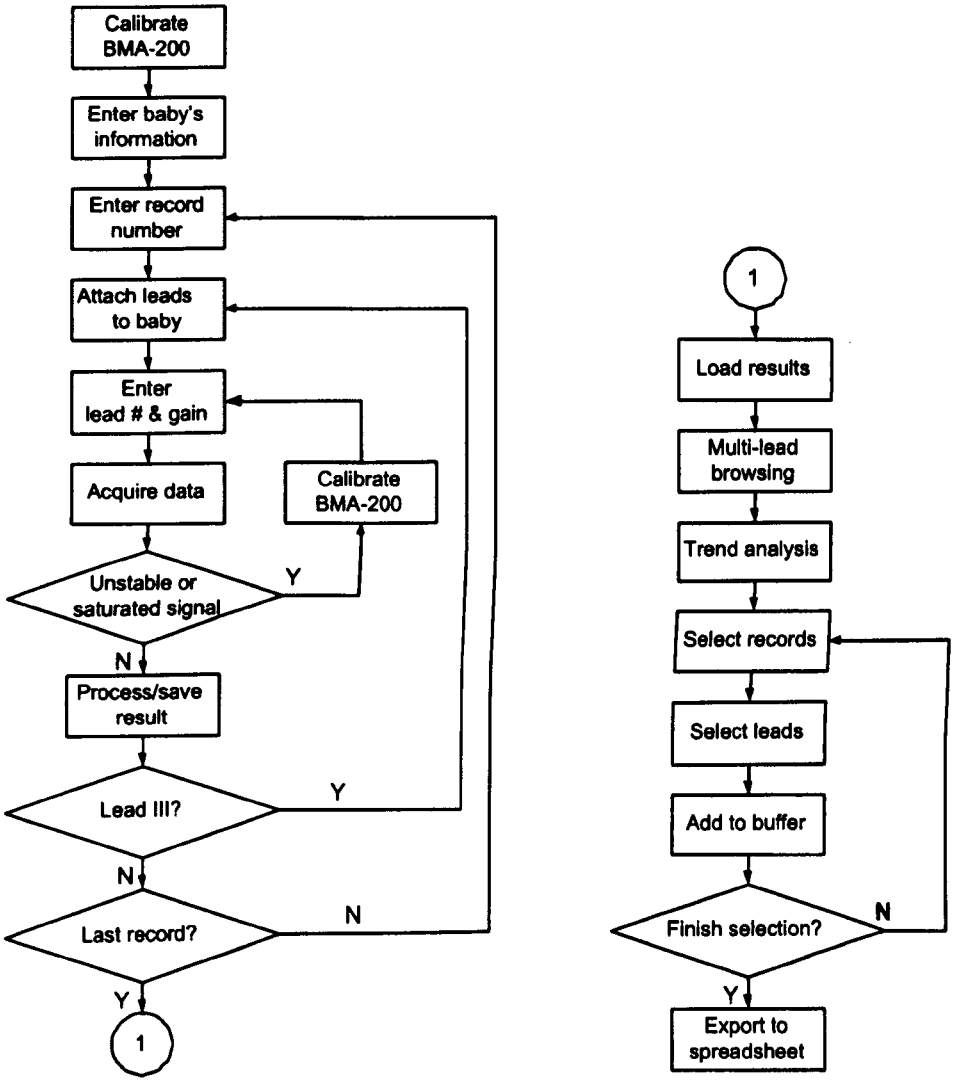

Figure D.1: System operating procedures

References

[1] C. H. Chu and E. J. Delp. Impulsive noise suppression and background normalisation of electrocardiogram signals using morphological operators. *IEEE Transactions on Biomedical Enigneering*, 36:262–273, 1989.

[2] P. T. Jackway. *Morphological scale-space with application to 3d object recognition.* PhD thesis, Queensland University of Technology, 1994.

[3] R. G. Baraniuk. Beyond time-frequency analysis: Energy densities in one and many dimensions. In *Proceedings of 1994 International Conference on Acoustic, Speech and Signal Processing (Los Alamitos, CA, Adelaide, Australia), IEEE Signal Processing Society*, pages III:357–360, 1994.

[4] G. Matheron. *Random Sets and Integral Geometry.* John Wiley & Sons, New York, 1975.

[5] J. Serra. *Image Analysis and Mathematical Morphology.* Academic Press, London, 1982.

[6] J. Serra, editor. *Image Analysis and Mathematical Morphology. II: Theoretical Advances.* Academic Press, London, 1988.

[7] R. van den Boomgaard. *Mathematical Morphology: Extensions towards computer vision.* PhD thesis, University of Amsterdam, 1992.

[8] D. J. Zhang and Q. H. Wu. Identification of magnetizing inrush current based on wavelet transform. Technical report, Department of Electrical Engineering and Electronics, The University of Liverpool, Dec. 2000.

[9] J. E. Waldron and S. E. Stanley. Design considerations for a new solid state transformer differential relay with harmonic restraint. In *Western Protective Relay Conference*, 1978.

[10] K. Karsai, D. Kerenyi, and L. Kiss. *Large Power Transformers.* Elsevier, New York, 1987.

[11] P. Liu, O. P. Malik, C. Chen, G. S. Hope, and Y. Guo. Improved operation of differential protection of power transformers for internal faults. *IEEE Transactions on Power Delivery*, 7 (4):1912–1919, 1992.

[12] Z. Q. Bo, G. Weller, and T. Lomas. A new technique for transformer protection based on transient detection. *IEEE Transactions on Power Delivery*, 15 (3):870–875, Jul. 2000.

[13] Z. Moravej, D. N. Vishwakarma, and S. P. Singh. ANN-based protection scheme for power transformer. *Electric Machines and Power Systems*, 28:875–884, Dec. 1999.

[14] J. Pihler, B. Grcar, and D. Dolinar. Improved operation of power transformer protection using artifical neural network. *IEEE Transactions on Power Delivery*, 12 (3):1128–1136, Jul. 1997.

[15] E. C. Mallard, C. E. Williams, B. M. Johnston, M. I. Gunnings, S. Davis, and P. D. Gluckman. Repeated episodes of umbilical cord occlusion in fetal sheep lead to preferential damage to the striatum and sensitize the heart to futher insults. *Pediatric Research*, 37 (6):707–713, 1995.

[16] O. Pahlm and L. Sornmo. Software QRS detection in ambulatory monitoring – a review. *Medical and Biological Engineering and Computing*, 22:289–297, 1984.

[17] G. B. Moody, W. K. Muldrow, and R. G. Mark. A noise stress test for arrhythmia detectors. *Computers in Cardiology*, 11:381–384, 1984.

[18] P. E. Trahanias. An approach to QRS complex detection using mathematical morphology. *IEEE Transactions on Biomedical Enigneering*, 40:201–205, 1993.

[19] D. Schonfeld. Morphological processing of medical images: An introduction. In *Proceedings of IEEE International Symposium on Circuits and Systems*, volume 1, pages 746–749, 1991.

[20] J. Serra and P. Soille. *Mathematical morphology and its applications to image processing.* Kluwer Academic Publishers, The Netherlands, 1994.

[21] H. Minkovski. Volumen und oberflache. *Math. Annalen*, 57:447–495, 1903.

[22] H. Hadwiger. *Vorlesungen uber inhalt, oberflache und isoperimetrie.* Springer–Verlag, Berlin, 1957.

[23] J. Serra. Introduction to mathematical morphology. *Computer Vision, Graphics and Image Processing*, 35:283–305, 1986.

[24] P. Maragos. A representation theory for morphological image and signal processing. *IEEE Transactions on Pattern Analysis and Machine Intelligence*, 11:586–599, 1989.

[25] H. J. A. M. Heijmans. *Morphological Image Operators.* Academic Press, Boston, 1994.

[26] S. J. Ko, A. Morales, and K. H. Lee. Fast recursive algorithms for morphological operators based on the basis matrix representation. *IEEE Transactions on Image Processing*, 5 (6):1073–1077, 1996.

[27] M. H. Sedaaghi and Q. H. Wu. Real-time implementation of grey-scale morphological operators. *Electronics Letters*, 33 (21):1761–1763, 1997.

[28] M. H. Sedaaghi and Q. H. Wu. A reliable hardware for grey-scale morphological filtering. In *Proceedings of the First International Symposium on Communication Systems and Digital Signal Processing*, pages 147–150, Sheffield Hallam University, Sheffield, 1998.

[29] R. M. Haralick, S. R. Sternberg, and X. Zhuang. Image analysis using mathematical morphology. *IEEE Transactions on Pattern Analysis and Machine Intelligence*, 9:532–550, 1987.

[30] M. J. E. Golay. Hexagonal parallel pattern transformations. *IEEE Transactions on Computers*, 18:733–740, 1969.

[31] D. Graham and P. Norgren. The Diff3 analyzer: A parallel/serial Golay image processor. In M. Onoe, K. Preston, and A. Rosenfeld, editors, *Real Time Medical Image Processing*, pages 163–182. Plenum Press, London, 1980.

[32] B. Kruse. *Design and Implementation of a Picture Processor.* PhD thesis, University of Linkoeping, Linkoeping, Sweden, 1977.

[33] J. C. Klein, L. Cahn, C. Ray, and G. H. Urban. The texture analyzer. *Journal of Microscopy*, 95:349–356, 1977.

[34] M. Duff. Parallel processors for digital image processing. In P. Stucki, editor, *Advances in digital image processing*, pages 265–279. Plentum, New York, 1979.

[35] F. Gerritsen and L. G. Aardema. Design and use of DIP-1: A fast flexible and dynamically microprogrammable image processor. *Pattern Recognition*, 14:319–330, 1981.

[36] A. Zarandy, A. Stoffels, T. Roska, and L. O. Chua. Implementation of binary and gray-scale mathematical morphology on the CNN universal machine. *IEEE Transactions on Circuits and SystemsI: Fundamental Theory and Applications*, 45 (2):163–168, 1998.

[37] J. Serra. Morphological filtering: An overview. *Signal Processing*, 38:3–11, 1994.

[38] Q. H. Wu, P. Sun, and D. J. Zhang. Identification of transformer inrush current by morphological signal decomposition. In *Proceeding of the 2001 International Conference on Power Systems*, pages 527–530, Wuhan, China, Sept. 2001. *CIGRÉ*.

[39] Q. H. Wu, P. Sun, and D. J. Zhang. Identification of transformer inrush current by morphological signal decomposition. Research report, Department of Electrical Engineering and Electronics, The University of Liverpool; T&D Protection and Control Ltd, Alstom, 2000.

[40] P. Sun, J.F. Zhang, Q.H. Wu, and S. Potts. Morphological identification of transformer magnetising inrush current. *Electronics Letters*, 38 (9):437–438, 2002.

[41] P. Sun, Q. H. Wu, A. M. Weindling, and J. Wang. Morphological operators for removal of baseline wander in neonatal ECGs. In *InstMC Mini-symposium, Proceeding of the UKACC International Conference on Control 2000*, Cambridge, UK, Sept. 2000. IEE.

[42] P. Sun, Q. H. Wu, A. M. Weindling, A. Finkelstein, and K. Ibrahim. An improved morphological approach to background normalisation of ECG signals. *IEEE Transactions on Biomedical Engineering*, To appear.

[43] E. R. Dougherty and C. R. Giardina. *Image Processing - Continuous to Discrete.* Prentice - Hall, Englewood Cliffs, NJ, 1987.

[44] C. R. Giardina and E. R. Dougherty. *Morphological Methods in Image and Signal Processing.* Prentice - Hall, Englewood Cliffs, NJ, 1988.

[45] ALSTOM T&D Control Ltd. *Type MBCH Biased Differential Relay*, 1999. Service Manual.

[46] M. Gomez-Morante and D. W. Nicoletti. A wavelet-based differential transformer protection. *IEEE Transactions on Power Delivery*, 14 (4):1351–1358, Oct. 1999.

[47] ALSTOM T&D Control Ltd. *Protective Relays*, 1995. Application Guide.

[48] A. Kulidjian, B. Kasztenny, and B. Campbell. New magnetizing inrush restraining algorithm for power transformer protection. In *Proceedings of the 7th International Conference on Developments in Power System Protection*, pages 181–184, Amsterdam, Netherlands, Apr. 09–12, 2001.

[49] B. Kasztenny and A. Kulidjian. An improved transformer inrush restraint algorithm increases security while maintaining fault response performance. In *5rd Annual Conference for Protective Relay Engineers*, College Station, Texas, USA, 11–13 Apr 2000.

[50] S. H. Horowitz and A. G. Phadke. *Power System Relaying.* Wiley & Sons, New York, 1992.

[51] B. Kasztenny, E. Rosolowski, M. M. Saha, and B. Hillstrom. A comparative analysis of protection principles for multi-citeria power transformer relaying. In *Proceedings of the 12th Power Systems Computation Conference*, pages 107–113, Dresden, Germany, Aug. 19–23, 1996.

[52] B. Kasztenny and M. Kezunovic. Improved power transformer protection using numerical relays. *IEEE Computer Applications in Power*, 11 (4):39–45, 1998.

[53] L. F. Blume. *Transformer Enigneering.* Wiley & Sons, New York, 1951.

[54] T. Giuliante and G. Clough. Advances in the design of differential protection of power transformers. In *Texas A&M University Conference for Protective Relay Engineers*, College Station, Texas, USA, 1995.

[55] W. A. Elmore. *Protective Relaying. Theory and Applications.* Marcel Dekker, New York, 1994.

[56] I. Pitas and A. N. Venetsanopoulos. Morphological shape decomposition. *IEEE Transactions on Pattern Analysis and Machine Intelligence*, 12 (1):38–45, Jan. 1990.

[57] D. Coltuc and I. Pitas. Morphological residual representations of signals. *IEEE Transactions on Image Processing*, 5 (11):1569–1572, Nov. 1996.

[58] A.M. Gole, O.B. Nayak, T.S. Sidhu, and M.S. Sachdev. A graphical electromagnetic simulation laboratory for power systems engineering programs. *IEEE Transactions on Power Systems*, 11 (2):599–606, 1996.

[59] P. Rolfe. Neonatal critical care monitoring. *Journal of Medical Engineering and Technology*, 10 (3):115–120, 1986.

[60] I. Barberi, M. P. Calabro, S. Cordaro, E. Gitto, A. Sottile, D. Prudente, G. Bertuccio, and S. Consolo. Myocardial ischaemia in neonates with perinatal asphyxia. *Neonatology*, 158:742–747, 1999.

[61] J. L. Emery. The neonatal electrocardiogram and unexpected death in infancy. *British Medical Journal*, 2 (6090):833, Sep. 1977.

[62] J. A. Zupancic, J. K. Triedman, M. Alexander, E. P. Walsh, D. K. Richardson, and C. I. Berul. Cost-effectiveness and implications of newborn screening for prolongation of QT interval for the prevention of sudden infant death syndrome. *Journal of Pediatrics*, 136 (4):481–489, 2000.

[63] R. J. Martin, M. J. Miller, and S. Redline. Screening for SIDS: A neonatal perspective. *Pediatrics*, 103:812–813, 1999.

[64] P. J. Schwartz, M. Stramba-Badiale, A. Segantini, P. Austoni, G. Bosi, R. Giorgetti, F. Grancini, E. D. Marni, F. Perticone, D. Rosti, and P. Salice. Prolongation of the QT interval and the sudden infant death syndrome. *New England Journal of Medicine*, 338 (24):1709–1714, 1998.

[65] W. F. Ganong. *Review of Medical Physiology.* Appleton and Lange, London, 1995.

[66] M. L. Ahlstrom and W. J. Tompkins. Digital filters for real-time ECG signal processing using microprocessors. *IEEE Transactions on Biomedical Enigneering*, 32:708–713, 1985.

[67] J. A. van Alste and T. S. Schilder. Removal of baseline wander and power-line interference from the ECG by an efficient FIR filter with a reduced number of taps. *IEEE Transactions on Biomedical Enigneering*, 32 (12):1052–1060, 1985.

[68] N. C. Gallagher and G. L. Wise. A theoretical analysis of the properties of median filters. *IEEE Transactions on Acoustics, Speech and Signal Processing*, 29:1136–1141, 1981.

[69] P. D. Wendt, E. J. Coyle, and N. C. Callagher. Stack filters. *IEEE Transactions on Acoustics, Speech and Signal Processing*, 34:898–911, 1986.

[70] S. R. Sternberg. Parallel architectures of image processing. *Real-time Parallel Computing and Image Analysis*, pages 347–359, 1981.

[71] M. H. Sedaaghi. Direct implementation of open-closing in morphological filtering. *Electronics Letters*, 33 (3):198–199, 1997.

[72] R. M. Freedom, L. N. Benson, and J. F. Smallhorn. *Neonatal Heart Disease.* Springer–Verlag, London, 1992.

[73] J. A. Hubsher. The electrocardiogram of the premature infant. *American Heart Journal*, 63 (4):467–475, 1961.

[74] H. C. Bazett. An analysis of the time relationship of the electrocardiogram. *Heart*, 7:353, 1920.

[75] P. J. Schwartz, M. Montemerlo, M. Facchini, P. Salice, D. Rosti, G. Poggio, and R. Giorgetti. The QT interval throughout the first six months of life: A prospective study. *Circulation*, 66:496–501, 1982.

[76] L. Edenbrandt, B. Devine, and P. W. Macfarlane. Classification of electrocardiographic ST-T segments-human exper vs artificial neural network. *European Heart Journal*, 14:464–468, 1993.

[77] F. Gritzali, G. Frangakis, and G. Papakonstantinou. Detection of the P and T waves in an ECG. *Computers and Biomedical Research*, 22:83–91, 1989.

[78] M. H. Sedaaghi. *Morphological Filtering in Signal/Image Processing.* PhD thesis, Department of Electrical Engineering and Electronics, The University of Liverpool, 1998.

[79] B. Reddy, P. Elko, D. Christenson, and G. Rowlandson. Detection of complex atrial arrhythmias in resting ECG. In *Proceedings of Computers in Cardiology, IEEE Computer Society*, pages 777–780, Bethesda, Maryland, 1994.

[80] B. Reddy, P. Elko, D. Christenson, and G. Rowlandson. Detection of P-waves in resting ECG: A preliminary study. In *Proceedings: Computers in Cardiology Conference, IEEE Computer Society*, pages 87–90, Los Alamitos, California, 1992.

[81] V. X. Afonso, W. J. Tompkins, T. Q. Nguyen, K. Michler, and S. Luo. Comparing stree ECG enhancement algorithms. *IEEE Engineering in Medicine and Biology Magazine*, 15 (3):37–44, 1996.

[82] J. V. Levert, A. C. Maan, C. A. Swenne, M. Bootsma, and A. V. G. Bruschke. The relation between QT intervals and heart rate in young healthy males using an incremental head-up tilt protocol. *Computers in Cardiology*, pages 285–288, Sept. 1996.

[83] J. S. M. Sarma, R. J. Sarma, M. Bilitch, D. Katz, and S. L. Song. An exponential formula for heart rate dependence of QT interval during exercise and cardiac pacing in humans: reevaluation of Bazett's formula. *American Journal of Cardiology*, 54:103–108, 1984.

[84] C. Funck-Brentano and P. Jaillon. Rate-corrected QT interval: techniques and limitations. *American Journal of Cardiology*, 72:17B–22B, 1993.

[85] O. Pahlm and L. Sornmo. Data processing of exercise ECGs. *IEEE Transactions on Biomedical Enigneering*, 34 (2):158–165, 1987.

[86] J. A. Van Alste, W. Van Eck, and O. E. Herrman. ECG baseline wander reduction using linear phase filters. *Computers and Biomedical Research*, 19:417–427, 1986.

[87] D. Wang and D. C. He. Fast implementation of 1-D grayscale morphological filters. *IEEE Transactions on Circuits and SystemsII: Analog and Digital Signal Processing*, 41 (9):634–636, 1994.

[88] A. G. Favret and A. A. Marchetti. Fetal electrocardiograph waveforms from abdominal wall recordings. *American Journal of Obstetrics and Gynecology*, 27:355–362, 1966.

[89] B. A. Goddard. A clinical foetal electrocardiograph. *Medical and Biological Engineering*, 4:159–167, 1966.

[90] W. J. H. Meijer and P. Bergveld. The simulation of the abdominal MECG. *IEEE Transactions on Biomedical Enigneering*, 28:354–357, 1981.

[91] A. Khamene and S. Negahdaripour. A new method for the extraction of fetal ECG from the composite abdominal signal. *IEEE Transactions on Biomedical Enigneering*, 47:507–516, 2000.

[92] S. Abound, A. Alaluf, S. Einav, and D. Sadeh. Real time abdominal fetal ECG recording using hardware correlator. *Computers in Biology and Medicine*, 22:325–335, 1992.

[93] J. H. V. Bemmel. Detection of weak fetal electrocardiograms by autocorrelation and cross-correlation of envelopes. *IEEE Transactions on Biomedical Enigneering*, 15:17–23, 1968.

[94] P. Bergveld, A. J. Kolling, and J. H. Peuscher. Real time fetal ECG recording. *IEEE Transactions on Biomedical Enigneering*, 33:505–509, 1986.

[95] E. R. Ferrara and B.Widrow. Fetal electrocardiogram enhancement by time-sequenced adaptive filtering. *IEEE Transactions on Biomedical Enigneering*, 29:458–460, 1982.

[96] J. Vanderschoot, D. Callaerts, W. Sansen, J. Vandewalle, G. Vantrappen, and J. Janssens. Two methods for optimal MECG elimination and FECG detection from skin electrode signals. *IEEE Transactions on Biomedical Enigneering*, 34:233–243, 1987.

[97] S. Mallat and W. L. Hwang. Singularity detection and processing with wavelets. *IEEE Transactions on Information Theory*, 38:617–643, 1992.

[98] S. Mallat and S. Zhong. Characterization of signals from multi-scale edges. *IEEE Transactions on Pattern Analysis and Machine Intelligence*, 14:710–732, 1992.

[99] C. Li, C. Zheng, and C. Tai. Detection of ECG characteristic points using wavelet transforms. *IEEE Transactions on Biomedical Enigneering*, 42:21–28, 1995.

[100] Y. Yang, D. Yin, and R. Freyer. Development of a digital signal processor-based new 12-lead synchronization electrocardiogram automatic analysis system. *Computer Methods and Programs in Biomedicine*, 69:57–63, 2002.

[101] R. Warlar and C. Eswaran. Integer coefficient bandpass filter for the simultaneous removal of baseline wander, 50 and 100 hz interference from the ECG. *Medical and Biological Engineering and Computing*, 29:333–336, 1991.

[102] Q. Z. Xie, Y. H. Hu, and W. J. Tmopkins. Neural-network based adaptive matched filtering of QRS detection. *IEEE Transactions on Biomedical Enigneering*, 39:317–329, 1992.

[103] E. C. Ifeachor and B. W. Jervis. *Digital Signal Processing: A Practical Approach.* Addison-Wesley, 1995.

[104] R. S. Fowler and C. D. Finlay. The electrocardiogram of the neonate. In R. M. Freedom, L. N. Benson, and J. F. Smallhorn, editors, *Neonatal Heart Disease.* Springer–Verlag, London, 1992.

[105] J. Rautonen, A. Makela, H. Boyd, M. Apajasalo, and M. Pohjavuori. CRIB and SNAP: assessing the risk of death for preterm neonates. *Lancet*, 343 (8908):1272–1273, May 1994.

[106] The International Neonatal Network. The CRIB (clinical risk index for babies) score: a tool for assessing initial neonatal risk and comparing performance of neonatal intensive care units. *Lancet*, 342 (8865):193–198, Jul 1993.

[107] CWE Inc. *BMA-200 Portable Bioamplifier*. Ardmore PA, USA, 1995. Instruction Manual.